ors

Volume 3B

Materials, Properties and Preparation

Volume editor

S. MAHAJAN

Department of Materials Science
Carnegie Institute of Technology
Carnegie-Mellon University
Pittsburgh, PA 15213
USA

1994

NORTH-HOLLAND
AMSTERDAM · LONDON · NEW YORK · TOKYO

CHAPTER 19

Atomic Ordering and Phase Separation in Epitaxial III–V Alloys

Alex ZUNGER

National Renewable Energy Laboratory
Golden, CO 80401
USA

S. MAHAJAN

Department of Materials Science
Carnegie Mellon University
Pittsburgh, PA 15213
USA

Handbook on Semiconductors
Completely Revised Edition
Edited by T.S. Moss
Volume 3, edited by S. Mahajan

© 1994 Elsevier Science B.V.
All rights reserved

Contents

1. Introduction: essential physics of phase separation and ordering in semiconductor alloys . 1402
2. Factors affecting deviations from randomness 1408
   2.1. Macroscopic deviations from randomness: phase separation and long-range order . . 1408
   2.2. Microscopic deviations from randomness: short-range order 1412
3. Observation of microscopic deviations from randomness: clustering/anticlustering 1417
4. Macroscopic nonrandomness: phase separation 1419
   4.1. Observations of phase separation 1419
   4.2. Bulk versus epitaxial phase separation 1421
   4.3. Microstructure of phase-separated epitaxial layers 1424
      4.3.1. Phase separation in the substrate plane (lateral PS) 1425
         4.3.1.1. Fine-scale contrast 1426
         4.3.1.2. Coarse-scale contrast modulations 1433
         4.3.1.3. Lateral composition modulations at steps 1433
      4.3.2. Phase separation perpendicular to the substrate plane (vertical PS) 1435
   4.4. Effect of growth temperature on lateral phase separation 1437
   4.5. Thermal stability of phase-separated microstructures 1437
5. Observations of long-range atomic order in III–V alloys 1439
6. Influence of growth parameters on ordering in III–V alloys 1447
   6.1. Effects of growth temperature 1452
   6.2. Effects of growth rate 1454
   6.3. Effects of V/III ratio 1455
   6.4. Effects of dopants 1456
   6.5. Effects of substrate orientation and steps 1456
7. Physical origins of long-range order in III–V alloys 1457
   7.1. Early models based on bulk thermodynamics 1457
   7.2. Surface-reconstruction induced long-range order 1461
      7.2.1. Reconstruction of the mixed-cation surface 1462
      7.2.2. Reconstruction of the anion surface 1469
      7.2.3. How are the atomic arrangements in subsurface layers affected by surface geometry? 1470
   7.3. The surface phase diagram 1475
   7.4. Dynamics of ordering 1478
      7.4.1. The top-surface cation-reconstruction model of ordering 1479
      7.4.2. The top-surface anion-reconstruction model of ordering 1479
      7.4.3. The anion-reconstruction model of ordering with subsurface atomic rearrangements 1481
      7.4.4. The step-induced exchange model of ordering 1482

8. Influence of phase separation and atomic ordering on electronic and optical properties . . 1485
8.1. Observations of phase-separation effects on transport and optical properties 1485
8.2. Observations of long-range atomic-ordering effects on transport 1486
8.3. Observations of long-range atomic-ordering effects on optical properties 1486
8.3.1. Theory of optical effects in ideal CuPt structures 1490
8.3.2. Observations of band-gap changes in nearly perfectly ordered structures . . . 1497
8.3.2.1. CA structure of $GaAlAs_2$ 1497
8.3.2.2. CA structure of $Ga_2PAs/GaAs$ 1497
8.3.3. Theory of the relation between optical properties and the degree of ordering . . 1498
9. Implications of phase separation and atomic ordering on semiconductor technology . . . 1502
10. Summary 1504
11. Open issues and research opportunities 1505
References 1507

1. Introduction: essential physics of phase separation and ordering in semiconductor alloys

Most binary III–V semiconductor compounds crystallize at ambient conditions in the zinc-blende structure, which consists of two interpenetrating face-centered cubic (fcc) sublattices (left panel of fig. 1). The III-V binary compounds cover only a limited range of materials properties, e.g., band gaps and lattice parameters (circles in fig. 2). For many technological applications, it is desirable, however, to have material properties that are *intermediate* between those offered by the individual III–V binary compounds. The traditional way of achieving this is to create "solid solutions" of two or more of these "building blocks" (Goryunova and Fedorova 1955, Woolley 1962, Panish and Ilegems 1972, Stringfellow 1974). Such mixtures are generally thought to comprise random substitutions of the mixed atoms on the fcc lattice. These alloys have band gaps and lattice parameters that are intermediate between those of the constituents (denoted by lines in fig. 2). This article focuses on *deviations* from perfect randomness in such solid solutions and the way such deviations affect the electronic properties of the alloy film. Before discussing deviations from randomness, we briefly summarize the expected properties of *random semiconducting solid solutions.*

We distinguish *chemical randomness* from *positional randomness*. In a perfect chemically random solid solution, each of the alloyed atoms occupies lattice sites with no correlation to the occupation of the other sites. For example, in a chemically random $Ga_{0.5}Al_{0.5}As$ alloy the fcc cation sites would be occupied by Ga and Al atoms according to a coin toss. Perfect chemical randomness implies absence of short- and long-range order, so their diffraction patterns manifest neither new (superstructure) Bragg peaks nor strong diffuse scattering in between the Bragg peaks (except for the monotonic Laue scattering (Warren 1969)). The absence of correlations among site occupancies further implies that the effective A–B interactions are indistinguishable from the (A–A) + (B–B) interactions, hence the mixing enthalpies are, by definition, zero. Perfect randomness is, as expected, a rare occurrence, existing in isotope alloys and to some extent in high-temperature-grown $Al_{1-x}Ga_xAs$ and $Si_{1-x}Ge_x$ alloys (Thurmond 1953, Woolley 1962, Panish and Ilegems 1972), having very small mixing enthalpies, and nearly ideal liquidus–solidus lines and diffraction patterns. Perfect chemical randomness does not imply positional randomness: we now know (Mikkelson and Boyce 1982) that even in *melt-grown* semiconductor $A_{1-x}B_xC$ alloys (which are chemically close to being random) the A–C and B–C bonds "relax", so their lengths R_{AC} and R_{BC} are close to those in the *pure* constituents, thus deviating significantly from the "virtual lattice" average value. Such atomic relaxations off the ideal zinc-blende sites could create lines and pseudo-satellites in X-ray and electron

Ordering Vectors	(0,0,0)	(0,0,1)		(2,0,1)		(1,1,1)
Name (ternary)	Zincblende (Sphalerite)	Layered Tetragonal	"Luzonite"	Chalcopyrite	Famatinite	Layered Trigonal
Formula:	n = 0,4;AC	n = 2;ABC_2	n = 1,3; A_3BC_4	n = 2;ABC_2	n = 1,3; A_3BC_4	n = 2;ABC_2
	Zn S	In Ga As	As Cu S	Cu Fe S	Sb Cu S	A B C
Example: (ternary)	ZnS-type	$InGaAs_2$-type	Cu_3AsS_4-type	$CuFeS_2$-type	Cu_3SbS_4-type	$CrCuS_2$-type ($NaVS_2$)
Bravais Lattice:	Face centered cubic	Simple tetragonal	Simple cubic	Body centered tetragonal	Body centered tetragonal	Rhombohedral
Space Group						
Int. Tables:	$F\bar{4}3m$	$P\bar{4}m2$	$P\bar{4}3m$	$I\bar{4}2d$	$I\bar{4}2m$	R3m
Schoenflies:	T_d^2	D_{2d}^5	T_d^1	D_{2d}^{12}	D_{2d}^{11}	C_{3v}^5
Number:	216	115	215	122	121	160
Struckturbericht	B3	—	$H2_4$	$E1_1$	$H2_a$	
Pearson symbol:	CF8	—	CP8	tI16	tI16	hR4
Atomic positions: (ternary)	Zn: 4 a $\bar{4}3m$ S: 4 c $\bar{4}3m$	1A: 1 a $\bar{4}2m$ 1B: 1 c $\bar{4}2m$ 2C: 2 g mm	3 Cu: 3 c $\bar{4}2m$ 1 As: 1 a $\bar{4}3m$ 4 S: 4 e 3m	2 Cu: 4 a $\bar{4}$ 2 Fe: 4 b $\bar{4}$ 4 S: 8 d 2	1 Cu: 2 b $\bar{4}2m$ 2 Cu: 4 d $\bar{4}$ 1 Sb: 2 a $\bar{4}2m$ 4 S: 8 i m	1 A: 1 a 3m 1 B: 1 a 3m 1 C: 1 a 3m 1 C: 1 a 3m
Equivalent superlattice:	None	(1,1) in [0 0 1] direction	None	(2,2) in [2 0 1] direction	(1,3) in [2 0 1] direction	(1,1) in [1 1 1] direction

Fig. 1. Ordered adamantine structures discussed in this review (from Wei and Zunger 1989).

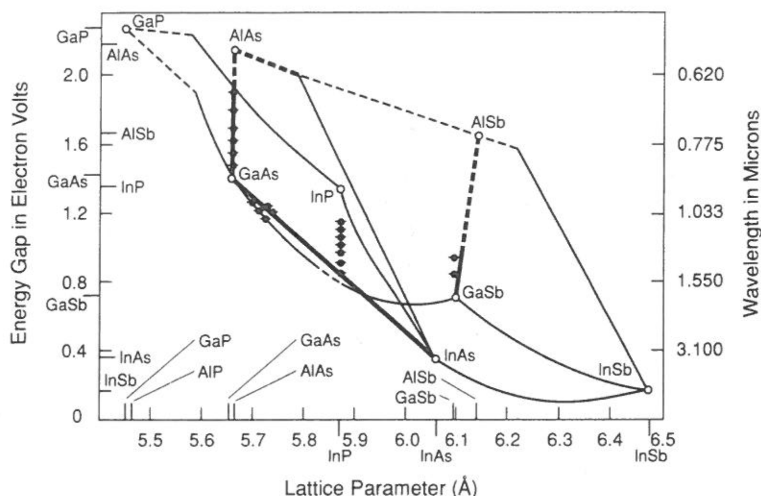

Fig. 2. Lattice parameters, band gaps, and emission wavelengths of binary III–V compounds. From R.E. Nahory (Bellcore).

diffraction patterns (Glas 1989b, Glas et al. 1990). Furthermore, even perfect chemical randomness (without long- or short-range order) does enable the existence of potential fluctuations and hence band tails. Potential fluctuations are manifested by the existence of a random distribution of A-site and B-site perturbations, $V_A - \bar{V}$ and $V_B - \bar{V}$, about the average potential $\bar{V}$. If these perturbations are sufficiently large, a bound state can form in the band gap, to which excitons can bind. If this "impurity" binding energy is too large, exciton–phonon interactions broaden the exciton line. This is the case for CdS : Te (Cuthbert and Thomas 1968) and ZnS : Te (Tchakpele and Albert 1988). If the impurity binding is weaker, sharp exciton lines can be seen. Most isovalent substitutions in III–V compounds (e.g., Al/Ga/In or P/As) do not form a bound impurity-like band. In such cases the exciton lines are visible but are broader than those in the binary constituents (Mena et al. 1991). Each interband transition in the alloy manifests a uniform, downwards shift with respect to that of the constituents. This phenomenon of "optical bowing" exists in principle, even in perfectly random alloys, and represents the combined response of band states to random chemical (i.e., $V_A \neq V_B$) and relaxational (i.e., $R_{AC} \neq R_{BC}$) fluctuations (Bernard and Zunger 1986, 1987). Potential fluctuations lead to a broadened absorption tail relative to the pure constituents. In most semiconductor alloys, the scale of broadening is $\ll 10$ meV. If the potential fluctuations are strong (e.g., for hole states in mixed-anion alloys such as CdSSe), the excited photocarriers could scatter effectively, thus washing out most of the spectral features of the pure components except for the impurity-localized excitons. On the other hand, if the potential fluctuations are weak (e.g., for electron states in mixed-cation alloys such as CdZnTe or GaInAs), most excitonic features of the pure constituents also exist in the alloy. These basic properties of perfectly random alloys will serve as a benchmark against which the properties of nonrandom alloys will be compared.

Deviations from perfect randomness were observed, both on a "small" (i.e., a few bond lengths) and a "large" (many bond lengths) distance scale. Small-scale deviations from randomness can appear as "short-range order" (SRO). It is manifested either by a preferential association of like atoms ("clustering" or "local phase-separation") or unlike atoms ("anticlustering" or "local ordering"). In either case, the scale of the deviation from randomness we discuss under "SRO" is limited to one or a few bond lengths. Short-range order produces diffuse scattering, i.e., scattering *in between* the Bragg peaks (Bocchi et al. 1985, Yasuami et al. 1992). It is further observed in Raman spectroscopy (Compaan et al. 1990a,b,c), infrared absorption (Yamazaki et al. 1980, Perkowitz et al. 1991), and nuclear magnetic resonance (NMR) chemical shifts (Beshah et al. 1987, Zax et al. 1987). Large-scale ("macroscopic") deviations from randomness appear either as phase separation or as long-range order (LRO), or both. They occur on a length scale of ten or more bond distances. Long-range order is manifested by the appearance of superlattice diffraction spots (see below), removal of the valence band degeneracy (Kanata et al. 1992, 1993, Alonso et al. 1993, Glembocki et al. 1992, Horner et al. 1993), altered polarization in optical and other spectroscopies (Mascarenhas et al. 1989, Mascarenhas and Olson 1990, Kanata et al. 1992, 1993), and in correlated NMR chemical shifts (Tycko et al. 1992). Phase separation is observed among others by X-ray microanalysis (Henoc et al. 1982, Glas 1989a,b) as well as by bright- and dark-field images in electron microscopy. All forms of deviations from perfect randomness – small-scale clustering and anticlustering, or large-scale phase separation and long-range order — profoundly affect the materials properties.

The various forms of deviations from randomness can have thermodynamic or kinetic origins. Thermodynamically mandated deviations can be classified by considering the formation (f) energy $\Delta E_{\mathrm{f}}(\sigma_x)$ of the ordered compound A/B in structure σ, and the mixing (mix) energy $\Delta E_{\mathrm{mix}}(x)$ of the random alloy $A_{1-x}B_x$ of composition x. These are defined as the excess energy taken with respect to the energies of equivalent amounts of the solid constituents A and B at their equilibrium molar volumes V_{A} and V_{B}:

$$\Delta E_{\mathrm{f}}(\sigma_x) = E_\sigma(\text{ordered}) - [(1-x)E_{\mathrm{A}} - xE_{\mathrm{B}}], \tag{1}$$

$$\Delta E_{\mathrm{mix}}(x) = E(\text{random}) - [(1-x)E_{\mathrm{A}} - xE_{\mathrm{B}}]. \tag{2}$$

Here, E is the total electronic plus nuclear energy of the system with the appropriate boundary conditions (e.g., bulk, or at the presence of a surface). The "ordering energy" is defined as the difference

$$\delta E_{\mathrm{ord}}(\sigma_x) = \Delta E_{\mathrm{f}}(\sigma_x) - \Delta E_{\mathrm{mix}}(x). \tag{3}$$

These simple definitions permit a classification of the various forms of nonrandomness: if $\delta E_{\mathrm{ord}}(\sigma_x) < 0$, the random alloy at composition x can develop SRO of the type underlying the ordered structure σ. When $\Delta E_{\mathrm{f}}(\sigma) < 0$, the LRO configuration σ could become a stable "ground-state structure", whereas $\Delta E_{\mathrm{f}}(\sigma) > 0$ means that the ordered structure σ is globally unstable with respect to phase separation into A and B.

Analysis of the measured phase diagrams of many III–V alloys (Stringfellow 1974,

Panish and Ilegems 1972, Martins and Zunger 1984) have shown that their mixing enthalpies $\Delta E_{\mathrm{mix}}(x)$ can be fitted to the form $\Omega x(1-x)$ and that the "interaction parameter" Ω is *positive* in all cases examined. Furthermore, it was found (Foster 1976, Stringfellow 1974) that Ω scales with the lattice mismatch between the binary constituents, i.e., $\Omega \sim [(a_{\mathrm{AC}} - a_{\mathrm{BC}})/\bar{a}]^{\lambda}$, where $\bar{a}$ is the average lattice constant and λ is a positive power. These well-established facts led to the general expectation that alloys of zinc-blende semiconductors would never exhibit either local or long-range order. This was based on the time-honored principle of metallurgy that ordering requires attractive interactions between the constituents, and that $\Omega > 0$ indicates repulsive interactions, hence, no ordering. Of course the classic "regular-solution" model or the "DLP" model (Stringfellow 1974) equating the enthalpy with $\Omega x(1-x)$ has no way of distinguishing ordered from random phase at the same x, so it is easy to see why the possibility of LRO in semiconductor alloys was overlooked.

More general theoretical analyses of ordering phenomena have indicated otherwise (Srivastava et al. 1985, Balzarotti et al. 1985a,b, Zunger 1986, Ichimura and Sasaki 1986, Mbaye et al. 1987, Martins and Zunger 1984, 1985, 1986a,b, Ferreira et al. 1989, Wei and Zunger 1988a, Wei et al. 1990, Bernard et al. 1988, 1991, Dandrea et al. 1990a). To illustrate the basic physical considerations, consider a few of the possible relative arrangements of the pertinent energies, i.e., that of phase separation (A + B; our zero of energy), the random alloy E(random), and the energies E(ordered) of some specific ordered structures, e.g., ord-I, ord-II, and ord-III (fig. 3, left). Figure 1 shows some possible ordered arrangements σ of two zinc-blende constituents (Wei and Zunger 1989). We distinguish three main relative sequences of stability:

(1) In the case of a structure of the type designated in fig. 3 as ord-I, we have $\Delta E_{\mathrm{f}}(\mathrm{I}) < 0$ and $\delta E_{\mathrm{ord}}(\mathrm{I}) < 0$. In this case the ground state will exhibit stable LRO in configuration $\sigma = \mathrm{I}$, and the disordered alloy will exhibit macroscopic SRO of the anticlustering (i.e., local ordering) type.

(2) In the case of a structure of type ord-II, we have $\Delta E_{\mathrm{f}}(\mathrm{II}) > 0$ but $\delta E_{\mathrm{ord}}(\mathrm{II}) < 0$. Unlike the previous case, here the ground state corresponds to phase separation of the structure II into its constituents A + B. However, as is the case in ord-I, here too the disordered alloy could exhibit SRO of the *anticlustering* type, since $\delta E_{\mathrm{ord}} < 0$. Note, therefore, that in this case, phase separation can coexist with local ordering tendencies in the same phase diagram.

(3) In the case of structure type ord-III, we have $\Delta E_{\mathrm{f}}(\mathrm{III}) > 0$ and $\delta E_{\mathrm{ord}}(\mathrm{III}) > 0$. Here, the ground state at low temperatures ($T < T_{\mathrm{MG}}$) corresponds to phase separation, whereas just above the "miscibility gap" temperature ($T > T_{\mathrm{MG}}$) the disordered alloy will exhibit clustering of like atoms. At yet higher temperatures (if the crystal does not melt), this SRO disappears and the alloy becomes random.

In cases II and III the phase diagram will consist of a miscibility gap with maximum at T_{MG}, followed by a disordered solid solution at higher temperatures. Microscopically, however, the disordered solid solution will exhibit anticlustering and clustering for cases II and III, respectively. The phase diagram of case I is of the "ordering type", exhibiting LRO below some order–disorder transition temperature T_{c} and a phase transition into the anticlustered disordered phase above T_{c}.

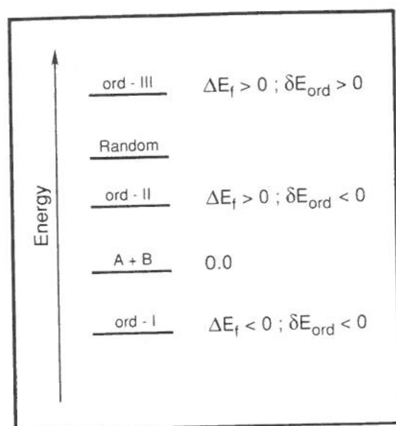

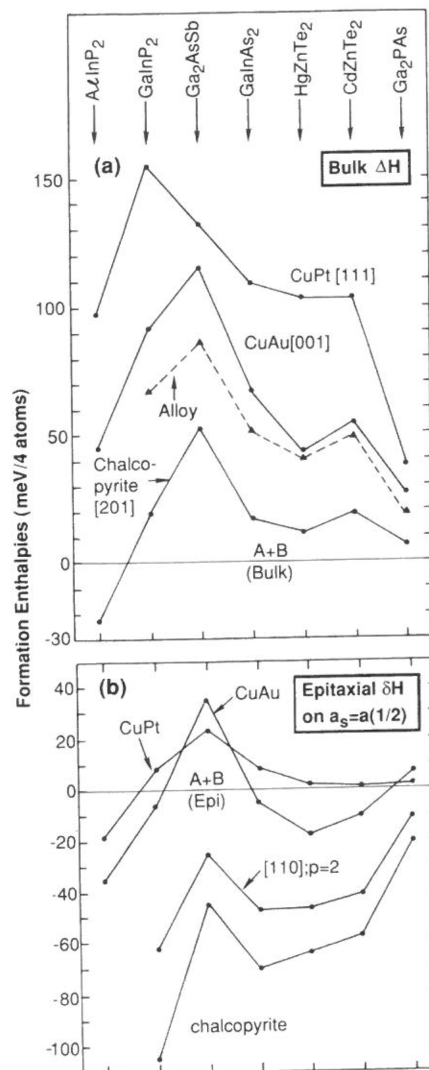

Fig. 3. Left: schematic depiction of the relative internal energies of phase separation (A + B; the energy zero), the random alloy, and three prototypical ordered structures I, II, and III. See eqs. (1)–(3). Right: calculated formation enthalpies of bulk (a) and lattice-matched epitaxial alloys (b). From Bernard et al. (1990).

In classical metallurgy, one encounters predominantly either "compound-forming systems" (type I above) or "phase-separating systems" (type III above). Recent theoretical studies to be reviewed here, have shown, however, that most semiconductor alloy systems belong to type II. This has been borne out during the last decade. Results indicate that most III–V alloys exhibit two main types of deviations from random distribution of the atomic species:

- *phase separation* (Henoc et al. 1982, Glas et al. 1982, Launois et al. 1982, Mahajan et al. 1984a, 1989, Ueda et al. 1984, 1988, 1989a,b, Norman 1985, Norman

and Booker 1985, Chu et al. 1985, Treacy et al. 1985, Shahid and Mahajan 1988, McDevitt 1990, McDevitt et al. 1992).

● *long-range atomic ordering* (Kuan et al. 1985, 1987, Nakayama and Fujita 1986, Jen et al. 1986, 1987, 1989a,b, Murgatroyd et al. 1986, 1990, Shahid et al. 1987, Ueda et al. 1987, 1988, 1989a,b, 1991, Norman et al. 1987, Ihm et al. 1987, Gomyo et al. 1987, 1988a,b, 1989a,b, Suzuki et al. 1988a,b,c, 1992, Bellon et al. 1988, 1989, Dabkowski et al. 1988, Gavrilovic et al. 1988, Kondow et al. 1988a,b 1989a, McKernan et al. 1988, Morita et al. 1988, Nozaki et al. 1988, Plano et al. 1988, Shahid and Mahajan 1988, Wada and Maeda 1988, Augarde et al. 1989, Kondow and Minagawa 1989, Cao et al. 1989, 1991, Mahajan and Shahid 1989, Okuda et al. 1989, Otsuka et al. 1989, Stringfellow 1989, Suzuki and Gomyo 1990a,b, 1991, Kurtz et al. 1988, 1990a,b, Chen et al. 1990, 1991, McDevitt et al. 1990, Baxter et al. 1991, Chen and Stringfellow 1991, McDermott et al. 1991, Ueda and Nakata 1992, Chu et al. 1992, Philips et al. 1993).

In this chapter the current status of our understanding of phase separation and atomic ordering in ternary and quaternary III–V alloys is assessed both from experimental and theoretical considerations. The effects of these microstructural features on physical properties are discussed. Finally, possible ramifications of phase separation and atomic ordering in semiconductor technology and open research issues are discussed.

2. Factors affecting deviations from randomness

2.1. *Macroscopic deviations from randomness: phase separation and long-range order*

We next discuss why particular semiconductor alloys behave as types I, II, and III above (fig. 3). The qualitative physics can be appreciated by decomposing the excess energies ΔE of eqs. (1) and (2) into physically recognizable components. We will take the general "chemical reactions"

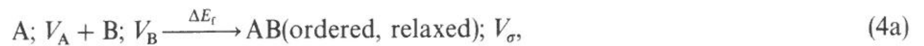

$$\mathrm{A};\ V_\mathrm{A} + \mathrm{B};\ V_\mathrm{B} \xrightarrow{\Delta E_\mathrm{f}} \mathrm{AB(ordered,\ relaxed)};\ V_\sigma, \tag{4a}$$

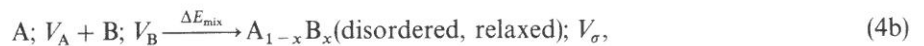

$$\mathrm{A};\ V_\mathrm{A} + \mathrm{B};\ V_\mathrm{B} \xrightarrow{\Delta E_\mathrm{mix}} \mathrm{A}_{1-x}\mathrm{B}_x\mathrm{(disordered,\ relaxed)};\ V_\sigma, \tag{4b}$$

describing the formation of ordered compounds (4a) and random alloys (4b) at their volume V_σ, and break them into steps (Srivastava et al. 1985, Bernard and Zunger 1986, Bernard et al. 1988) as follows.

First, deform hydrostatically the pure solids A and B from their equilibrium molar volumes V_A and V_B, respectively, to the volume V_σ akin to the final compound or alloy σ:

$$\mathrm{A};\ V_\mathrm{A} + \mathrm{B};\ V_\mathrm{B} \xrightarrow{\Delta E_\mathrm{VD}} \mathrm{A},\ V_\sigma + \mathrm{B},\ V_\sigma. \tag{5}$$

Since V_σ is usually intermediate between V_A and V_B, this process involves hydrostatic

compression of the component with the larger molar volume and *dilation* of the component with the smaller molar volume. In doing so, we invest a "volume deformation" (VD) energy which we denote ΔE_{VD}. It vanishes if the constituents are size-matched ($V_{\mathrm{A}} = V_{\mathrm{B}} = V_{\sigma}$) and is *positive* (i.e., promotes phase separation) otherwise. Since, to within a good approximation (Ferreira et al. 1988), the molar volumes of different structures with the same compositions (e.g., σ = ordered versus σ = random) are nearly equal, ΔE_{VD} depends essentially on the composition x but not on the microscopic atomic arrangement within σ.

Second, react $\mathrm{A}(V_{\sigma})$ and $\mathrm{B}(V_{\sigma})$, both already prepared at their "final" volume V_{σ}, and form the final compound in its *ideal unrelaxed structure*:

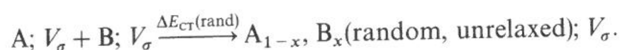

$$\mathrm{A};\, V_{\sigma} + \mathrm{B};\, V_{\sigma} \xrightarrow{\Delta E_{\mathrm{CT}}(\mathrm{ord})} \mathrm{AB}(\text{ordered, unrelaxed});\, V_{\sigma},$$
$$\mathrm{A};\, V_{\sigma} + \mathrm{B};\, V_{\sigma} \xrightarrow{\Delta E_{\mathrm{CT}}(\mathrm{rand})} \mathrm{A}_{1-x},\, \mathrm{B}_{x}(\text{random, unrelaxed});\, V_{\sigma}. \tag{6}$$

Here one imagines forming a mixed compound or alloy, but the atoms in either structure are held fixed at their ideal (e.g., zinc-blende) positions. For example, if the cubic lattice parameter of the mixed system is $a(x)$, in step (6) one constrains the nearest-neighbor bond lengths to equal $R_{\mathrm{A-C}} = R_{\mathrm{B-C}} = \sqrt{3}a(x)/4$, just as in the zinc-blende structure with lattice constant $a(x)$. Since a *mixed* structure is formed in this reaction, charge transfer (CT), hybridization, and other band-structure effects can take place. These could either lower or raise the energy relative to the binaries. We call the change in total energy in reaction (6) $\Delta E_{\mathrm{CT}}(\sigma)$.

Finally, permit the atoms in the ordered or random compound to relax to their energy-minimizing positions,

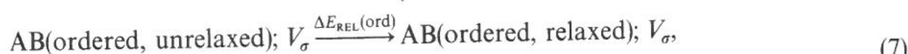

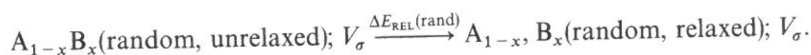

$$\mathrm{AB}(\text{ordered, unrelaxed});\, V_{\sigma} \xrightarrow{\Delta E_{\mathrm{REL}}(\mathrm{ord})} \mathrm{AB}(\text{ordered, relaxed});\, V_{\sigma},$$
$$\mathrm{A}_{1-x}\mathrm{B}_{x}(\text{random, unrelaxed});\, V_{\sigma} \xrightarrow{\Delta E_{\mathrm{REL}}(\mathrm{rand})} \mathrm{A}_{1-x},\, \mathrm{B}_{x}(\text{random, relaxed});\, V_{\sigma}. \tag{7}$$

In our example above, the C atom (e.g., P in $\mathrm{Ga}_{1-x}\mathrm{In}_{x}\mathrm{P}$) can be displaced away from the center of the cation tetrahedron, leading to $R_{\mathrm{A-C}} \neq R_{\mathrm{B-C}}$. Such strain-relieving relaxations (REL) lower the total energy by an amount denoted ΔE_{REL}. Like the volume-deformation energy, $\Delta E_{\mathrm{REL}}(\sigma)$ tends to vanish for size-matched systems (if the bond lengths are naturally equal, there is little driving force for atomic displacements). In contrast to ΔE_{VD}, however, relaxations depend on the atomic configuration σ, since certain structures can better pack dissimilar atomic sizes than others. Furthermore, relaxation is always energy-*lowering*, hence, it promotes compound formation.

The sum of reactions (5), (6), and (7) adds up to the overall formation reaction (4). We see that the basic physical factors governing compound or alloy formation are

$$\Delta E_{\mathrm{f}}(\sigma_{x}) = \Delta E_{\mathrm{VD}}(x) + \Delta E_{\mathrm{CT}}(\text{ordered}, \sigma) + \Delta E_{\mathrm{REL}}(\text{ordered}, \sigma), \tag{8}$$

$$\Delta E_{\mathrm{mix}}(x) = \Delta E_{\mathrm{VD}}(x) + \Delta E_{\mathrm{CT}}(\text{random}) + \Delta E_{\mathrm{REL}}(\text{random}), \tag{9}$$

$$\delta E_{\mathrm{ord}}(\sigma) = [\Delta E_{\mathrm{CT}}(\text{ord}, \sigma) - \Delta E_{\mathrm{CT}}(\text{rand})] + [\Delta E_{\mathrm{REL}}(\text{ord}, \sigma) - \Delta E_{\mathrm{REL}}(\text{rand})]. \tag{10}$$

The classic view (Panish and Ilegems 1972, Stringfellow 1974) that ΔE of either ordered or disordered phases can be represented by the same form (e.g., $\Omega x(1-x)$) is appropriate to $\Delta E_{VD}(x)$ alone. Both ΔE_{CT} and ΔE_{REL} are generally different for different atomic arrangements σ. This crucial factor, overlooked by standard thermodynamic theories of semiconductor alloys (Panish and Ilegems 1972, Foster 1976, Stringfellow 1974, 1982a,b, Glas 1987, Johnson and Chiang 1988, Chiang and Johnson 1989, Larche et al. 1988) leads to the possibility of coexistence of ordering with phase separation.

We can now analyze the expected phase behavior of different semiconductor alloys. In a series of papers (Srivastava et al. 1985, Zunger 1986, Bylander and Kleinman 1986, Mbaye et al. 1987, Martins and Zunger 1985, 1986a,b, Bernard et al. 1988, 1990, 1991, Boguslawski and Baldereschi 1988, Wood et al. 1988, Dandrea et al. 1990a, Wei and Zunger 1988a,c, 1989, 1990, 1992, Wei et al. 1990, Ferreira et al. 1989, Froyen and Zunger 1991a,b, Magri and Zunger 1991) the different terms in eqs. (8)–(10) have been calculated from self-consistent first-principles local density theory for many semiconductor alloys. Details are given in the original papers. The right-hand side of fig. 3 (Bernard et al. 1990) shows the calculated ΔE_f and ΔE_{mix} of a few alloys in the structures shown in fig. 1. The basic trends can be summarized as follows:

(i) Pseudobinary alloys made of lattice-*matched*, isovalent binary constituents, such as $Al_{1-x}Ga_xAs$ or $Cd_{1-x}Hg_xTe$ (Wei and Zunger 1988a, Magri and Zunger 1991), have $\Delta E_{VD} = \Delta E_{REL} \approx 0$ (since the tetrahedral atomic radii of the mixed atoms are nearly equal), but the charge-transfer energy ΔE_{CT} is slightly *positive*. The total $\Delta E_f \geqslant 0$ and $\Delta E_{mix} \geqslant 0$ are thus positive. Hence, these alloys belong to "type III" above, exhibiting phase separation at very low temperatures (fig. 4a) and weak clustering-type SRO just above the (low) miscibility gap temperature (Bocchi et al. 1985). This behavior is analogous to the metallurgical phase-separating alloys Cu–Rh or Pd–Rh. Type-III alloys include also the nonisovalent cases of $(GaAs)_x(Ge_2)_{1-x}$ having $\Delta E_f > 0$, $\Delta E_{mix} > 0$, and $\delta E_{ord} > 0$ (Osorio et al. 1991a,b, Dandrea et al. 1990b). The latter alloys exhibit large miscibility gaps, strong clustering, and no bulk ordering, since $\Delta E_{VD} \geqslant 0$ and $\Delta E_{CT} + \Delta E_{REL} \gg 0$.

(ii) Pseudobinary alloys made of binary isovalent constituents having different bond lengths, such as $Ga_{1-x}In_xP$, $Ga_{1-x}In_xAs$, $GaAs_{1-x}P_x$, $GaAs_{1-x}Sb_x$ (or binary $Si_{1-x}Ge_x$ and $C_{1-x}Ge_x$ alloys), have $\Delta E_f > 0$ and $\Delta E_{mix} > 0$ (fig. 3, right), hence, like in case (i) above, their ground state also corresponds to phase separation. The reason is that the positive volume-deformation energies ΔE_{VD} exceed in magnitude the *negative* "chemical energy" $\Delta E_{CT} + \Delta E_{REL}$. Calculated phase diagrams shown in figs. 4b–e (Wei et al. 1990) hence exhibit miscibility gaps. However, a certain ordered structure – the chalcopyrite (fig. 1) – is able to accommodate large size mismatches better than the random alloy (Bernard et al. 1988, 1990), hence ΔE_{REL}(chalcopyrite) $< \Delta E_{REL}$ (random). This leads to δE_{ord}(chalcopyrite) < 0 (fig. 3, right). If one considers surface free energies, also δE_{ord}(CuPt) < 0 at the surface (this is further discussed in § 7.2). This class of semiconductor alloys represents a "type-II" system. Hence, semiconductor alloys consisting of isovalent binary constituents having different bond lengths are expected to show (a) phase separation as a ground

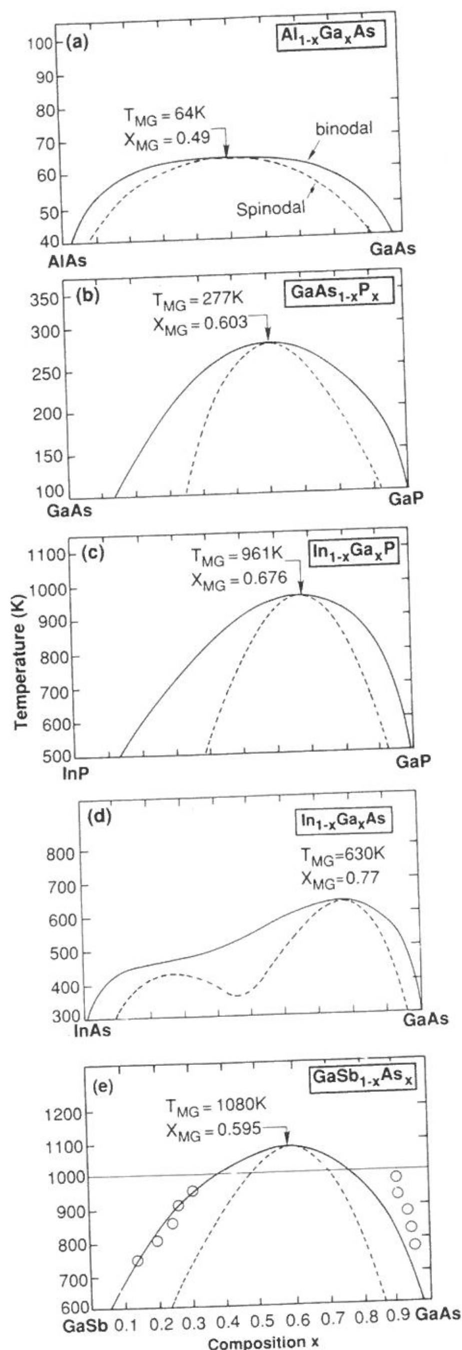

Fig. 4. Calculated phase diagrams for the III–V alloys (a) $Al_{1-x}Ga_xAs$, (b) $GaAs_{1-x}P_x$, (c) $In_{1-x}Ga_xP$, (d) $In_{1-x}Ga_xAs$, and (e) $GaSb_{1-x}As_x$. The solid (dashed) lines give the binodal (spinodal) lines. Low-temperature ordered phases are not shown. The arrows point to the maximum miscibility gap (MG) temperatures and compositions. The circles in (e) are the recent experimental data of Ishida et al. (1988); the horizontal line in (e) represents the peritectic line. From Wei et al. (1990).

state, (b) *bulk* chalcopyrite ordering when phase separation is inhibited, and (c) CuPt ordering at a free surface (see § 7.2 below). These alloy systems are analogous to the metallurgical case of Ni–Au ($\Delta E_f > 0$ but $\delta E_{ord} < 0$), showing phase separation at low temperature but ordering-type SRO at higher temperatures (Lu et al. 1993).

(iii) Some semiconductor alloys have very strong stabilizing charge-transfer ($\Delta E_{CT} \ll 0$) and $\Delta E_{VD} + \Delta E_{REL} \equiv 0$. This leads to stable, ordered compound formation $\Delta E_f < 0$. The main example is SiC (Martins and Zunger 1986a,b). A second case of $\Delta E_f < 0$ is $AlInP_2$ and $AlInAs_2$ in the chalcopyrite structure (Dandrea et al. (1990a) and fig. 3, right). Here, a stabilizing Al → In charge transfer combines with an effective chalcopyrite relaxation to give $\Delta E_{CT} + \Delta E_{REL} < \Delta E_{VD}$. These alloy systems belong to type I above, and are analogous to the metallurgical cases of compound-forming systems, e.g., Cu–Au or Ni–Pt (Lu et al. 1993), in that they should spontaneously order at low temperatures.

With the exception of AlAs/GaAs (type III) and chalcopyrite $AlInP_2$ and $AlInAs_2$ (type I) all pseudobinary III–V alloy systems can be classified as type-II systems. Their hallmark is the *coexistence* of phase separation and ordering.

2.2. *Microscopic deviations from randomness: short-range order*

Our foregoing discussion clarified the expected *macroscopic* behavior of alloys: when $\Delta E_{mix} > 0$ (as is the case in most lattice-mismatched III–V or II–VI alloys) one expects phase separation below the miscibility gap (MG) temperature T_{MG}. Evidence for this is discussed in the next section. The local or *microscopic* behavior can, however, be quite intricate relative to what is suggested merely by the sign of ΔE_{mix}. Consider, for example, a fourfold coordinated pseudobinary $A_{1-x}B_xC$ alloy with a "common atom" C. The nearest-neighbor atomic arrangements about the common atom can be A_4, A_3B, A_2B_2, AB_3, or B_4. We will denote these microclusters as $A_{4-n}B_n$ with $0 \leqslant n \leqslant 4$. If the alloy were perfectly random (R), the probability of finding in the alloy a cluster of type n at composition x is given by the Bernoulli distribution

$$P_R^{(n)}(x) = \binom{4}{n} x^n (1-x)^{4-n}. \tag{11}$$

The actual probabilities $P^{(n)}(x, T)$ can deviate from randomness. We define the *excess* probability with respect to the perfectly random alloy as

$$\Delta P^{(n)}(x, T) = P^{(n)}(x, T) - P_R^{(n)}(x). \tag{12}$$

When $T \to \infty$ one has $\Delta P^{(n)}(x, \infty) = 0$. The main question pertaining to the form of microscopic deviations from randomness is, therefore, equivalent to asking what is the sign and magnitude of $\Delta P^{(n)}$. If the *mixed* clusters A_3B, A_2B_2, or AB_3 exist in *excess* of what the random probability (eq. (11)) would predict, we say that "anticlustering" exists, whereas the reverse implies "clustering". An alternative measure of microscopic deviations from randomness is given by the "clustering parameter" β (Verleur and Barker 1966). Denoting the probability of finding two A atoms or two

B atoms by P_{AA} and P_{BB}, respectively, one has

$$P_{AA} = (1-x) + x\beta, \qquad (13)$$
$$P_{BB} = x + (1-x)\beta,$$

so when $\beta = 0$ we have $P_{AA} = 1 - x$ and $P_{BB} = x$. In terms of the excess tetrahedron probabilities of eq. (12) this can be written as

$$\beta(x) = \frac{-1}{2x(1-x)}\left[\tfrac{1}{2}\,\Delta P^{(1)}(x,T) + \tfrac{1}{2}\,\Delta P^{(3)}(x,T) + \tfrac{2}{3}\,\Delta P^{(2)}(x,T)\right]. \qquad (14)$$

For the perfectly random alloy $\beta = 0$. "Clustering" means $\beta > 0$ while "anticlustering" means that $\beta < 0$.

The microscopic deviations from randomness in semiconductor alloys were calculated thermodynamically by Balzarotti et al. (1985a,b), Ichimura and Saski (1986), Sher et al. (1986), Mbaye et al. (1987), Patrick et al. (1987), Ferreira et al. (1988, 1989), and Wei et al. (1990). Although the methods of calculation are different, the results are rather similar. The underlying physics can be appreciated by applying the decomposition of eqs. (8), (9) to the excess energy of *each cluster*. The latter reads, in analogy with eq. (1),

$$\Delta E^{(n)} = E^{(n)}[A_{4-n}B_n] - \frac{4-n}{4}\,E^{(0)}[A_4] - \frac{n}{4}\,E^{(4)}[B_4]. \qquad (15)$$

The energy required to deform the pure A and B *clusters* into the common volume is denoted by $G(x) = \Delta E^{(n)}_{VD}$, whereas the charge-transfer and relaxation energy of cluster n is denoted $\varepsilon^{(n)} = \Delta E^{(n)}_{CT} + \Delta E^{(n)}_{REL}$. We then have for cluster n

$$\Delta E^{(n)}(X_n) = \varepsilon^{(n)} + G(X_n), \qquad (16a)$$

where $X_n = \frac{1}{4}(4-n)$ is cluster composition. Here $\varepsilon^{(n)}$ is the constant-volume "chemical" energy of cluster n, while $G(X_n)$ is its elastic energy. A random alloy can be thought of as a mixture of all clusters, so

$$\Delta E_{mix}(x,T) = G(x) + \sum_n P^{(n)}(x,T)\varepsilon^{(n)}, \qquad (16b)$$

while for an ordered compound of type n at $x = X_n$

$$\Delta E_f = G(X_n) + \varepsilon^{(n)}. \qquad (16c)$$

We see that a random alloy can be thought of as a weighted mixture of all clusters (eq. (16b)) while a simple ordered compound isolates a single cluster and repeats it periodically (eq. (16c)). The basic results of the theoretical studies of clustering in semiconductor alloys can be summarized as follows:

(i) $\Delta P^{(n)}(x,T)$ *depends on the constant-volume chemical energies* $\varepsilon^{(n)}$ *but not on the elastic deformation energy* $G(x)$ (Ferreira et al. 1988, Wei et al. 1990). This follows simply from the fact that at a fixed composition x the elastic energy $G(x)$ is common to all clusters n, so the only distinguishing factor is the "chemical" energy $\varepsilon^{(n)}$. When $\varepsilon^{(n)} < 0$ we expect local ordering (anticlustering), whereas $\varepsilon^{(n)} > 0$ leads to local phase-separation (clustering). Here we assume that all clusters are coherent with the alloy.

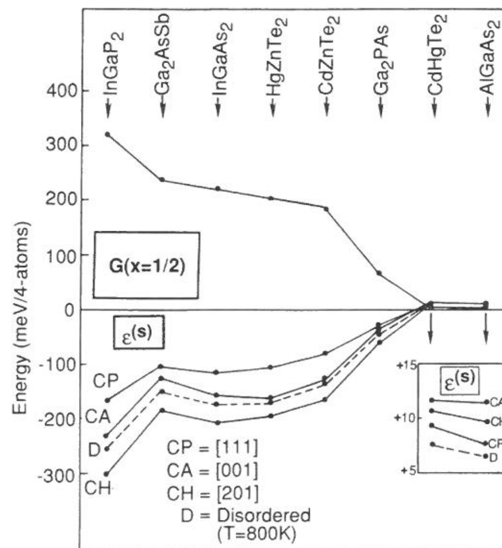

Fig. 5. Breakdown of the formation enthalpies of ordered 50%–50% intersemiconductor compounds CP (CuPt), CA (CuAu), and CH (chalcopyrite) into elastic $G(x=\frac{1}{2})$ and substitutional $\varepsilon^{(s)}$ pieces (eq. (16a)). For comparison, we also give the substitutional energy for the random 50%–50% alloy (denoted R) at $T = 800$ K. Note that $\varepsilon^{(s)} > 0$ (inset) for the two size-matched alloys. From Bernard et al. (1990).

(ii) On the other hand, the elastic energy $G(x)$ can play a decisive role in determining the *macroscopic* phase separation. This is obvious if one considers an example where x_1 and x_2 are the compositions of two phases in equilibrium. By assumption, $x_1 \neq x_2$. Now switch on $G(x)$ in eq. (16). Since in general $G(x_1) \neq G(x_2)$, the two phases cannot be in equilibrium any longer. Their equilibrium compositions would have to be shifted to x_1' and x_2', thus altering the shape of the phase diagram.

(iii) Lattice-mismatched semiconductor alloys have $G(x) > 0$ but $\varepsilon^{(n)} < 0$ (since charge transfer and relaxation lower the energy). This is illustrated by the calculated ε and $G(x=0.5)$ values for many semiconductors, depicted in fig. 5 (Bernard et al. 1990). Note that the chalcopyrite structure has the lowest chemical energy, $\varepsilon^{(n)} = \Delta E_{\rm CT}^{(n)} + \Delta E_{\rm REL}^{(n)}$, while the CuPt structure has the highest energy in this series of structures. This reflects the fact that the chalcopyrite structure is able to accommodate dissimilar bond lengths very effectively (Mbaye et al. 1986, 1987), so its $\Delta E_{\rm REL} \ll 0$. Since $\varepsilon^{(n)} < 0$ for lattice-mismatched alloys (fig. 5) one predicts anticlustering. This is illustrated in figs. 6 and 7 (Wei et al. 1990, Ferreira et al. 1989), which show the excess probabilities $\Delta P^{(n)}(x, T)$ of eq. (12), calculated using the energies of fig. 5. In most compositions, the mixed clusters exist in excess of what random probability

Fig. 6. Excess cluster probabilities $P_n(x, T) - P_{\rm R}^{(n)}(x)$ at high temperatures (with respect to the values obtained for a perfectly random (R) alloy) (eq. (12)). Observe the (small) clustering in the size-matched $Al_{1-x}Ga_xAs$ system and the (larger) anticlustering found in the size-mismatched systems (all others). Results are given for the III–V systems whose clusters are denoted (a) $Al_{4-n}Ga_nAs$, (b) $Ga_4As_{4-n}P_n$, (c) $In_{4-n}Ga_nP$, (d) $In_{4-n}Ga_nAs$, and (e) $Ga_4Sb_{4-n}As_n$ for $0 \leqslant n \leqslant 4$. From Wei et al. (1990).

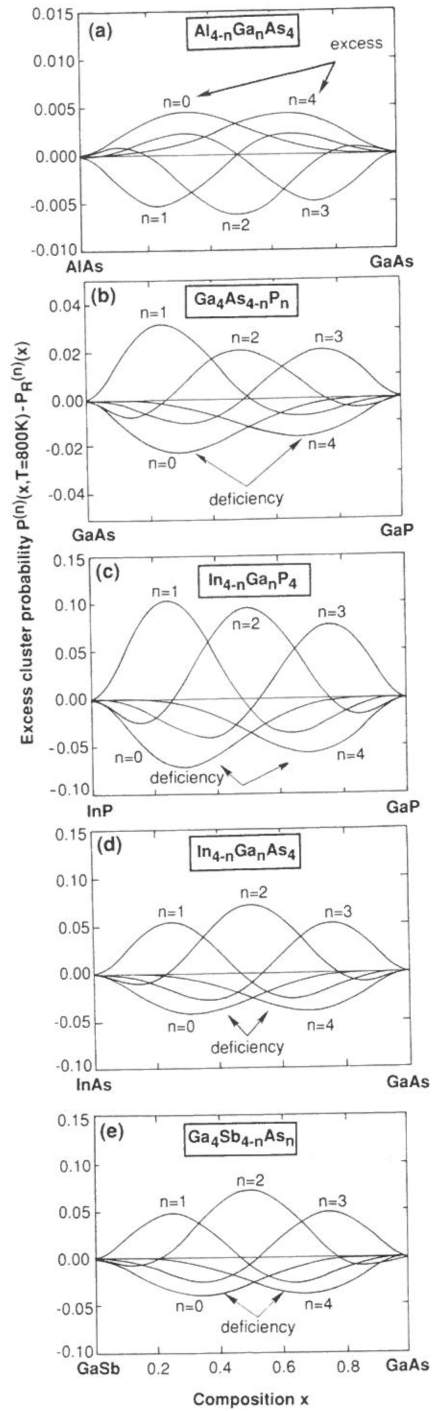

(a)
$Al_{4-n}Ga_nAs_4$
excess
n=0
n=4
n=1
n=2
n=3
AlAs
GaAs
(b)
$Ga_4As_{4-n}P_n$
n=1
n=2
n=3
n=0
n=4
deficiency
GaAs
GaP
(c)
$In_{4-n}Ga_nP_4$
n=1
n=2
n=3
n=0
n=4
deficiency
InP
GaP
(d)
$In_{4-n}Ga_nAs_4$
n=1
n=2
n=3
n=0
n=4
deficiency
InAs
GaAs
(e)
$Ga_4Sb_{4-n}As_n$
n=1
n=2
n=3
n=0
n=4
deficiency
GaSb
GaAs
Excess cluster probability $P^{(n)}(x,T=800K) - P_R^{(n)}(x)$
Composition x

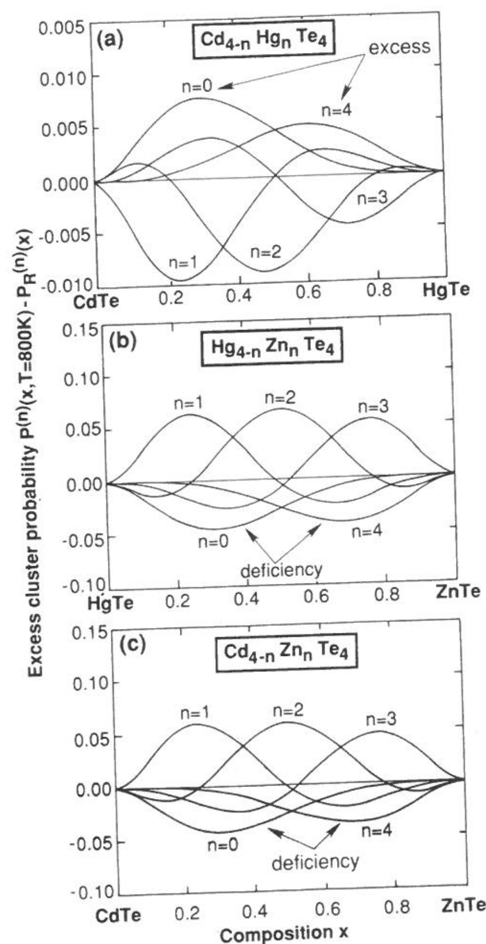

Fig. 7. Same as fig. 6 (see caption), but for the II–VI alloys whose clusters are denoted (a) $Cd_{4-n}Hg_nTe_4$, (b) $Hg_{4-n}Zn_nTe_4$, and (c) $Cd_{4-n}Zn_nTe_4$. From Wei and Zunger (1990).

will grant, while the pure A_4 and B_4 clusters are deficient. In terms of the "clustering parameter" of eq. (14) this means that $\beta < 0$. This is valid when we assume, as we have, that all clusters are coherent with the alloy lattice. If each cluster were to relax to its own free-space equilibrium volume, the energy of the pure clusters could be lowered, so clustering rather than anticlustering could appear. Hence, the stability of clustering versus anticlustering could depend on the detailed chemical and elastic interactions between precipitate clusters and their alloy environment.

(iv) Lattice-matched semiconductor alloys have $G(x) \approx 0$ and a slightly positive chemical energy $\varepsilon^{(n)} \gtrsim 0$. This is shown in the inset of fig. 5. This means that such systems will be close to perfect randomness, with a very small amount of clustering. This is borne out in the calculation shown in fig. 6a for GaAlAs and fig. 7a for CdHgTe.

3. Observation of microscopic deviations from randomness: clustering/anticlustering

We next review the experimental evidence for microscopic clustering/anticlustering. Naturally, only experimental probes that can distinguish the various *local* A_nB_{4-n} clusters are appropriate here. Once the *existence* of such clusters is detected, comparison of their *relative probabilities* with the ideal random values can be used to establish whether clustering or anticlustering takes place.

The existence of local clusters was demonstrated by Samuelson et al. (1984). They doped the $GaAs_{1-x}P_x$ alloy with Cu, thereby creating five different local environments (As_4, As_3P, As_2P_2, AsP_3, and P_4) for the Ga-substituting Cu atom. The 1.36 eV Cu-related luminescence in pure GaAs was observed to split in the alloy into a set of lines correlated with the five local environments. The peak intensities closely followed the random distribution $P_R^{(n)}(x)$ of eq. (11), thus within the accuracy of their experiment, their alloy is random.

Another local probe is provided by the NMR chemical shift. Zax et al. (1987) and Beshah et al. (1987) measured the Te chemical shift in $Hg_{1-x}Cd_xTe$ and $Cd_{1-x}Zn_xTe$, respectively, while Tycko et al. (1992) measured the P chemical shift in $Ga_{1-x}In_xP$ alloys. In all cases, distinct chemical shifts in the common atom due to the different local environments were resolved. Tycko et al. (1992) found for $Ga_{0.14}In_{0.86}P$ the intensity ratio 0.09:0.38:0.53 for In_2Ga_2, In_3Ga, and In_4, respectively, compared with the ideal random values (eq. (11)) of 0.087:0.356:0.547. Hence, there appears to be a small enhancement of the In_3Ga cluster and depletion of the In_4 cluster ("anticlustering", or $\beta < 0$). For vapor-grown $Ga_{0.5}In_{0.5}P$ samples they found a small enhancement of the In_3Ga and $InGa_3$ clusters and depletion of $In_4 + Ga_4$ (also anticlustering). Beshah et al. (1987) found only small deviations from randomness in $Cd_{1-x}Zn_xTe$. For $x = 0.07$ the Cd_3Zn_1 cluster was slightly deficient while for $x = 0.30$ the Cd_4 cluster was deficient.

Zax et al. (1987) first performed measurements on powder samples of $Hg_{0.75}Cd_{0.25}Te$, assigning the chemical shifts (fig. 2 in Zax et al. (1987)) around 200–400 ppm to the Hg_4 clusters, the shift around 500–700 ppm to the Hg_3Cd clusters, and the shift in the intermediate region ($\sim$450 ppm) to Hg_2Cd_2 clusters. The *order* of chemical shifts (using CdTe as a reference) was

$$\sigma(HgCd_3) \leqslant \sigma(Hg_4) < \sigma(Hg_2Cd_2) < \sigma(Hg_3Cd).$$

Comparing their NMR spectra for the Hg-rich sample to simulations assuming perfectly random samples (part b of their fig. 3; note error in this figure caption) they concluded that the Hg_3Cd cluster had an intensity *significantly larger* than that predicted by the simple statistical model of eq. (11). This result conflicted with the thermodynamic calculations of Zunger and Mbaye (1986), Wei and Zunger (1988c), and Wei et al. (1990). Figure 7a depicts these calculated results (note the scale of this figure, indicating that ΔP of eq. (12) is less than 0.005 for this material). The discrepancy between experiment and theory was significant, in that experiment suggested that the chemical energy (eq. (16)) is $\varepsilon(Hg_3Cd) \ll 0$ (strong binding leading to anticlustering) while theory suggested $\varepsilon(Hg_3Cd) \gtrsim 0$. New experiments (Zax et al. 1993) on *single crystals* $Hg_{0.78}Cd_{0.22}Te$ reversed the original peak assignment: the structure

assigned previously to Hg_4 (Zax et al. 1987) is now identified to be due to Hg_2Cd_2 while the structure previously assigned to Hg_2Cd_2 is now due to Hg_4. The corrected order of chemical shifts is now

$$\sigma(HgCd_3) < \sigma(Cd_2Hg_2) < \sigma(Hg_4) < \sigma(Hg_3Cd).$$

This led to the conclusion (Zax et al. 1993) that the Hg_3Cd cluster is *not* in excess of random statistics, while $HgCd_3$ *is* in excess of random statistics, as predicted theoretically earlier (Zunger and Mbaye 1986, Wei and Zunger 1988c, Wei et al. 1990). This is illustrated in table 1.

Additional information on the short-range order can be deduced from X-ray diffuse scattering. Bocchi et al. (1985) found that LPE-grown AlGaAs alloys exhibit nearly perfect randomness, and Kashihara et al. (1989) found similar results for MBE-grown samples. This is expected of lattice-matched systems (fig. 6a) where $\varepsilon^{(n)} \approx 0$ (inset in fig. 5). The results for lattice-mismatched alloys are less clear. Glas (1989a) and Glas et al. (1990) calculated the diffuse scattering features of size-mismatched alloys, finding that the diffuse lines and pseudo-satellites can be explained in terms of the correlated displacements of atoms in an ideal chemically random alloy (zero chemical SRO). Most analyses of diffuse-scattering data do not separate accurately chemical SRO from relaxation effects. Brühl et al. (1977) found in polycrystalline Bridgman-grown GaInP samples significant (13%) *nearest-neighbor clustering*, whereas more recent measurements on LPE-grown $In_{0.53}Ga_{0.47}As$ alloys by Osamura et al. (1987) found *nearest-neighbor anticlustering* and next-nearest-neighbor clustering. Recent measurements by Yasuami et al. (1992) on OMVPE-grown $In_{0.5}Ga_{0.5}P$ and $In_{0.5}Al_{0.5}P$ alloys found anticlustering tendencies. As discussed above, this could reflect in part different coherency conditions: coherent morphology, assumed in figs. 6 and 7, is predicted to lead to anticlustering, while incoherent morphology could lead to clustering. Clearly, more work is needed in establishing the magnitudes and signs of the chemical SRO by diffuse X-ray scattering in high-quality alloys.

While impurity-bound luminescence, NMR chemical shift, and X-ray diffuse scattering provide direct measurements of SRO on a scale of one or so bond lengths, the deduction of truly short-range ordering from optical measurements is somewhat

Table 1
Order of Te chemical shifts $\sigma^{(n)}$ for the various $Hg_{4-n}Cd_n$ clusters in Hg-rich CdHgTe alloys as originally inferred by Zax et al. (1987). This assignment led to the excess probability ΔP (eq. (11)) indicated as "+ +" (excess) and "− −" (deficiency). The new assignment (Zax et al. 1993) reversed the identification of Hg_2Cd_2 and Hg_4. Theoretical predictions (Zunger and Mbaye 1986, Wei and Zunger 1988c, Wei et al. 1990) are also shown.

Zax et al.	(1987)	$\sigma(Cd_4) <$	$\sigma(HgCd_3) \leqslant$	$\sigma(Hg_4) <$	$\sigma(Hg_2Cd_2) <$	$\sigma(Hg_3Cd)$
ΔP	(1987)			− −		+ +
Zax et al.	(1993)	$\sigma(Cd_4) <$	$\sigma(HgCd_3) <$	$\sigma(Hg_2Cd_2) <$	$\sigma(Hg_4) <$	$\sigma(Hg_3Cd)$
σ (ppm)	(1993)		256	410	472	563
ΔP	(1993)		+	−	~0	~0
Theory	(1986, 1989)	0	+	−	~0	~0

less direct. Dimoulas et al. (1990) fitted the lineshape observed in modulated reflection and transmission spectra of InGaAs to a model that permits local clustering, finding that the cluster sizes (< 10 Å) are far smaller than those inferred by TEM. Since, however, this model excludes the possibility of anticlustering, the analysis may be incomplete. Compaan et al. (1990a,b,c) performed resonance Raman experiments on Hg-rich $Hg_{1-x}Cd_xTe$ alloys, finding that the 133 cm^{-1} mode can be associated with anticlustering of Hg_3Cd. Fu and Dow (1987) calculated the phonon spectra, interpreting the 133 cm^{-1} mode as a Hg_3Cd cluster vibration. Sela et al. (1988a,b) have similarly interpreted the frequency splitting of the resonant Raman modes of $Ga_{0.5}Al_{0.5}As$ as reflecting local inhomogeneities on the scale of a sphere with radius 2.3 Å.

Many investigators (Verleur and Barker 1966, Perkowitz et al. 1991, Kozyrev et al. 1983, Yamazaki et al. 1980, Kakimoto and Katoda 1985) have attempted a comparison between the measured vibrational line intensities and those calculated empirically via some spring-constant models, thus deducing an effective clustering parameter β (eq. (14)). Verleur and Barker (1966) fitted the infrared reflectivity of $GaAs_xP_{1-x}$ to a multi-parameter spring model, deducing a huge $\beta = 0.75$. Perkowitz et al. (1991) applied a similar analysis to $CdSe_xTe_{1-x}$, finding $\beta \sim 0.2$–0.5. Kakimoto and Katoda (1985) fit a modified linear chain model to the Raman spectra of $Ga_{0.47}In_{0.53}As$, finding $\beta \approx 0.3$, while Yamazaki et al. (1980) fitted the infrared reflectivity spectra of GaInAs to a twelve-parameter spring-constant model, deducing $\beta \lesssim 0.2$. All of these results ($\beta > 0$, i.e., clustering) conflict with all thermodynamic models of short-range order (e.g., figs. 6 and 7) discussed above. It is not obvious, however, if the conflict is real since (i) the fitted value of β depends on the details of (the rather complex) many-parameter spring-constant models, (ii) the normal vibrational modes extend far beyond the dimension of a cluster, so what is measured in effect is an average over different n-values in $A_{4-n}B_n$, and (iii), as eq. (14) indicates, β represents an average over the true statistical variables $\Delta P^{(1)}$, $\Delta P^{(2)}$, and $\Delta P^{(3)}$. Direct fits of the vibrational spectra to these *three* variables rather than to an averaged β could reveal more directly if the data supports clustering or anticlustering. A recent *direct* measurement (Ramos et al. 1993) of the distribution of chalcogen atoms in CdS_xSe_{1-x} using X-ray absorption revealed negligible deviations from randomness. Thus, the current analysis of the IR data producing large clustering values could be incorrect.

Having described the observations of microscopic short-range clustering/anticlustering, we turn next to describe observations of macroscopic, spinodal-type phase separation in bulk and epitaxial alloys.

4. Macroscopic nonrandomness: phase separation

4.1. *Observations of phase separation*

As will become clear later on in this section, the observations of phase separation in III–V alloys are complicated by the fact that different growth geometries and growth sequences lead to different effects. These are often confused in the literature.

We start therefore by summarizing the "big picture" on observations of phase separation in semiconductor alloys and provide details later on.

We first distinguish phase separation seen in *bulk-grown* samples (e.g., melt growth) from that seen in *epitaxially grown* samples (e.g., LPE, VPE, MBE). Second, phase separation in epitaxially grown samples appears either as (i) "lateral phase separation" seen in the substrate plane (i.e., perpendicular to the growth direction) or as (ii) "vertical phase separation" seen perpendicular to the substrate plane (i.e., parallel to the growth direction). Lateral phase separation is seen in different growth modes, each exhibiting its own characteristics. This includes: (a) homogeneous growth, where the three elements A, B, and C of $A_{1-x}B_xC$ are deposited simultaneously. (b) Mobility enhanced growth, where the group III *elements* A and B are deposited first, followed by deposition of the group V element (while the flux of group III elements is shut off). (c) Superlattice growth, where the binary compounds AC and BC are deposited sequentially. Vertical phase separation is seen under homogeneous alloy growth.

We start by discussing phase separation in *bulk-grown* semiconductor alloys. Here there is no substrate, and the alloy is grown most often from the melt, rather than from the vapor phase. In 1953, Shih and Peretti (1953) noted that the InAs–InSb system had a maximum terminal solid solution of only 2%, while Koster and Thoma (1955) found in 1955 similar evidence for insolubility in GaSb–InSb, AlSb–InSb, and even AlSb–GaSb. It was later realized that in most of these cases true thermal equilibrium was not reached. The first demonstration of equilibrium solid solutions in III–V alloys came from the work of Goryunova and Federova (1955), who found that after prolonged annealing GaSb–InSb reached a single-phase condition while GaAs–InAs exhibited equilibrium phase separation. Woolley's review (1962) of bulk growth of III–V alloys demonstrates how the methods of prolonged powder annealing, zone recrystallization, and zone casting lead in many cases to solid solutions, yet alloys with a large size mismatch show significant regions of phase separation (e.g., InAs–InSb), observable in X-ray diffraction. These measurements reflect the closest one can approach true bulk equilibrium. The calculated phase diagrams of fig. 4 represent the theoretical version of such situations. The recent careful bulk annealing experiments of Ishida et al. (1988) for GaSb–GaAs, reproduced as open circles in fig. 4e, demonstrate significant phase separation. In fact, phase separation is so pronounced in bulk-grown alloys that some alloys cannot even be mixed in the bulk state (e.g., GaP–GaSb or InP–InSb).

With the advent of epitaxial growth methods (e.g., liquid phase epitaxy, or LPE) it was first thought that the problem of phase separation was avoided. It was later realized, however, that phase separation is reduced, but not eliminated by low-T epitaxial growth. Following the initial observation of Henoc et al. (1982) on phase separation in InGaAsP layers grown by LPE on (001) InP substrates, several investigators have reported similar results (Glas et al. 1982, Launois et al. 1982, Mahajan et al. 1984a, 1989, Ueda et al. 1984, 1988, Chu et al. 1985, Norman and Booker 1985, Treacy et al. 1985, Cherns et al. 1987, Shahid et al. 1987, Shahid and Mahajan 1988, Glas 1989b, Mahajan and Shahid 1989, Okuda et al. 1990, McDevitt et al. 1990, 1992, Peiro et al. 1991). These studies encompass layers grown by (i) LPE (Launois et al. 1982, Mahajan et al. 1984a, Ueda et al. 1984, Norman and Booker

We start therefore by summarizing the "big picture" on observations of phase separation in semiconductor alloys and provide details later on.

We first distinguish phase separation seen in *bulk-grown* samples (e.g., melt growth) from that seen in *epitaxially grown* samples (e.g., LPE, VPE, MBE). Second, phase separation in epitaxially grown samples appears either as (i) "lateral phase separation" seen in the substrate plane (i.e., perpendicular to the growth direction) or as (ii) "vertical phase separation" seen perpendicular to the substrate plane (i.e., parallel to the growth direction). Lateral phase separation is seen in different growth modes, each exhibiting its own characteristics. This includes: (a) homogeneous growth, where the three elements A, B, and C of $A_{1-x}B_xC$ are deposited simultaneously. (b) Mobility enhanced growth, where the group III *elements* A and B are deposited first, followed by deposition of the group V element (while the flux of group III elements is shut off). (c) Superlattice growth, where the binary compounds AC and BC are deposited sequentially. Vertical phase separation is seen under homogeneous alloy growth.

We start by discussing phase separation in *bulk-grown* semiconductor alloys. Here there is no substrate, and the alloy is grown most often from the melt, rather than from the vapor phase. In 1953, Shih and Peretti (1953) noted that the InAs–InSb system had a maximum terminal solid solution of only 2%, while Koster and Thoma (1955) found in 1955 similar evidence for insolubility in GaSb–InSb, AlSb–InSb, and even AlSb–GaSb. It was later realized that in most of these cases true thermal equilibrium was not reached. The first demonstration of equilibrium solid solutions in III–V alloys came from the work of Goryunova and Federova (1955), who found that after prolonged annealing GaSb–InSb reached a single-phase condition while GaAs–InAs exhibited equilibrium phase separation. Woolley's review (1962) of bulk growth of III–V alloys demonstrates how the methods of prolonged powder annealing, zone recrystallization, and zone casting lead in many cases to solid solutions, yet alloys with a large size mismatch show significant regions of phase separation (e.g., InAs–InSb), observable in X-ray diffraction. These measurements reflect the closest one can approach true bulk equilibrium. The calculated phase diagrams of fig. 4 represent the theoretical version of such situations. The recent careful bulk annealing experiments of Ishida et al. (1988) for GaSb–GaAs, reproduced as open circles in fig. 4e, demonstrate significant phase separation. In fact, phase separation is so pronounced in bulk-grown alloys that some alloys cannot even be mixed in the bulk state (e.g., GaP–GaSb or InP–InSb).

With the advent of epitaxial growth methods (e.g., liquid phase epitaxy, or LPE) it was first thought that the problem of phase separation was avoided. It was later realized, however, that phase separation is reduced, but not eliminated by low-T epitaxial growth. Following the initial observation of Henoc et al. (1982) on phase separation in InGaAsP layers grown by LPE on (001) InP substrates, several investigators have reported similar results (Glas et al. 1982, Launois et al. 1982, Mahajan et al. 1984a, 1989, Ueda et al. 1984, 1988, Chu et al. 1985, Norman and Booker 1985, Treacy et al. 1985, Cherns et al. 1987, Shahid et al. 1987, Shahid and Mahajan 1988, Glas 1989b, Mahajan and Shahid 1989, Okuda et al. 1990, McDevitt et al. 1990, 1992, Peiro et al. 1991). These studies encompass layers grown by (i) LPE (Launois et al. 1982, Mahajan et al. 1984a, Ueda et al. 1984, Norman and Booker

1985, Treacy et al. 1985, McDevitt 1990, McDevitt et al. 1990, 1992), (ii) vapor phase epitaxy (VPE) (Chu et al. 1985), (iii) vapor levitation epitaxy (VLE) (Shahid et al. 1987, Shahid and Mahajan 1988, Mahajan et al. 1989), (iv) organometallic vapor phase epitaxy (OMVPE) (Mahajan and Shahid 1989, Ueda et al. 1988, 1989a,b, McDevitt et al. 1990), and (v) molecular beam epitaxy (MBE) (Ueda et al. 1989a, McDevitt et al. 1992). Direct local chemical X-ray microanalysis (Henoc et al. 1982, Glas et al. 1982, Glas 1989b, Cherns et al. 1987) have clearly demonstrated phase separation.

4.2. *Bulk versus epitaxial phase separation*

Our foregoing discussion distinguished bulk-grown crystals from epitaxially grown crystals. The thermodynamic difference between these cases can be appreciated as follows: imagine (Zunger and Wood 1989, Wood and Zunger 1989) that an alloy $\alpha_x\beta_{1-x}$ were grown epitaxially on an exactly lattice-matched substrate, and that in bulk form $\Delta E_{\rm mix} \geqslant 0$, as is the case for III–V alloys (Stringfellow 1974). As a concrete example, take $Ga_{0.5}In_{0.5}P$ grown on GaAs (001). As long as the alloy is homogeneous, its energy does not depend on its thickness, since, by assumption, it is perfectly lattice matched with the substrate. This is depicted by the horizontal lines marked $\alpha\beta$ in fig. 8a. Now when the alloy starts to phase separate (by way of a thought-experiment) into α-rich and β-rich domains, these species could initially be coherent with the substrate. In our concrete example this corresponds to GaP-on-GaAs (001) plus InP-on-GaAs (001). These coherent phase-separated species are highly strained due to the large mismatch with the substrate. This raises the energy of *epitaxial* $\alpha+\beta$ relative to the homogeneous compound $\alpha\beta$ as shown in fig. 8 under the heading "thin epi". The internal energy of the system is no longer given by $\Delta E_{\rm mix}$ of eq. (2), but rather by

$$\Delta E_{\rm epi}(a_{\rm s}, x) = \Delta E_{\rm mix}(x) + \Delta E_{\rm SS}(a_{\rm s}, x), \tag{17}$$

where the substrate strain (SS) energy is

$$\Delta E_{\rm SS}(a_{\rm s}, x, \hat{G}) = K_{\alpha\beta}(a_{\rm s} - a_{\alpha\beta})^2 - xK_\alpha(a_{\rm s} - a_\alpha)^2 - (1-x)K_\beta(a_{\rm s} - a_\beta)^2. \tag{18}$$

Here $K_\alpha = \frac{9}{8}q_\alpha(\hat{G})B_\alpha a_\alpha$, where $q_\alpha(\hat{G})$ is the orientation ($\hat{G}$) dependent elastic constant (Zunger and Wood 1989), B_α is the bulk modulus, and a_α, a_β, and $a_{\rm S}$ are the lattice constants of α, β, and the substrate, respectively. Figure 8a illustrates schematically the situation for lattice-matched films, i.e., $a_{\rm s} = a_{\alpha\beta}$, while fig. 8b shows the results when the homogeneous phase $\alpha\beta$ is mismatched with respect to the substrate. In fig. 8a the energy of the lattice-matched alloy $\alpha\beta$ does not depend on the film thickness (since it is lattice matched to the substrate), but the energy of the phase-separated components $\alpha+\beta$ does. If the constituents α and β are strongly mismatched with the substrate, $\Delta E_{\rm SS} \ll 0$, *so in an extreme case it is possible that* $\Delta E_{\rm epi} < 0$ *despite* $\Delta E_{\rm mix} > 0$ *in the bulk*. This leads to an epitaxial reduction in the miscibility gap temperature. After a (Matthews–Blakeslee) critical thickness $h_{\rm c}$, the phase-separated system $\alpha+\beta$ starts to develop misfit dislocations, lowering its energy towards the fully relaxed bulk value (our zero of energy), as shown on the right side of fig. 8a.

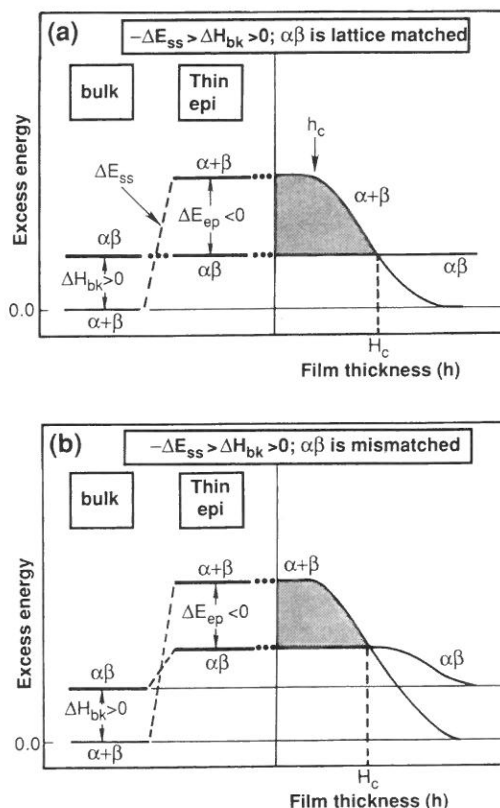

Fig. 8. Schematic plot of bulk and epitaxial energies when $-\Delta E_{ss} > \Delta H_{bk}$. The left part shows energies for thin ($h \ll h_c$) films while the right-hand side shows results as a function of thickness. Here (a) is for $a_{\alpha\beta} = a_s$, while (b) is for $a_{\alpha\beta} \neq a_s$. Note the crossing of the energies of bulk and epitaxial systems at the thickness $H_c \neq h_c$. The shaded area denotes regions where the homogeneous phase $\alpha\beta$ is stabler than the phase-separated constituents $\alpha + \beta$. From Zunger and Wood (1989).

However, the homogeneous alloy $\alpha\beta$ continues to be the lowest-energy state until a larger thickness H_c. At this point, dislocations lower the energy of $\alpha + \beta$ sufficiently to make this phase-separated system the ground state. These considerations show that epitaxial coherency with the substrate can lower the miscibility gap temperature depending on the layer thickness and the value of H_c. A *qualitative* description of the epitaxial lowering of the miscibility gap temperature (Larche et al. 1988, Zunger and Wood 1989, Chiang and Johnson 1989) can be obtained by making a few simplifying assumptions. Suppose that the film's lattice constant $a_{\alpha\beta}(x) = a(x)$ follows Vegard's rule, and that the substrate itself is an alloy with fixed composition X_s and lattice parameter $a_s = a(X_s)$. The substrate strain energy of eq. (18) is then

$$\Delta E_{SS}(X_s x, \hat{G}) = (a_\beta - a_\alpha)^2[K(x)(x - X_s)^2 - K_\alpha x(1 - X_s)^2 - K_\beta(1 - x)X_s^2], \quad (19)$$

where $K_{\alpha\beta} = K(x)$, K_α, and K_β depend on the film's orientation $\hat{G}$. The miscibility

temperature is given by the zero of the second compositional derivative of $\Delta E_{epi} - TS$. For simplicity, assume that the entropy S is just the *ideal* mixing entropy and that the bulk energy ΔE_{mix} is given by the regular-solution model $\Omega x(1-x)$. Then, at $x = \frac{1}{2}$

$$T_{MG} = \frac{\Omega}{2R} - (a_\beta - a_\alpha)^2 \frac{K(x)}{2R} - \frac{(a_\beta - a_\alpha)^2 (x - X_s)}{4R} [K''(x)(x - X_s) + 4K'(x)], \tag{20}$$

where R is the gas constant and K' and K'' are the first and second compositional derivatives of K. The terms in eq. (20) have the following meaning:

(1) The first term of eq. (20) denotes the bulk T_{MG}. Since $\Omega > 0$ and Ω is proportional to $(a_\beta - a_\alpha)^2$, the MG temperature is large in size-mismatched alloys, e.g., fig. 4. This term has been considered by Panish and Ilegems (1972), de Cremoux et al. (1981), de Cremoux (1982), and Stringfellow (1982a) and leads often to an overestimation of T_{MG}.

(2) The second term in eq. (20) denotes the lowering of T_{MG} due to coherent strains. This lowering is proportional to the size-mismatch $|a_\beta - a_\alpha|^2$ and to the elastic stiffness $K(x) = \frac{9}{8} q(\hat{G}) B(x) a(x)$. Such effects exist even for a lattice-matched $(x = X_s)$ case. A similar term has been considered by Cahn (1961) for bulk alloys and has been applied to lattice-matched epitaxy by de Cremoux (1982), Stringfellow (1982b), and Glas (1987). It often leads to $T_{MG} < 0$, in contradiction with many experiments. Glas (1987) has corrected this term due to lateral composition modulation and surface effects, finding that this correction leads to positive T_{MG}, in better agreement with experiment. He neglected, however, the last term of eq. (20).

(3) The last term is substrate dependent and appears only for $x \neq X_s$. It involves a (generally small) $(a_\beta - a_\alpha)^2 (x - X_s)^2 K''$ term as well as a larger term $(a_\beta - a_\alpha)^2 (x - X_s) K'$, which combines coherency strain with elastic modulus effects. The latter term changes sign as x crosses the lattice-matched composition X_s. This type of term has been included by Larche et al. (1988), Johnson and Chiang (1988), Chiang and Johnson (1989), Wood and Zunger (1989), Zunger and Wood (1989), and Wood (1992), leading to finite T_{MG} values that are below the bulk $\Omega/2R$ value. This shows how epitaxial growth leads to enhanced solubility (reduced phase separation) relative to (incoherent) bulk growth.

The simple model discussed above gives the essential physics of epitaxy but neglects nonideal entropy, the dependence of the equilibrium composition x on strain ("lattice latching"), deviations from Vegard's rule, and uses a simplified regular-solution model. All these approximations were avoided in the work of Mbaye et al. (1986, 1988), Wood and Zunger (1988a,b, 1989), and Zunger and Wood (1989). Figure 9 (Wood 1992) illustrates how coherent epitaxial conditions lower dramatically T_{MG} relative to the (incoherent) bulk *and even expose the bulk-metastable chalcopyrite (CH) phase as epitaxially stable.* Experimental illustrations of enhanced solubilities in epitaxial systems relative to their bulk counterparts include GaP–GaSb (Jou et al. 1988), BaF_2–CaF_2 (Sullivan et al. 1982), and PbS–CdS (Sood et al. 1978). While the detailed microstructure is not known (i.e., whether some two-phase regions exist),

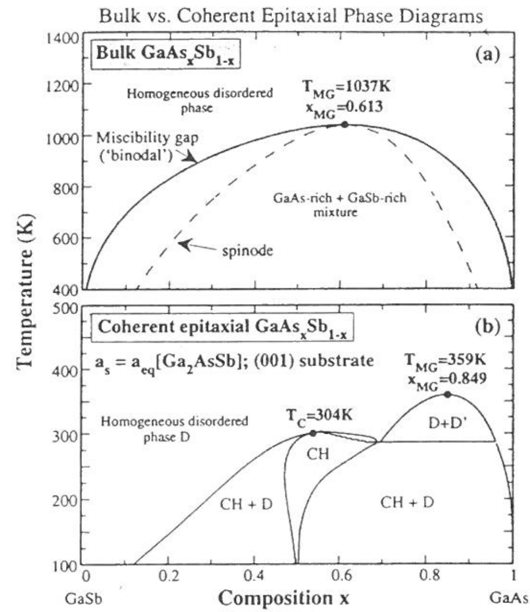

Fig. 9. Calculated (x, T) phase diagrams for $GaAs_xSb_{1-x}$ under bulk (a) and coherent epitaxial conditions on a (001) substrate lattice-matched to $GaAs_{0.5}Sb_{0.5}$ (b). D and D′ indicate disordered phases of distinct compositions. "Spinode" in (a) indicates limits of metastability of the homogeneous disordered phase. Note that epitaxy lowers dramatically the miscibility gap temperature and introduces a stable ordered chalcopyrite structure CH. From Wood (1992).

these examples do demonstrate that coherent epitaxy could stabilize the homogeneous phase relative to bulk, thus diminishing phase separation.

This discussion shows that when the phase-separated precipitates are *fully coherent* with the substrate, their energy increases, so the miscibility gap temperature is reduced (but does not vanish, see fig. 9). We label this as the "coherent MG temperature" T^{C}_{MG}. If, however, full coherence cannot be established during growth, the precipitates will relax to their own "natural" lattice parameters. This will lower their energy, thus raise the miscibility gap temperature. We label this "incoherent MG temperature" as T^{IC}_{MG}. Thus, depending on growth, one could imagine two limits: high-T^{IC}_{MG} for incoherent growth (relaxed precipitates) and low-T^{C}_{MG}. for coherent growth (strained precipitates). The degree of phase separation observed will naturally depend on the extent of coherency of the microstructures established during growth.

With these qualifications, we next describe the experimental observations of phase separation.

4.3. *Microstructure of phase-separated epitaxial layers*

We distinguish here phase separation (PS) observed in the substrate plane (lateral PS) from that occurring perpendicular to the substrate plane (vertical PS). These are discussed separately.

4.3.1. Phase separation in the substrate plane (lateral PS)

Here we distinguish experiments where all of the elements A, B, and C of the alloy are deposited simultaneously ("homogeneous growth") from experiments where one deposits AC/BC in a cyclical manner ("superlattice growth") or deposition of the cations A + B while the anion flux is shut off ("mobility enhanced" epitaxy).

Figure 10 shows a series of dark-field electron micrographs obtained from a (001) InGaAsP layer grown by homogeneous LPE; the layer emits at 1.3 μm (McDevitt et al. 1992). *Both coarse and fine-scale composition modulations are visible.* It can be discerned from fig. 10 that the coarse modulations lie along the [100] and [010] substrate directions and that the principal strains associated with the fine-scale modulations are parallel to the directions along which they are aligned, i.e., [100] and [010]. These results are consistent with those of Mahajan et al. (1984a) and Norman and Booker (1985) on InGaAsP epitaxial layers grown by LPE. We will discuss separately the fine-scale and coarse contrast modulations.

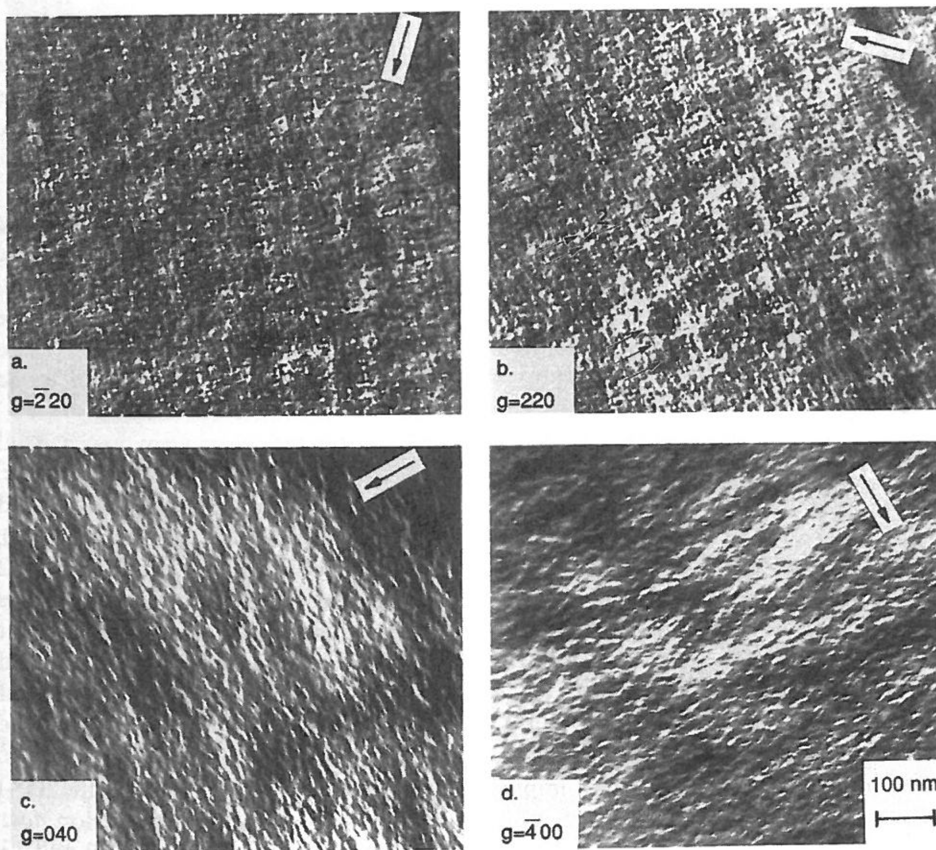

Fig. 10. Series of dark-field electron micrographs obtained from a (001) $In_{1-x}Ga_xAs_yP_{1-y}$ epitaxial layer grown by LPE; the emission wavelength of the layer is 1.3 μm. The operating reflections in (a), (b), (c), and (d) are, respectively, ($\bar{2}$20), (220), (040), and ($\bar{4}$00). From McDevitt (1990).

4.3.1.1. Fine-scale contrast. These were seen early on by Roberts et al. (1981), Henoc et al. 1982, Norman and Booker (1985), and Gowers (1983). Glas (1989b) and Glas et al. (1990) argue that the main features of the fine-scale contrast can be explained by atomic relaxation in a perfectly homogeneous random alloy, without assuming composition modulations. However, the presence of sharp satellites (Norman and Booker 1985) cannot be explained in terms of a perfectly random atomic arrangement. McDevitt et al. (1992) and Mahajan et al. (1984a) suggested that the fine-scale modulations in fig. 10 are due to phase separation. This is consistent with the electron diffraction pattern shown in fig. 11. The satellite reflections contiguous to the (200) and (020) reflections are observed; see the enlarged region in the lower right-hand corner in fig. 11. These satellites appear as lobes of intensity along the [100] and [010] directions. Using the following expression, the periodicity of the modulations (λ) can be determined from fig. 11:

$$\lambda = \frac{a}{\sqrt{h^2 + k^2 + l^2}} \frac{|\boldsymbol{g}|}{|\Delta \boldsymbol{g}|}, \tag{21}$$

where a is the lattice parameter of the solid solution and $|\boldsymbol{g}|/|\Delta \boldsymbol{g}|$ is the ratio of the distances from the transmitted spot to the diffracted spot whose Miller indices are (hkl) and from the satellite to the diffracted spot. The application of eq. (21) to the results in fig. 11 gives $\lambda = 70$ Å; this correlates well with the measured value of $\lambda =$ 80 Å from fig. 10.

Mackenzie et al. (1991) have investigated the compositional homogeneity of GaInAs, AlInAs, and GaAlInAs layers, grown on InP substrates by OMVPE, using pulsed-laser atom probe techniques. All samples showed fine-scale TEM contrast. Some of the samples show distinct deviations from compositional uniformity, on a scale of typically 100–200 Å, from the mean, lattice-matched composition by up to 5 at%. These results are compatible with the above assessment that the fine-scale speckle structure results from phase separation.

There is a remarkable similarity between the microstructures seen in epitaxial layers grown by LPE, VPE, OMVPE, and MBE (Chu et al. 1985, Ueda et al. 1989a,b, McDevitt 1990). Figure 12 shows plan-view dark-field micrographs obtained from (a) InGaAsP and (b) InGaAs layers (emitting at 1.2 and 1.65 µm, respectively); both grown by OMVPE. Comparing figs. 10 (InGaAsP grown by LPE) and 12 (InGaAsP grown by OMVPE) it is apparent that the phase-separated microstructures in the layers grown by different methods are very similar. The preceding assessment is also borne out by an examination of the $\langle 110 \rangle$ cross sections of layers deposited by different techniques. Figures 13, 14, and 15 show, respectively, the cross-sectional micrographs obtained from LPE-, OMVPE-, and VPE-grown InGaAsP films. The speckle structure, suggestive of phase separation, is observed in all the three cases. In addition, if fine-scale contrast implies phase separation, its absence for the (004) reflection in figs. 13b, 14b, and 15 indicates that this type of phase separation *does not occur along the growth* [001] *direction.* Combining the results of figs. 10 and 13 it can be inferred that the phase separation in layers grown on (001)-oriented substrates is two-dimensional in nature and occurs along the directions lying in the growth plane.

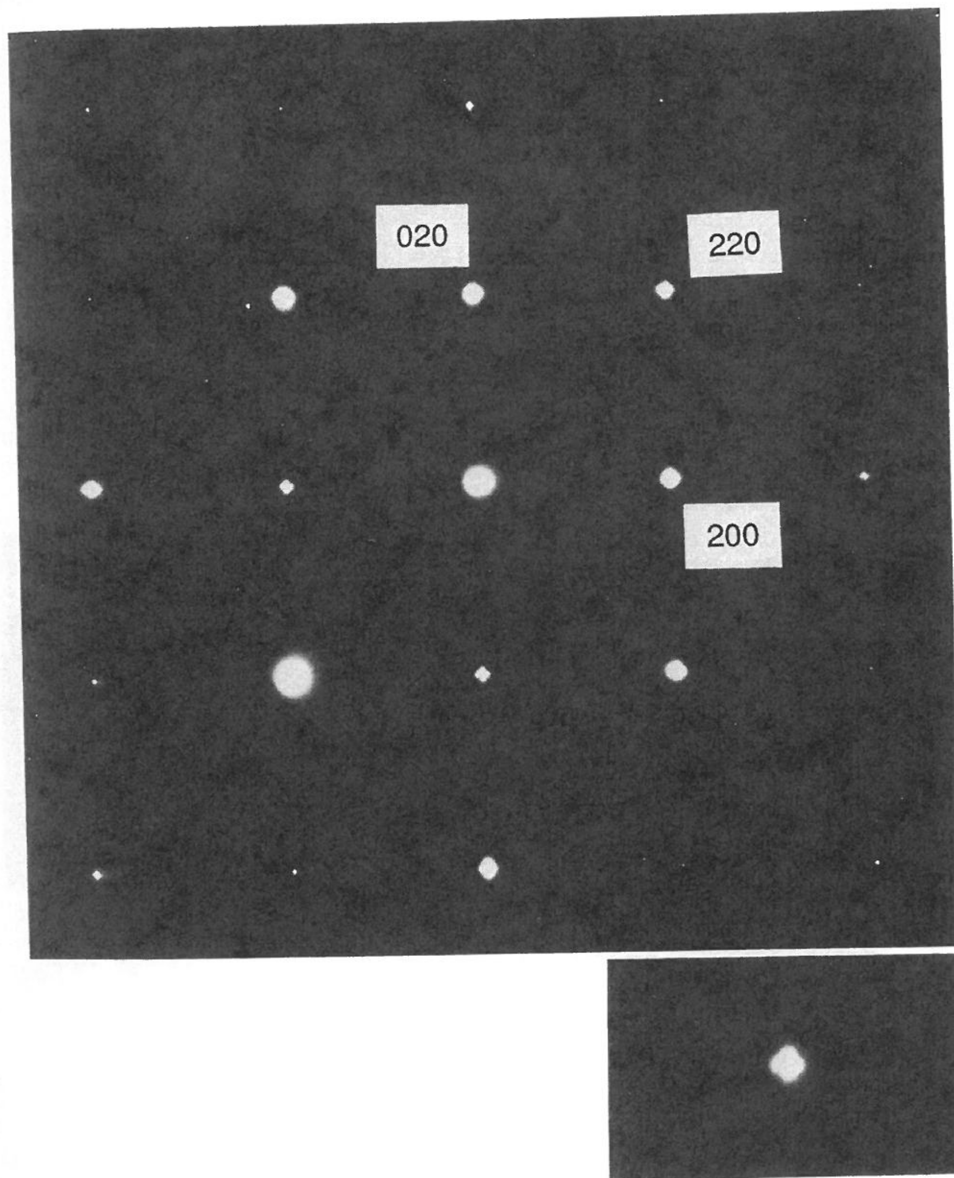

Fig. 11. The (001) diffraction pattern obtained from the layer shown in fig. 10. The pattern shows satellites in the vicinity of (220), (020), and higher-order spots that result from the alignment of periodic fine-scale contrast modulations. One of the highest-ordered spots is enlarged at the lower right-hand corner to show detail. From McDevitt (1990).

To assess the generic validity of the above result, McDevitt (1990) and McDevitt et al. (1992) have examined InGaAsP epitaxial layers deposited by LPE on (110), $(111)_A$, and (123) InP substrates using transmission electron microscopy; the emission

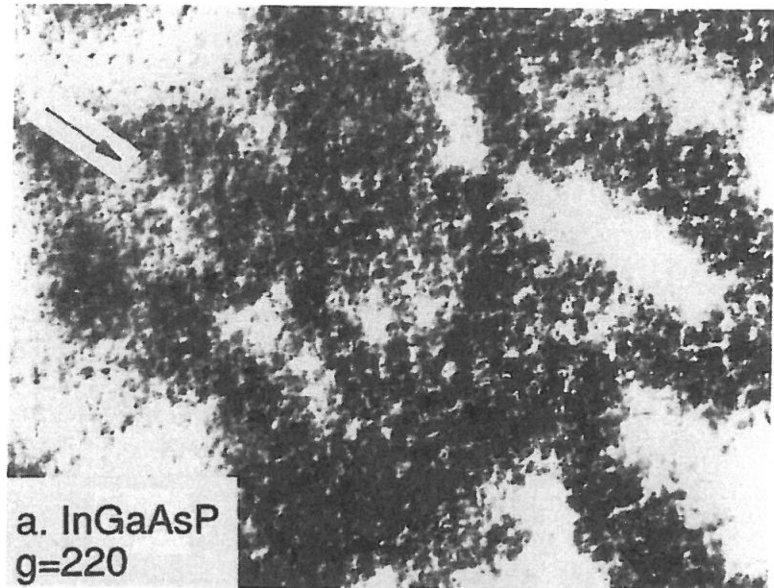

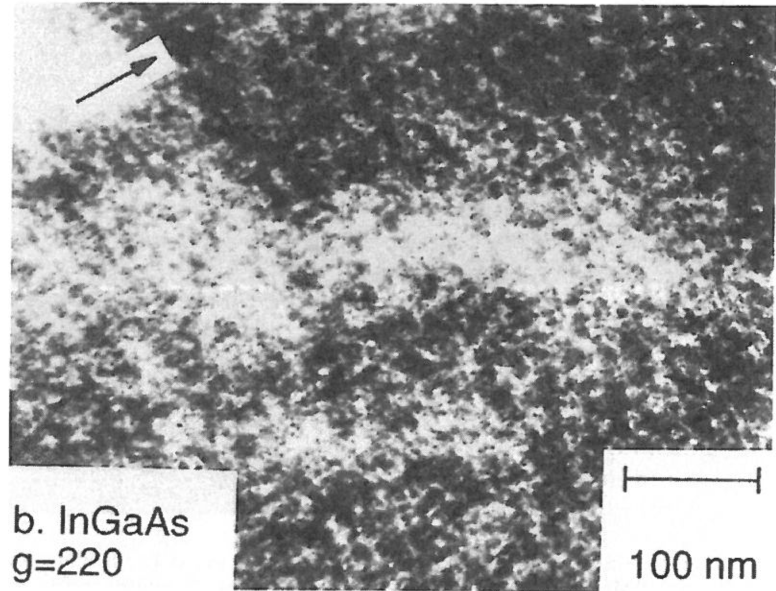

Fig. 12. Plan-view dark-field TEM micrographs from (a) InGaAsP $\lambda = 1.2$ μm and (b) InGaAs $\lambda = 1.65$ μm, MOCVD-grown films. Both images taken with $g = 220$. From McDevitt (1990).

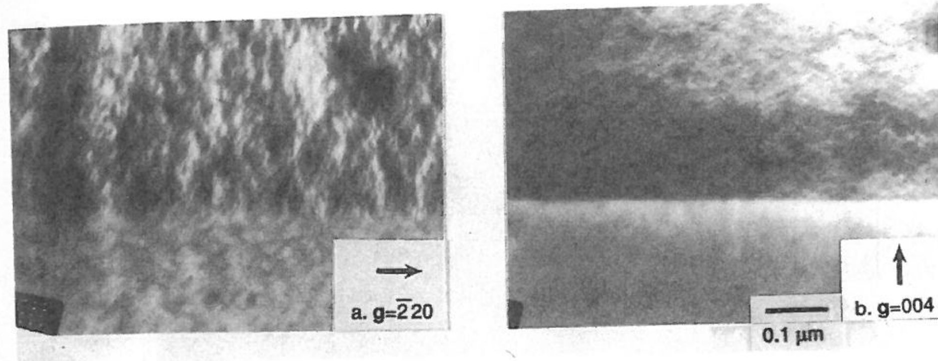

Fig. 13. Dark-field micrographs obtained from a cross section of a (001) LPE-grown $In_{1-x}Ga_xAs_yP_{1-y}$ layer. The operating reflections in (a) and (b) are ($\bar{2}$20) and (004), respectively. These images demonstrate the absence of decomposition along the growth direction. Marker represents 50 nm. From McDevitt (1990).

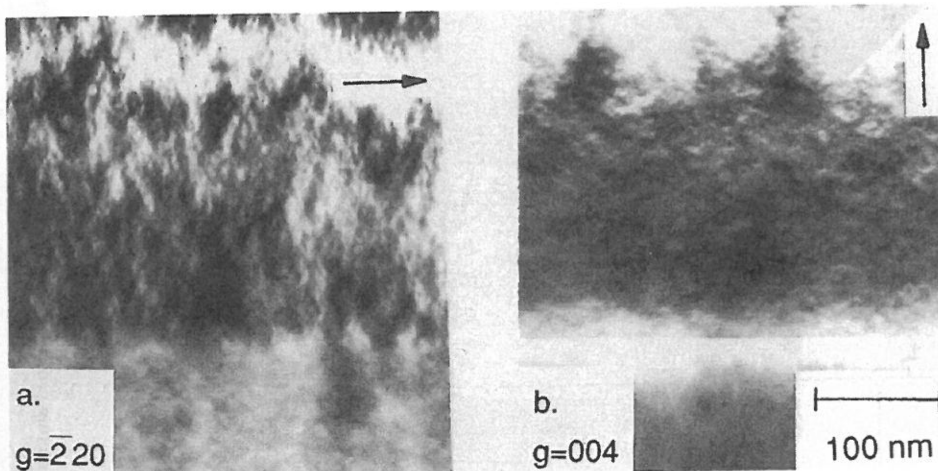

Fig. 14. Dark-field micrographs from a (110) cross section of a (001) MOCVD-grown InGaAsP specimen. From McDevitt (1990).

wavelength of the layer in each case was 1.3 μm. Figure 16 summarizes their results. It is clear that the observed microstructure exhibits a strong dependence on the orientation of the underlying substrate and that in each case phase separation is two-dimensional in nature. The directions along which phase separation occurs are [001] and [1$\bar{1}$0] for the (110) substrate, [30$\bar{1}$] and [0$\bar{3}$2] for the (123) substrate, whereas phase separation is isotropic for the $(111)_A$ substrate. The respective wavelengths along different directions for the three orientations are: 6[001] and 5[1$\bar{1}$0] for the (110) substrate, 9[$\bar{3}$01] and 25[0$\bar{3}$2] for the (123) substrate, and 3 nm for the (111) substrate. Results for the (110) substrate are compatible with those seen by Ueda et al. (1989a,b) in phase-separated GaInP layers grown by OMVPE on (110) GaAs.

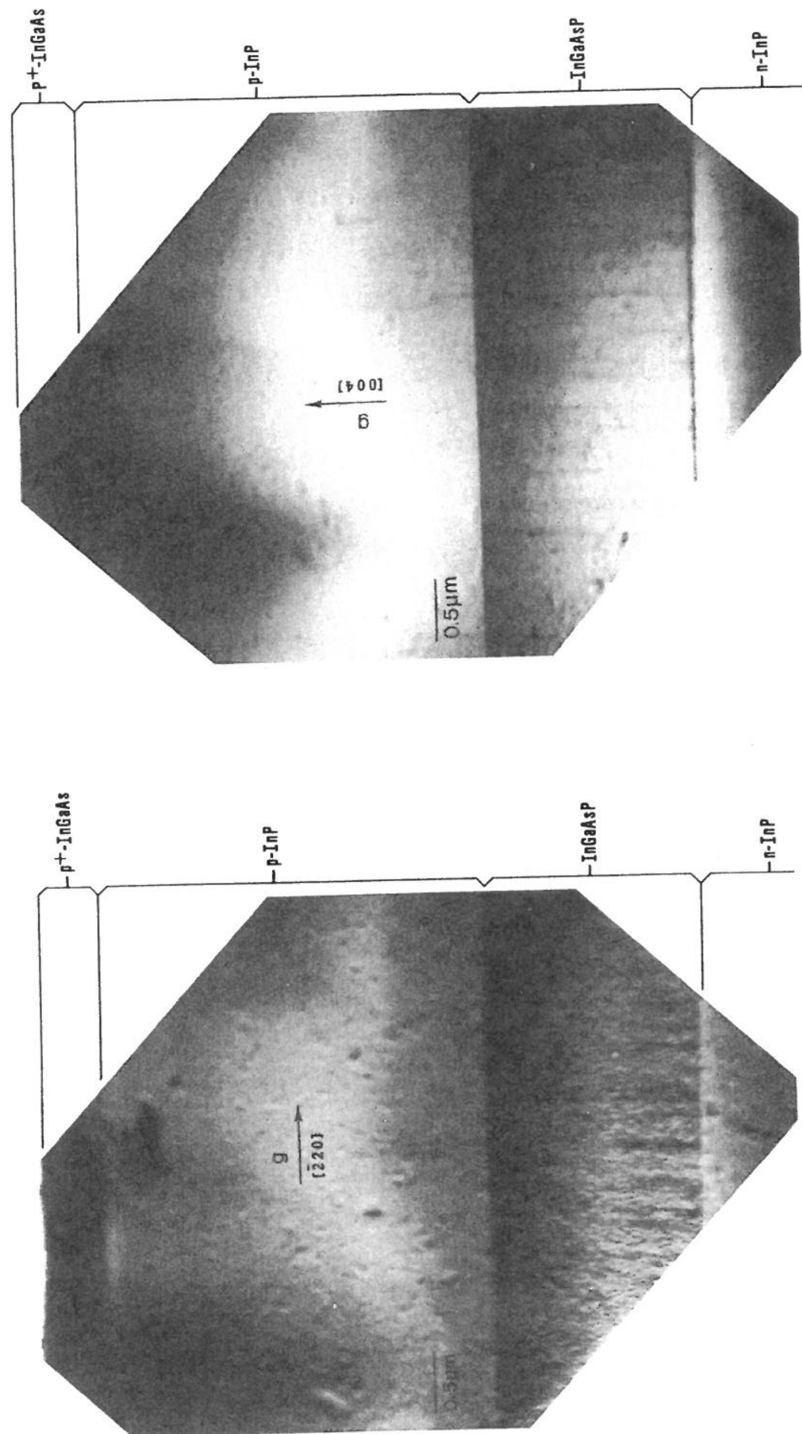

Fig. 15. XTEM micrographs of a four-layer LED structure grown by VPE; operating reflections in left and right part are ($\bar{2}20$) and (004), respectively. From Chu et al. (1985).

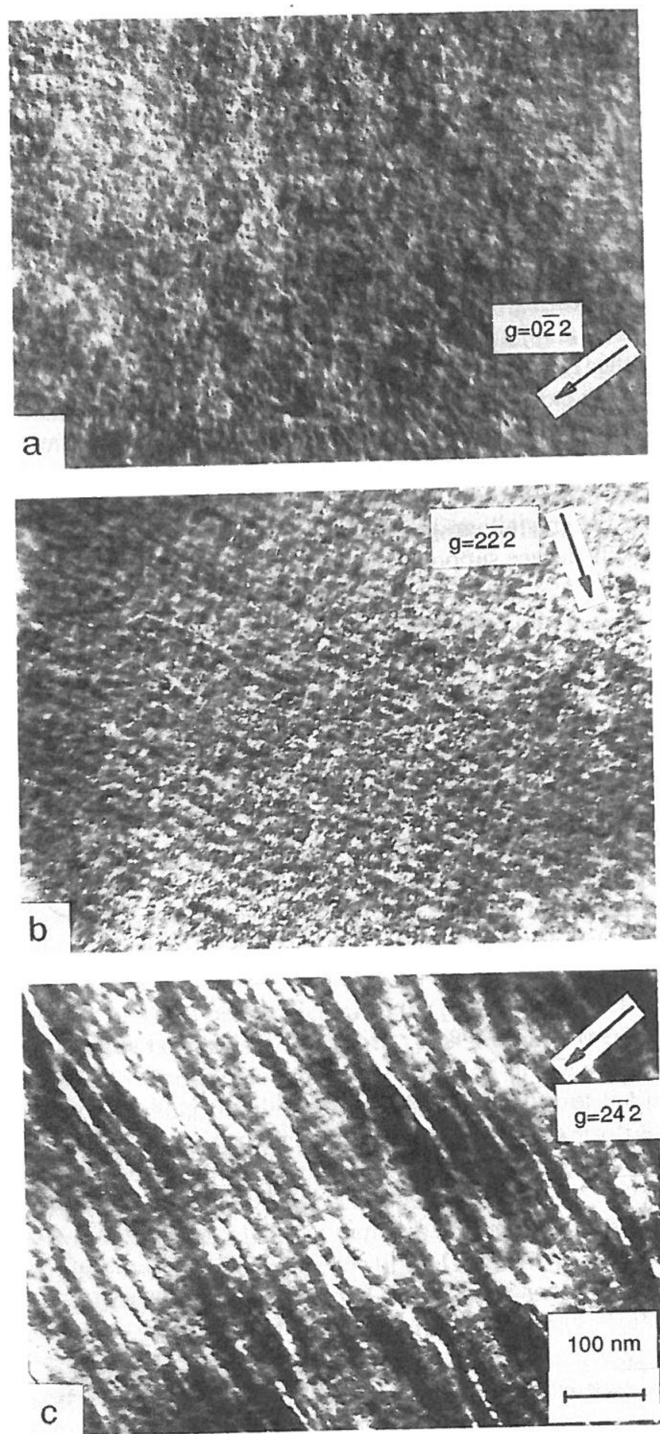

Fig. 16. Micrographs showing orientation dependence of phase-separated microstructures observed in InGaAsP layers (emission wavelength 1.3 μm) grown by LPE on InP substrates: (a) (111), (b) (110), and (c) (123). From McDevitt et al. (1992).

To understand the relationship between substrate orientation and the direction of phase separation, McDevitt et al. (1992) have computed the elastic work associated with the occurrence of phase separation along different directions in the (001), (110), (123), and $(111)_A$ planes of InP at a 600°C growth. This follows along the lines of the work of Cahn (1961) (the energy associated with the coherent deformation of the substrate or with the relaxation of the free surface are neglected here, see Glas and Henoc (1987)). The relative values of the elastic work were normalized to a [100] modulation on the (001) surface. Results of this computation are summarized in fig. 17. The plot for the (001) substrate shows "rounded cusps" along the [100] and [010] direction indicating that modulations along these directions require minimum elastic energy. The (110) substrate plot shows minima along the [001] and [$1\bar{1}0$] direction while the (123) substrate shows minima along the [$30\bar{1}$] and [$0\bar{3}2$] direction. The (111) substrate exhibits elastic isotropy. It is apparent from the agreement of this calculation with experiment that the direction of phase separation is correlated with the directions in the substrate surface along which the coherent strain energy is minimum, i.e., with the soft directions in the growth surface (Cahn 1961). The observation that the crystallography of the modulations is determined by the anisotropy of the growth surface supports the premise that phase separation occurs at the

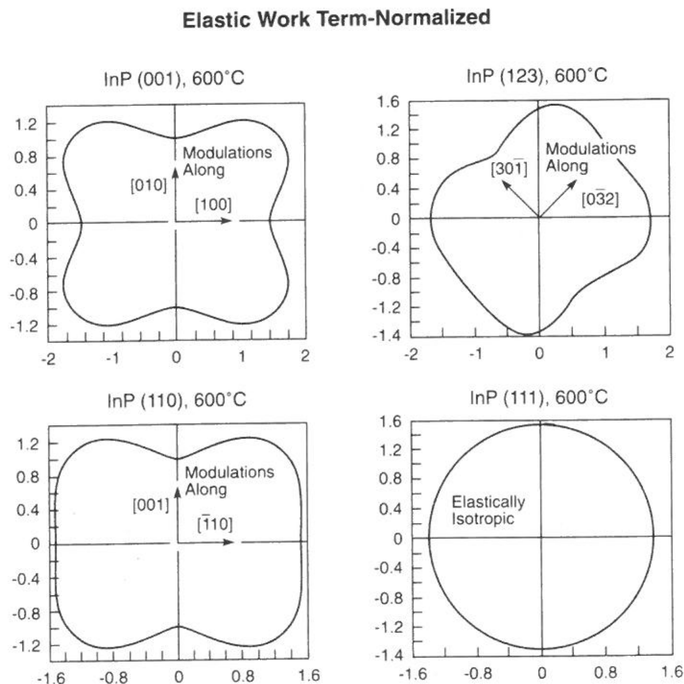

Fig. 17. Polar plots of the relative values of elastic work that is associated with the creation of composition modulations in the plane of the substrate for the (001), (110), (111), and (123) orientations. From McDevitt et al. (1992).

surface while the layer is growing. The fact that *bulk* elastic constants used in these calculations describe *surface* phenomena, is, however, unexpected.

4.3.1.2. Coarse-scale contrast modulations. The origin of coarse modulations seen in fig. 10 is controversial. Henoc et al. (1982), Glas (1989b), Glas et al. (1982), Cherns et al. (1987), Treacy et al. (1985), Launois et al. (1982), and Norman and Booker (1985) suggest that they evolve by phase separation (wavelength of 1000–2000 Å) of a growing layer. Mahajan et al. (1984a, 1989) and McDevitt et al. (1992), on the other hand, have argued that since the observed wavelength is very large (~1000 Å), it cannot evolve by surface diffusion during the time required for the deposition of a monolayer. They suggested that the coarse contrast modulations are an artifact of thin foils, representing wrinkling of the surface, which form to accommodate two-dimensional strains associated with the speckle structure (Mahajan and Shahid 1989, Mahajan et al. 1989, McDevitt 1990, McDevitt et al. 1990, 1992). It is implicit in their suggestion that the coarse modulations are coupled with the fine-scale structure. This issue was recently examined by McDevitt et al. (1991) by measuring the thermal stability of fine and coarse modulations in InGaAsP epitaxial layers. This will be discussed in more detail in § 4.5.

4.3.1.3. Lateral composition modulations at steps. This was seen most clearly in epitaxial growth of AlAs/GaAs on vicinal surfaces of GaAs (001) (Tsuchiya et al. 1989, Lu et al. 1990, Krishnamurthy et al. 1993). A misorientation of 0.5°, 1°, and 2° gives terrace sizes of 320, 160, and 80 Å, respectively. We distinguish here deposition of submonolayers from deposition of a complete monolayer. In the experiment of Tsuchiya et al. (1989) submonolayers of Al and Ga were deposited on this substrate at a low As pressure of 10^{-7}–10^{-8} Torr, until a total cation monolayer was completed. After that, an As monolayer was deposited, while the Al and Ga beam was shut off. This growth mode corresponds to "mobility enhanced" epitaxy. The interesting result is that during Al + Ga deposition, the Al atoms seem to segregate preferentially at the step while the Ga atoms occupy the flat terrace. This segregation is particularly strong if the step is perpendicular to the [100] direction and the growth temperature is 550–600°C. If the step is cut perpendicular to the [$1\bar{1}0$] direction, the Al segregation is poor and the Al–Ga border is not smooth. This elegant experiment shows that the presence of steps introduces a driving force for Al–Ga segregation. This segregation mechanism, reflecting the different chemical affinities of Ga and Al to form bonds at reactive sites (steps), is distinct from surface elastic anisotropy (fig. 17). The atomic arrangement seen in the experiment of Tsuchiya et al. (1989) can be reproduced by *stochastic* kinetic simulations (Lu et al. 1990).

Consider next what happens when one deposits binary compounds AC/BC sequentially ("superlattice growth"). Cyclical deposition of a *fractional* monolayer m of AlAs followed by a fractional monolayer n of GaAs results in *lateral* $(AlAs)_m/(GaAs)_n$ superlattices when $m + n \approx 1$ (Fukui and Saito 1987, Gaines et al. 1988). The lateral period corresponds to the nominal terrace spacing of the vicinal surface. It is believed that these lateral composition modulations are formed when atoms arrive on the surface from the vapor, diffuse along terraces, and attach to the upper step edge.

Under similar growth conditions, one expects that cyclical deposition of alternate *complete* monolayers ($m = n \approx 1$) will result in *vertical* $(AlAs)_1/(GaAs)_1$ superlattices with *no* lateral composition modulation. Recently, however, Krishnamurthy et al. (1993) attempted to grow such superlattices on a 1°–2° misoriented GaAs (001) substrate with Ga terminated steps in the [01$\bar{1}$] direction, finding that *lateral* superlattices were formed. The lateral period was 80 ± 20 Å, in agreement with the nominal substrate misorientation angle. The authors suggested that this structure can be rationalized by assuming that incoming Al atoms always exchange with Ga atoms, where the exchanged Ga atom flows to the step edge. In contrast, an incoming Ga atom does not exchange. In this process, one finds Al-rich regions *away* from the step and Ga-rich regions *near* the step. This is exactly the reverse of what Lu et al. (1990) find in their stochastic kinetic simulation of mobility enhanced epitaxial deposition of Al and Ga on the As face of stepped GaAs (001).

A related form of lateral phase separation is the composition modulation observed by Hsieh et al. (1990) and Cheng et al. (1992) in a "superlattice growth mode". They attempted to grow a (001) $(GaP)_2/(InP)_2$ superlattice on a $Ga_{0.5}In_{0.5}P$ buffer deposited on GaAs by gas-source MBE. Using transmission electron microscopy, transmission electron diffraction, energy-dispersive X-ray microanalysis, and double-crystal X-ray rocking curve measurements, they verified the composition and structure of the (2,2) superlattice and that of the buffer. In addition, they observed an unintentional lateral composition modulation along the [1$\bar{1}$0] direction. Within the modulating bands, which had an about 200 Å periodicity, the In composition was found to vary smoothly from 42 to 56%, while the complementary Ga composition varied between 58 and 44%. The sample is shown schematically in fig. 18, while fig. 19 shows a dark-field image (Cheng et al. 1992). This illustrates phase separation which is induced laterally only when a short-period superlattice exists and when its period deviates from the ideal $n = 2$ value. Recently, this laterally modulated sample was

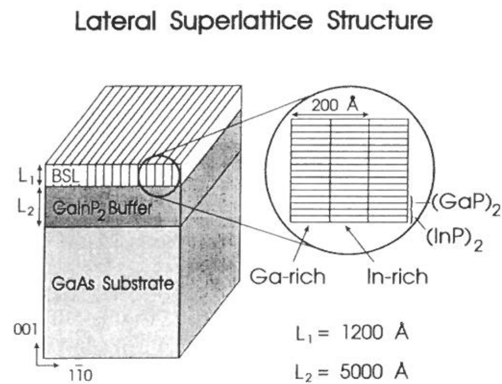

Fig. 18. Schematic of the sample consisting of the $(GaP)_2/(InP)_2$ bilayer superlattice (BSL) and $GaInP_2$ buffer grown on a (001) GaAs substrate. The inset shows the details of the BSL, which is comprised of vertically alternating $(GaP)_2$ and $(InP)_2$ bilayers, superposed on which is the lateral composition modulation that results in Ga-rich and In-rich regions. From Mascarenhas et al. (1992).

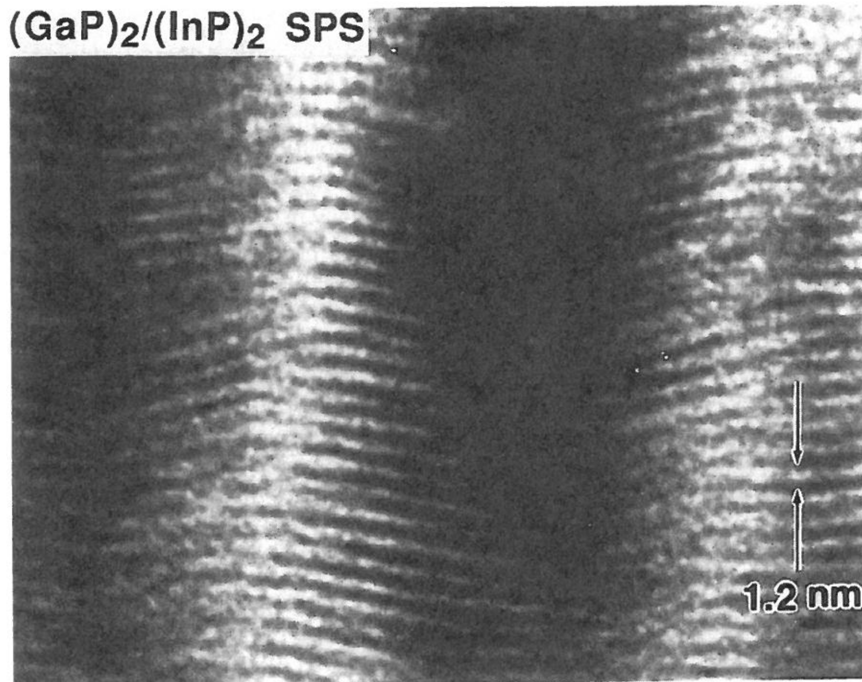

Fig. 19. Dark-field TEM image of the $(GaP)_2/(InP)_2$ (see fig. 18) showing lateral phase separation. From Cheng et al. (1992).

studied by PL, PLE, and reflectance (Mascarenhas et al. 1992); the significant lowering of the band gap (130 meV) relative to the random alloy was interpreted in terms of the lateral composition modulations.

To date phase separation with no atomic ordering has been observed in most layers grown by LPE (Henoc et al. 1982, Launois et al. 1982, Mahajan et al. 1984a, 1989, Ueda et al. 1984, Norman and Booker 1985, Treacy et al. 1985, McDevitt et al. 1992). Depending on the growth conditions, phase separation coexisting with atomic ordering was seen in vapor phase techniques such as VLE, OMVPE, and MBE (Chu et al. 1985, Shahid et al. 1987, Shahid and Mahajan 1988, Ueda et al. 1988, 1989a,b). The issue of ordering is discussed in detail in §§ 5–7.

4.3.2. Phase separation perpendicular to the substrate plane (vertical PS)

Petroff et al. (1982) noted that when $Ga_{0.75}Al_{0.25}As$ was deposited by MBE at 600°C on a GaAs (110) substrate, quasiperiodic composition modulations of wavelength 15–300 Å developed *along the growth direction.* In contrast, deposition on a (100) substrate resulted in a homogeneous film. This is the first example of vertical phase separation in III–V alloys.

Vertical phase separation was recently observed in lattice-mismatched III–V alloys grown on a (001) substrate: Seong et al. (1990), Ferguson et al. (1991, 1992), and

Norman et al. (1993) observed that MBE growth of $InAs_xSb_{1-x}$/(001)GaAs and $GaAs_xSb_{1-x}$/(001)InSb at low temperatures results in strong composition modulations *perpendicular* to the substrate (i.e., along the [001] growth direction). For example, while growth of $InAs_{0.5}Sb_{0.5}$ at 430°C produced rather homogeneous material, growth at 340°C indicates strong composition modulation along [001]. This produces two types of alternating layers along this direction, both having the same lateral lattice parameter of 6.25 Å (i.e., relaxed with respect to the substrate). One layer is essentially $InAs_{0.38}Sb_{0.62}$, having a lattice parameter of 6.4 Å parallel to [001] (i.e., $c/a > 1$), while the second layer is essentially $InAs_{0.80}Sb_{0.20}$ and has a lattice parameter of 6.04 Å (i.e., $c/a < 1$). Increasing the growth temperature from 340 to 370 and 400°C resulted in a progressive increase in the thickness of the phase-separated layers (250, 350, and ~450 Å, respectively). Growth of $InAs_xSb_{1-x}$ for $x = 0.2$ produced no phase separation. Similar vertical phase separation has been observed in $GaAs_xSb_{1-x}$ grown below 500°C (Ferguson et al. 1991). This vertical phase separation is thought (Norman et al. 1993) to occur at the growing surface by the formation of islands of different phases which subsequently laterally overgrow each other. Annealing experiments showed conclusively that the vertical phase separation does not occur by bulk diffusion.

We now summarize the basic findings of this section:

(1) *Observation of lateral phase separation.* This is seen in three growth modes:

(a) homogeneous growth in which all alloy elements are deposited simultaneously leads to a "fine-scale contrast" in the substrate plane with a composition wavelength of about 100 Å, and to a "coarse-scale modulation" with a wavelength of about 1000 Å. The former is seen in various growth methods (LPE, VPE, OMVPE, and MBE) of lattice-mismatched alloys and was interpreted either in terms of coherent bond-length relaxation (Glas and coworkers) or in terms of surface phase-separation during growth (Mahajan and coworkers). The coarse-scale modulation was interpreted either in terms of surface phase-separation (Henoc, Glas, and coworkers) or in terms of an artifact of thin foils wrinkling (Mahajan and coworkers).

(b) Mobility enhanced epitaxy leads to lateral phase separation. This was interpreted by a stochastic kinetic model assuming that *Al* flows to the step edge while *Ga* occupies the terrace.

(c) Superlattice growth in which submonolayers of the *compounds* GaAs and AlAs are deposited sequentially leads to lateral phase separation, with period commensurate with the terrace width. Surprisingly, similar structures occur when *full* monolayers are deposited. This was interpreted in terms of an exchange model assuming that *Ga* flows to the step edge while *Al* occupies the terrace. Lateral phase separation due to superlattice growth occurs also for $(GaP)_2/(InP)_2$. This was interpreted in terms of strain effects rather than preferential attachment to steps versus terraces.

(2) *Observations of vertical phase separation.* This is seen in *low-temperature* MBE growth of homogeneous alloys. For AlGaAs it occurs only on a (110) substrate, whereas for size-mismatched alloys it occurs on a (001) substrate. This was interpreted to occur at the growing surface by the formation of islands of phases with different compositions. These are thought to subsequently overgrow laterally.

The brief summary of the "big picture" concerning lateral and vertical phase

separation in III–V alloys reveals not only how intricate these phenomena are, but also how limited our understanding of these effects is.

4.4. *Effect of growth temperature on lateral phase separation*

If lateral phase separation occurs at the surface while the layer is growing (see § 4.3.1), the evolution of its wavelength and amplitude must occur by surface diffusion. The effect of LPE growth temperature on the occurrence of composition modulation was studied by Henoc et al. (1982), Launois et al. (1982), Glas et al. (1982), and Peiro et al. (1991). Recently, McDevitt et al. (1992) examined the temperature dependence of phase-separated microstructures in (001) InGaAs layers grown by MBE in the temperature range 400–500°C. Consistent with the observations on LPE, VPE, and OMVPE layers discussed earlier, phase separation in this case also occurs along the [100] and [010] direction; the modulation wavelength λ is measured to be 50–60 Å. The authors argued that the period of modulations (λ) may be related to the growth temperature (T) by an activated form:

$$\lambda^2 = A \exp(-E_s/kT), \tag{22}$$

where A is a constant and E_s is the activation energy for surface diffusion. This equation predicts that $\ln(\lambda)$ should vary linearly with $1/T$. McDevitt et al. (1992) deduced from such a plot that E_s is ~ 0.35 eV. Since the activation energy for surface diffusion of As atoms on the (001) GaAs surface is ~ 0.25 eV (Neave et al. 1985) and since the atoms are migrating on an InGaAs surface, it was inferred by the authors that the evolution of phase-separated microstructures in InGaAs layers grown by MBE is controlled by the surface diffusion of As atoms.

4.5. *Thermal stability of phase-separated microstructures*

Since on annealing the reversion of phase-separated microstructures in epitaxial layers can occur only by bulk diffusion, differences must exist in the reversion kinetics of coarse and fine composition modulations. This is inferred because the magnitudes of two-dimensional strains, the source of coarse contrast modulations, should be reduced. This in turn results from interdiffusion among the phase-separated regions. If the fine-scale speckle structure is responsible for the formation of coarse contrast modulations, as discussed in § 4.3.1, the annealing behavior of the two microstructural features should be coupled. If, on the other hand, the two types of modulations develop in a chronological sequence, as suggested by Norman and Booker (1985), the time scales for reversion should be significantly different because of the difference in their wavelengths. McDevitt et al. (1991) have carried out annealing experiments on (001) InGaAsP epitaxial layers grown by LPE. Figure 20 shows a series of dark-field micrographs of as-grown and annealed layers; the layers were annealed for 30 min at a temperature indicated in each figure. The authors drew several conclusions from this figure. First, the fine-scale speckle structure and the coarse modulations are often coupled, suggesting according to these authors that the latter are

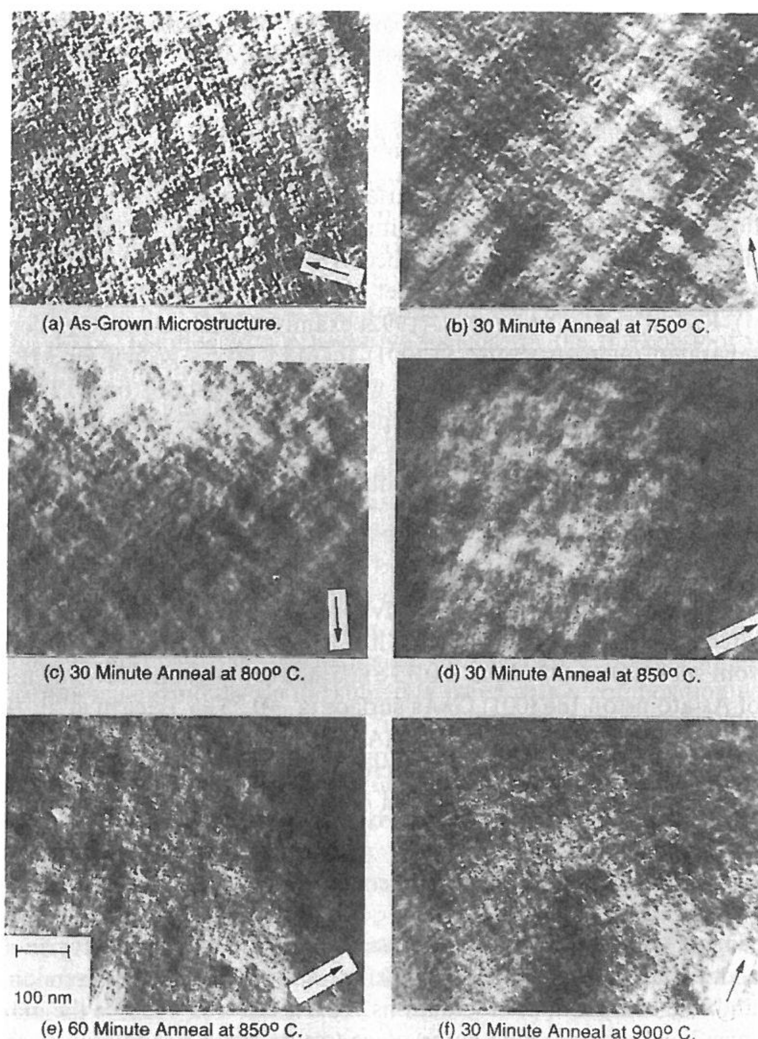

Fig. 20. Series of dark-field micrographs showing the behavior of modulated microstructures during annealing. (a) As-grown microstructure, (b) 30 min anneal at 750°C, (c) 30 min anneal at 800°C, (d) 30 min anneal at 850°C, (e) 60 min anneal at 850°C, (f) 30 min anneal at 900°C. All micrographs were taken with the (220) diffraction condition satisfied and $s = 0$. From McDevitt et al. (1991).

caused by the fine-scale speckle structure. Note, however, that in some cases, e.g., fig. 20f, the coarse modulations are damped despite the fact that the fine contrast remains, so in this case they are not coupled. Second, the time scales required for the reversion of phase-separated microstructure is considerably longer than that required for the deposition of a monolayer. This could suggest that the fine-scale modulations form at the surface while the layer is growing and that the evolution of the speckle structure occurs by surface diffusion of atomic species constituting an

epitaxial layer. Third, the speckle structure is still observed after a half-hour anneal at 900°C.

Two distinct possibilities exist regarding the origin of contrast observed in fig. 20f: either it is due to partial reversion or it results from correlated relaxation of atoms within a layer (Glas et al. 1990). McDevitt (1990) has carried out diffraction contrast experiments to discern these possibilities. His microstructural as well as electron diffraction results appear to support the idea that the contrast in fig. 20f is due to the partial reversion of the phase-separated microstructure.

5. Observations of long-range atomic order in III–V alloys

Before describing the nature of the ordered structures in *isovalent* III–V alloys, consider the "big picture" of ordering in ternary semiconductors. Of course, *nonisovalent* semiconductor components have long been known to form ordered atomic arrangements. This includes the ternary adamantine structures of chalcopyrites $A^{I}B^{III}C_2^{VI}$ (e.g., $CuGaS_2$; see fig. 1), which can be thought of as $(A^{I}C^{VI})_2/(B^{III}C^{VI})_2$ ordered [201] superstructures, or the ternary pnictide $A^{II}B^{IV}C_2^{V}$ (e.g., $ZnSnP_2$) systems having the same structure. In both classes of compounds, below some critical temperature T_c the A and B atoms order crystallographically in the chalcopyrite form, whereas above T_c they disorder into the zinc-blende structure (Zunger 1987, Wei and Zunger 1992). The fact that such *non*isovalent components order is perhaps not too surprising, given the significant electrostatic interactions (Wei and Zunger 1992) between their nonoctet units, e.g., the seven-electron $A^{I}C^{VI}$ "acceptor" with the nine-electron $B^{III}C^{VI}$ "donor" in $A^{I}B^{III}C_2^{VI}$ chalcopyrites. What *is* surprising, is that *octet isovalent units* such as the eight-electron $A^{III}C^{V}$ and $B^{III}C^{V}$ zinc-blende materials will order into an $A^{III}B^{III}C_2^{V}$ compound.

Long-range ordering among isovalent octet units, however, is not new:

(i) It has been known for a long time that, whereas most alkali halide pairs exhibit limited solid solubilities, some pairs involving large differences in the cation radii, produce stoichiometric long-range ordered superstructures. LiF–RbF, for example, orders in the $LiRbF_2$ structure and LiF–CsF orders in the $LiCsF_2$ structure; these ordered "intermetallic" structures were studied crystallographically (Burns and Busing 1965, Burkhalova and Sementsova 1965, Chernov et al. 1976, Chernov and Bugaerko 1976).

(ii) Other examples of ordering among octet systems involve the spontaneous ordering found in Cd_3As_2–Zn_3As_2 alloys: these show the $(Cd_3As_2)_1(Zn_3As_2)_2$ superstructure ("$CdZn_2As_2$") (Trzebiatowski et al. 1963, Masumoto et al. 1971, Berak and Pruchnik 1971), seen also in Cd_3P_2–Zn_3P_2 solid solutions.

(iii) Another interesting ordering system made of octet units is the dolomite $[Ca(CO_3)_2]_x[Mg(CO_3)_2]_{1-x}$ alloy: the *ordered* structure has a measured negative formation energy $\Delta E_f < 0$ (indicating low-temperature ordering), whereas the *disordered* alloy has positive mixing energy $\Delta E_{mix} > 0$ (Navrotski and Capobianco 1987). A related isovalent alloy showing similar features is $[Cd(CO_3)_2]_x[Mg(CO_3)_2]_{1-x}$ (Capobianco et al. 1987).

(iv) Finally, some of the solid solutions of chalcopyrite $A^{I}B^{III}C_2^{VI}$ compounds with the zinc-blende $D^{II}C^{VI}$ semiconductors show signs of formation of an intermediate ordered stannite-like phase (Osorio et al. 1993, Quintero et al. 1990, Newman and Xiang 1991, Gallardo and Lin 1992, Gallardo 1992).

In all of these cases, size-mismatched octet units combine to give ordered superstructures. The discussion in § 2 is pertinent here: the large size-mismatched-induced volume-deformation energy ΔE_{VD} is overcome in these cases by the stabilizing chemical interactions of charge-transfer ΔE_{CT} and sublattice relaxation ΔE_{REL}. Note also that *magnetic* ordering is seen in zinc-blende compounds, e.g., the spins in MnTe order in the chalcopyrite arrangement $Mn^{\uparrow}Mn^{\downarrow}Te_2$ (see Furdyna 1988).

In the remainder of this chapter we will discuss the particular case of ordering among III–V semiconductor components.

As shown by Srivastava et al. (1985), Wei et al. (1990), and Bernard et al. (1991), a variety of ordered structures are possible in alloys of zinc-blende semiconductors (fig. 1). These can be described as $(AC)_p(BC)_q$ superlattices whose layers are oriented along direction $\hat{G}$. The most important cases are (i) the CuAu–I (or "CA") ordering, which is a monolayer ($p = q = 1$) superlattice along $\langle 001 \rangle$, (ii) the chalcopyrite (or CH) ordering, which is a bilayer ($p = q = 2$) superlattice along $\langle 201 \rangle$, and (iii) the CuPt-like (or CP) ordering, which is a monolayer superlattice along $\langle 111 \rangle$. In discussing the crystallography of the observed structures, it is assumed that the origins of group III and V sublattices are at $[0, 0, 0]$ and $[\frac{1}{4}, \frac{1}{4}, \frac{1}{4}]$, respectively, see fig. 1.

The *classic* thermodynamic theories of semiconductor alloys reviewed in §§ 1 and 2 portrayed the excess energies ΔE of eqs. (1) and (2) as being *configuration independent*. For example, the regular-solution approach (Panish and Ilegems 1972, Stringfellow 1974, Foster 1976, Chiang and Johnson 1989) assumed $\Delta E = \Omega x(1 - x)$. The "delta lattice parameter" (DLP) model (Stringfellow 1974) interpreted Ω in terms of the relative A–B size mismatch. The common theme of these approaches was that ΔE does not depend on the configuration (e.g., ordered versus disordered) but rather on the global properties (e.g., compositions, molar volumes). Since ΔE_{mix} (eq. (2)) was known at the time to be positive, it was naturally assumed that this instability of the disordered alloy ($\Omega > 0$) towards phase separation is also shared by its possible ordered modifications. Hence, long-range order was not expected.

Concomitant with the first theoretical prediction (Srivastava et al. 1985) that despite $\Delta E_{mix} > 0$ semiconductor alloys could exhibit LRO, Kuan et al. (1985) observed LRO in $Al_{1-x}Ga_xAs$ (ironically, this first published case of ordering in III–V alloys is still not understood). Using selected-area electron diffraction, they have examined $Ga_{1-x}Al_xAs$ layers grown by OMVPE and MBE on GaAs substrates; the value of x was varied between 0.25 and 0.75, growth temperatures were in the range of 600 to 800°C, and (110) and (100) substrates were used. Superstructure reflections were observed in (110) and (001) patterns. These results are reproduced in fig. 21 for $Ga_{0.75}Al_{0.25}As$ film grown on a (110) GaAs substrate by OMVPE at 700°C. It is evident that, besides the fundamental spots belonging to the zinc-blende structure, extra reflections are present at (110), (001), and other equivalent positions, as seen in fig. 21a. The (001) pattern from the same layer, reproduced in fig. 21b,

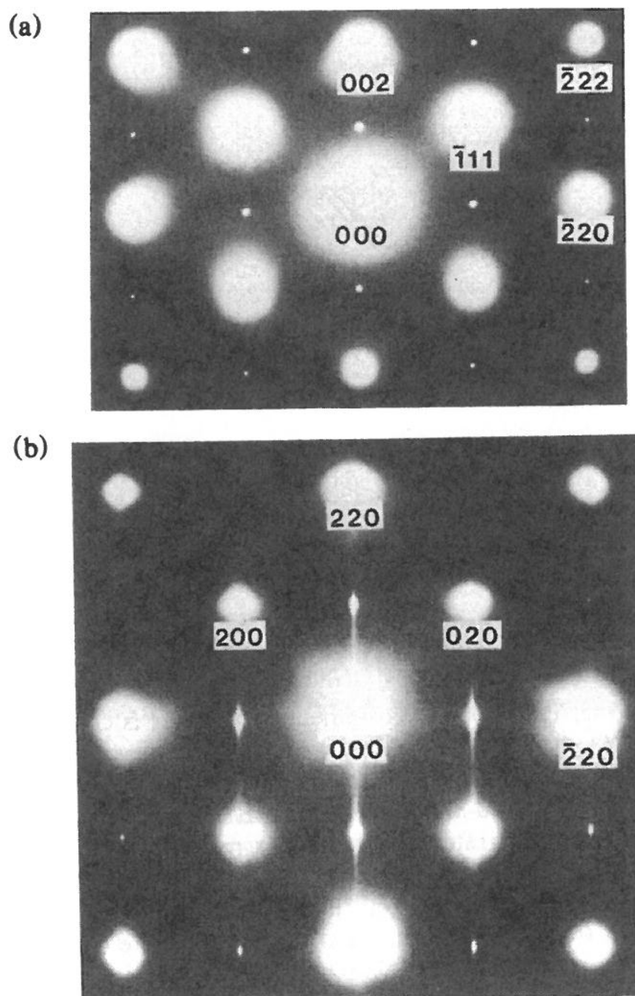

Fig. 21. (a) (110) diffraction pattern and (b) (001) pattern from an $Al_{0.75}Ga_{0.25}As$ film grown on a (110) GaAs substrate by MOCVD at 700°C. From Kuan et al. (1985).

shows superlattice reflections at (110), ($1\bar{1}0$), and equivalent positions. Kuan et al. (1985) showed that the above observations are consistent with the presence of CA ordering (see fig. 1) in $Ga_{1-x}Al_xAs$ layers grown by OMVPE or MBE on (110) substrates. In addition, all the reflections are streaked in the growth direction; the origin of these streaks is not understood. The results of their study are summarized in table 2. Note that significant CA ordering at $x = 0.5$ is seen only on a (110)-oriented substrate; on a (001) substrate only weak CA ordering was present for the *nonequimolar* ($x = 0.75$) alloy. This type of ordering is qualitatively similar to the vertical phase separation noted by Petroff et al. (1982) for $Ga_{0.75}Al_{0.25}As$/GaAs (110) (see § 4.3.2).

Table 2
Intensities of superstructure reflections observed from $Al_xGa_{1-x}As$ thin crystals grown on GaAs by MOCVD. From Kuan et al. (1985).

Substrate orientation	Al content (x)	600°C	Growth temperature		
			650°C	700°C	800°C
(110)	0.25	–	weak	–	–
	0.50	weak	weak	medium	weak
	0.75	weak	medium	strong	weak
(100)	0.25	–	–	weak	–
	0.50	–	–	–	–
	0.75	–	–	–	weak

Nakayama and Fujita (1986) reported the presence of a famatinite-type ordered structure (fig. 1) in $In_{0.53}Ga_{0.47}As$ layers grown on (001) InP substrates by LPE (the famatinite structure is identical to the $A_2B_2C_4$ chalcopyrite structure, when one of the A atoms is changed into B). The assignment of Nakayama and Fujita was based on examination of a single reciprocal section of the ordered structure.

Kuan et al. (1987) report the existence of a CA-type structure in $In_{0.5}Ga_{0.5}As$ epitaxial layers deposited by MBE on (110) InP substrates; the growth temperature was 530°C, whereas the growth rate was 0.2 μm/h. It hence appears from the results of Kuan et al. (1985, 1987) that a (110)-oriented substrate is conducive to CA-type ordering in $AlGaAs_2$ and $InGaAs_2$. Most workers have focused, however, on (001)-oriented substrates, which produce a different type of ordering.

Jen et al. (1986) examined the (001) reciprocal sections of $GaAs_{0.5}Sb_{0.5}$ layers deposited on (001) InP substrates by OMVPE. A representative electron diffraction pattern obtained from their later work (Jen et al. 1987) is reproduced as fig. 22, and a summary of the results of their detailed study is given in table 3. Two types of ordered structures, CuAu-I (CA) and chalcopyrite (CH), were observed in Ga_2AsSb layers. The intensities of reflections belonging to a particular ordered structure were found to be affected by the growth rate, growth temperature, and orientation of the underlying substrate.

Figure 23 shows the results of Gomyo et al. (1988a) on $Ga_{0.5}In_{0.5}P$. It is evident that extra diffraction spots are observed at $(\frac{\bar{1}}{2}, \frac{1}{2}, \frac{1}{2})$ and $(\frac{1}{2}, \frac{\bar{1}}{2}, \frac{1}{2})$ and other equivalent positions. This observation implies that in the ordered structure the real-space periodicities along the $[\bar{1}11]$ and $[1\bar{1}1]$ direction are doubled. Also, when the $(1\bar{1}0)$ reciprocal section was examined, extra diffraction spots were not observed, implying that ordering occurs only on two of the four possible $\{111\}$ planes. Since the line of intersection of the $\{111\}$ planes on which ordering occurs with the (001) surface is parallel to the intersection of the $\{111\}_B$ planes with the (001) plane, the observed ordered variant is termed as $CuPt_B$ (or CP_B) (each of the two components of CP_B will be termed "subvariant"). Gomyo et al. (1988a) also found that the relative proportion of the two CP_B subvariants $[\bar{1}11]$ and $[1\bar{1}1]$ depends on the (001) substrate misorientation: the population of a particular subvariant is enhanced when

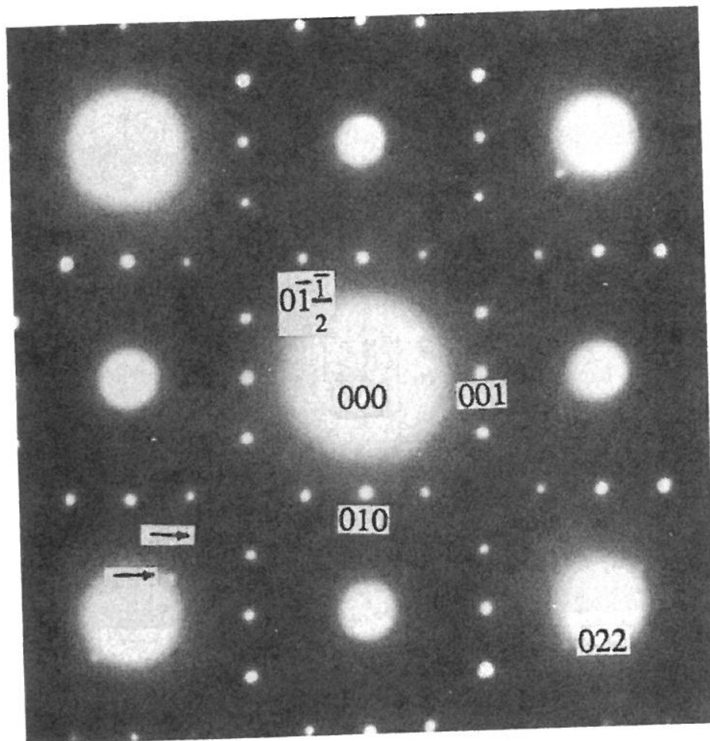

Fig. 22. The [100] pole electron diffraction pattern of $GaAs_{0.5}Sb_{0.5}$ grown on a (100) InP substrate at 600°C with a growth rate of 0.09 μm/min. The forbidden spots {100} are CA induced, and the $\{1\frac{1}{2}0\}$ spots are CH induced. Arrows show the superlattice spots of the three times normal periodicity along the [110] direction. After Jen et al. (1987).

the substrate has a vicinal angle component inclined towards $[\bar{1}11]$ and $[1\bar{1}1]$, respectively. Thus, [110] steps descending towards $[\bar{1}10]$ ("B steps") could control the ratio between CP_B subvariants. Figure 23 shows indeed an enhancement of the $[\bar{1}11]$ subvariant with respect to the $[1\bar{1}1]$ subvariant for a (001) substrate misoriented by 2° towards [010], which has a 1° misorientation component towards $[\bar{1}11]$. The two A subvariants (CP_A) are never seen in OMVPE growth. The atomic arrangement within an $Ga_{0.5}In_{0.5}P$ layer which has undergone $CuPt_B$ ordering along the $[\bar{1}11]$ direction is shown in fig. 24. Geometrically, this arrangement can be realized by positioning alternate [110] rows of Ga and In atoms along the $[1\bar{1}0]$ direction and by shifting the rows by $a/(2\sqrt{2})$ in interlayers.

Since the pioneering work of Kuan et al. (1985), Nakayama and Fujita (1986), Jen et al. (1986), Murgatroyd et al. (1986), Ueda et al. (1987), Shahid et al. (1987), and Gomyo et al. (1988a), many investigators have reported the occurrence of ordering in a variety of ternary zinc-blende alloys. Table 4 summarizes these observations. The following assessments can be made from this table:

(i) The CuPt-type ordering is by far the most commonly observed structure in

Table 3
Dependence of ordering in Ga_2AsSb on growth parameters, s = strong, m = moderate, w = weak, vw = very weak. From Jen et al. (1987).

Growth temperature (°C)	Substrate orientation							
	(100)		(110)		(221)		(311)	
	Growth rate (μm/min)	Ordering observed	Growth rate (μm/min)	Ordering observed	Growth rate (μm/min)	Ordering observed	Growth rate (μm/min)	Ordering observed
550	0.02	CA(m)	0.02	CA(m)	0.06	CA(vw)	0.06	CA(vw)
	0.01	CA(m), CH(w)	0.01	CA(m)				
600	0.09	CA(s), CH(s)	0.09	CA(m)				
	0.045	Ca(s), CH(s)	0.045	CA(m)				
650	0.22	Ca(s), CH(s)						

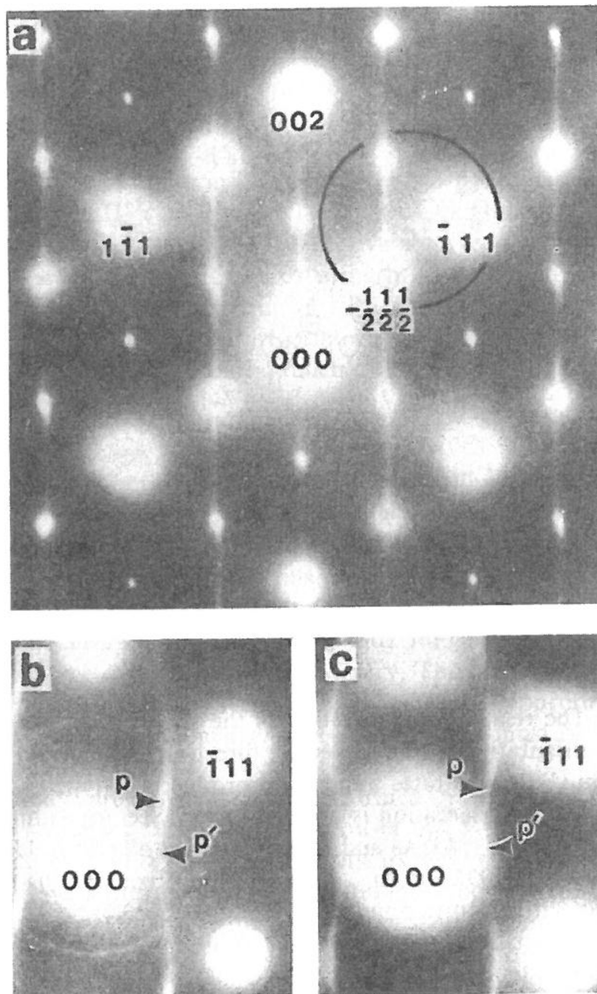

Fig. 23. The [110]* zone-axis electron-diffraction patterns for three growth temperatures. (a) A TED pattern from a $Ga_{0.5}In_{0.5}P$ crystal showing strong superstructure spots $(-\frac{1}{2}, \frac{1}{2}, \frac{1}{2})$ along the $[\bar{1}11]^*$ direction but weak spots with $[\bar{1}11]^*$. The crystal was grown at $I_s = 700°C$. (b) A TED pattern for a sample grown at $T_s = 600°C$. (c) A TED pattern for a sample grown at $T_s = 550°C$. The about 10° inclination to the $\pm[110]^*$ directions at the $(-\frac{1}{2}, \frac{1}{2}, \frac{1}{2})$ and $(-\frac{1}{2}, \frac{2}{2}, \frac{3}{2})$ positions and wavy features of the streaks are clearly observed in (b) and (c). The points p and p′, indicated by arrows, show the positions of $(-\frac{1}{2}, \frac{1}{2}, \frac{1}{2})$ and $(-(\frac{1}{2} - \delta), \frac{1}{2} - \delta, 0)$, respectively. From Gomyo et al. (1988a).

(001) epitaxial layers. It evolves under a variety of growth methods, growth conditions, and substrates. It seems that ordering is the *rule*, rather than an exception, in vapor phase growth of III–V alloys.

(ii) Out of the four possible variants, only the $CuPt_B$ variant (with two "degenerate" *sub*variants, $(\bar{1}11)$ and $(1\bar{1}1)$) is observed. This is the case both for mixed-anion and for mixed-cation alloys. For example, both $GaInP_2$ and Ga_2AsSb alloys exhibit

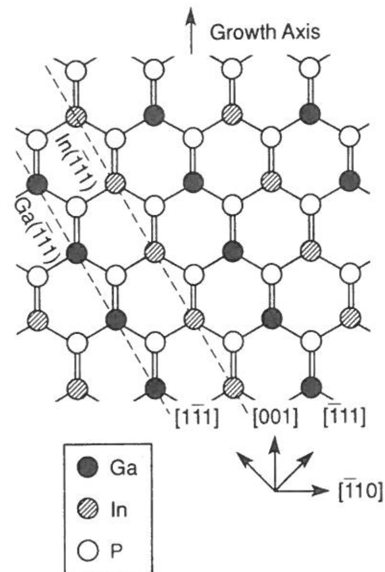

Fig. 24. Schematic of the atomic arrangement within an $In_{0.5}Ga_{0.5}P$ layer that has ordered on the (1$\bar{1}$1) planes.

$CuPt_B$ ordering. The relative concentration of the two subvariants is controlled by the substrate misorientation in the respective direction of the subvariant.

(iii) Growth on (110) substrates appears to produce CA-type ordering (although the role of substrate misorientation is not clear here). See, for example, the work of Kuan et al. (1985) on $Ga_{1-x}Al_xAs$ and that of Kuan et al. (1987), Ueda et al. (1991), and Ueda and Nakata (1992) on $In_{1-x}Ga_xAs$ alloys. Exact (110) substrates do not appear to produce any CP ordering (Gomyo et al. 1988b).

(iv) The OMVPE-grown Ga_2AsSb alloys exhibit CP, CA, and CH ordering, depending on growth temperatures and rates (table 3), whereas MBE growth of the same alloys shows CP-type ordering. One might think that non-CuPt diffraction spots could also arise from the presence of different types of interfaces between the two CuPt-type subvariants. It could be, for instance, that the extra spots observed in fig. 22 (Jen et al. 1986, 1987) are due to such interfaces. However, a private communication by G.B. Stringfellow (1993) indicates that no $\langle 111 \rangle$ superlattice spots were found in these samples in any of the $\{110\}$ cross sections, so only CuAu and chalcopyrite ordering appears to be present.

(v) With the exception of a single observation by Nakayama and Fujita (1986), epitaxial layers grown by LPE do not exhibit atomic ordering and show only phase-separated microstructures. Further LPE studies of ordering are clearly needed.

(vi) Atomic ordering and phase separation seem to coexist in layers grown by vapor phase techniques. Shahid et al. (1987) and Shahid and Mahajan (1988) have demonstrated that CuPt-type order and phase separation are observed in (001) InGaAs and InGaAsP epitaxial layers grown by chloride transport VPE.

Subsequently, Ueda et al. (1988), Mahajan et al. (1989), and McDevitt et al. (1990) showed that an identical situation exists in (001) GaInP and in GaAlInP layers deposited by OMVPE. The recent studies of Ueda et al. (1989a) and Philips et al. (1993) on (001) InAlAs and InGaAs epitaxial layers, grown by MBE, indicate the coexistence of atomic ordering and phase separation.

While the search for ordering in III–V alloys has been an active area of research since 1985, ordering in II–VI alloys has hardly been examined. Very recently, Park et al. (1992) and Salamanca-Riba et al. (1992) have observed for the first time ordering in a II–VI like system: they noted CA ordering in MBE-grown $Zn_{0.5}Fe_{0.5}Se$. Also, a single report exists of CuPt ordering in LPE-grown HgCdTe on a $(111)_B$ CdTe substrate (Chang and Goo 1992). Furthermore, Bode (1993) observed CP ordering in off-stoichiometric $CuInSe_2$. Clearly, much more work is needed to establish the generic patterns of ordering in II–VI and I–III–VI_2 systems.

6. Influence of growth parameters on ordering in III–V alloys

The experimental evidence to date indicates that growth parameters such as growth temperature, rate, V/III ratio, surface misorientation, and the presence of dopants during growth, have a considerable effect on the *degree of atomic ordering* as measured by TED. While ordering exists for a very wide range of values of any of these parameters, the *degree* of ordering seems to vary. These results are reviewed next. However, before discussing these effects, a word of caution is appropriate. To establish how growth parameters affect the *degree* of ordering, one must be able to quantitatively measure the latter quantity. Unambiguous measures of the degree of ordering (i.e., order parameter) are conventionally performed in metallurgy by Bragg as well as diffuse X-ray scattering. With the exception of the X-ray studies of Kurtz et al. (1989) and Okuda et al. (1989) such measurements were not performed on thin-film semiconductor alloys. Instead, one uses the (nonkinematic) electron diffraction which does not, by itself, gives accurate quantitative measures of the degree of ordering. For example, Kondow et al. (1988c) associated ordering with the *sharpness* of the TED spots, concluding that it is maximum for GaInP near 700°C, whereas Gomyo et al. (1988a) associated ordering with the *intensity* at the $\frac{1}{2}(\bar{1}11)$ and $\frac{1}{2}(1\bar{1}1)$ positions, finding that it is maximum at about 650°C. The results of Suzuki et al. (1988b) appear to disprove those of Kondow et al. (1988c). Note, however, that in a nonkinematic scattering process the intensity is a complex function of film thickness, electron beam conditions, etc., so the intensity cannot simply be used as a direct measure of the degree of order (Baxter et al. 1990, 1991). Furthermore, currently available ordered samples exhibit a "mosaic" structure with domains having different degrees of long-range order. This further complicates the analysis of the TED and TEM data. Finally, the reduction in band gap upon ordering (see § 8.3) was also used extensively in the literature to assess the degree of order. However, as will be seen in § 8.3, while ordering certainly reduces the band gap, so does local phase-separation (clustering) and tensile strain. While theoretical calculations have separated these effects (e.g., Wei and Zunger 1993, Wei et al. 1993), *quantitative experimental* measures of the degree of ordering in these materials are urgently needed.

Table 4
Summary of experimental results on atomic ordering. $\Theta/[hkl]$ means substrate misorientation towards $[hkl]$.

Layer composition	Substrate and its orientation	Growth technique	Growth temperature (°C)	Type of ordered structure	Ref.[a]
$Ga_{1-x}Al_xAs$ $x=0.25\rightarrow 0.875$	(110)GaAs (001)GaAs	OMVPE and MBE	600–800	CuAu-I No order at $x=\frac{1}{2}$	[1]
$GaAs_{0.5}Sb_{0.5}$	(001)InP $\Theta=3°/[110]$	OMVPE	550–680	CuAu-I + CH	[2]
$GaAs_{1-y}Sb_y$ $y=0.25$, 0.5, and 0.71	(001)GaAs $\Theta=2°/[110]$	MBE	520	Chalcopyrite CuPt-type	[3]
GaAsSb	~(001)GaAs $\Theta=3°/[110]$	OMVPE	550–680	CuAu-I + chalcopyrite	[4]
GaAsSb	(001)GaAs and InP	MBE	480–580	CuPt-type	[5]
$GaAs_{0.5}Sb_{0.5}$	(001)GaAs	MBE	480, 520, and 580	CuPt-type	[6]
$GaAs_{1-y}Sb_y$ $y=0.25$, 0.5, and 0.71	(001)GaAs $\Theta=2°/[110]$	MBE	520	CuPt-type	[7]
$In_{1-x}Ga_xAs$ $x=0.475$	~(001)InP	LPE	630	famatinite	[8]
$In_{0.53}Ga_{0.47}As$	~(001)InP	VLE	650 and 660	CuPt-type	[9]
$In_{0.53}Ga_{0.47}As$	~(001)InP	OMVPE	600 to 700	CuPt-type	[10]
$In_{0.5}Ga_{0.5}As$	~(110)InP	MBE	530	CuAu-I type	[11]
$In_{1-x}Ga_xAs_yP_{1-y}$	~(001)InP	VLE	650 and 660	CuPt-type	[12]
InGaAsP	~(001)	OMVPE	600 to 700	CuPt-type	[10]
$In_{1-x}Ga_xAs_yP_{1-y}$ $x=0.75$ and $y=0.45$	~(001)GaAs	OMVPE	640	CuPt-type	[13]
$Ga_{0.47}In_{0.53}As$	~(110) $\Theta=6°$ towards $(11\bar{1})$ and (111) poles	MBE	470	CuAu-I type	[14]
$In_{0.5}Ga_{0.5}As$	~(110)InP	MBE	405	CuAu-I type	[15]
$In_{0.5}Ga_{0.5}As$	~(110)InP $\Theta=5°/[001]$	MBE	360–450	CuAu-I type	[16]
$Ga_{0.5}In_{0.5}P$	(001)GaAs $\Theta=2.5°/[110]$	OMVPE	600–630	CuPt-type	[17]
$Ga_{0.5}In_{0.5}P$	~(001)GaAs $\Theta=2°/[110]$	OMPVE	~700	CuPt-type	[18]

$Ga_{0.5}In_{0.5}P$	~(001)GaAs	OMVPE	625 and 700	CuPt-type	[19]
$Ga_{0.5}In_{0.5}P$	~(001)GaAs $\Theta = 2°/[110]$	OMPVE	650	CuPt-type	[20]
$Ga_{0.5}In_{0.5}P$	~(001)GaAs 2°/[110]	OMVPE	650–670	CuPt-type	[21]
$Ga_{0.5}In_{0.5}P$	~(001)GaAs $\Theta = 2°/[110]$	OMPVE	550–700	CuPt-type	[22]
$Ga_{0.58}In_{0.42}P$	~(001)GaAs $\Theta = 6°$/around ⟨110⟩ toward $\{111\}_A$ and $\{\bar{1}\bar{1}\bar{1}\}_B$	OMVPE	640	CuPt-type	[23]
$Ga_{0.5}In_{0.5}P$	~(001)GaAs	OMPVE	600–700	CuPt-type	[24]
$Ga_{0.5}In_{0.5}P$	~(001)GaAs	OMPVE	–	CuPt-type	[25]
$Ga_{0.5}In_{0.5}P$	(001)GaAs	OMVPE	660–700	CuPt-type	[26]
$Ga_{0.5}In_{0.5}P$	~(001)GaAs	OMVPE	650 and 700	CuPt-type	[27]
InGaP	~(001) $\Theta = 2.5°/[110]$	OMVPE	630	CuPt-type	[28]
$Ga_xIn_{1-x}P$ $x = 0.52$	~(001)GaAs $\Theta = 6°$ around ⟨110⟩ toward $\{111\}_A$ and $\{\bar{1}\bar{1}\bar{1}\}_B$	OMVPE	650	CuPt-type	[29]
$Ga_{0.5}In_{0.5}P$	~(001)GaAs Different misorientations	OMVPE	~650 and 700	CuPt-type	[30]
$Ga_xIn_{1-x}P$ $x = 0.52$	(001)GaAs $\Theta = 6°$ around ⟨110⟩ toward $\{111\}_A$ and $\{\bar{1}\bar{1}\bar{1}\}_B$	OMVPE	650	Both CuPt variants for $\{111\}_A$ and $\{\bar{1}\bar{1}\bar{1}\}_B$ tilt. Biases one variant	[31]
$Ga_{0.7}In_{0.3}P$	(001)GaAs	OMVPE	690	CuPt-type	[32]
$Ga_{0.52}In_{0.48}P$	~(001)GaAs $\Theta = 2°/[110]$	OMVPE	–	CuPt-type	[33]
$Ga_{0.52}In_{0.48}P$	~(001)GaAs	OMVPE	700 and 750	CuPt-type	[34]
$Ga_{0.5}In_{0.5}P$	~(001)GaAs	OMVPE	600–700	CuPt-type	[32]
$Ga_{0.5}In_{0.5}P$	~(001)GaAs	OMVPE	600–750	CuPt-type	[35]
$Ga_{0.5}In_{0.5}P$	~(001)GaAs	OMVPE	590–650	CuPt-type	[36]
$Ga_{0.5}In_{0.5}P$	(001)GaAs $\Theta = 2.5°/\langle 010\rangle$	chloride-VPE	576–740	CuPt-type	[37]
$Ga_{0.51}In_{0.49}P$	~(001)GaAs oriented 2–3° off (001) toward [110]	OMVPE	680	CuPt-type	[38]

Table 4 (*continued*)

Layer composition	Substrate and its orientation	Growth technique	Growth temperature (°C)	Type of ordered structure	Ref.[a]
$Ga_{0.5}In_{0.5}P$	Patterned (001) GaAs substrates	OMVPE	670	CuPt-type	[39]
$Ga_{0.5}In_{0.5}P$	~(001)GaAs $\Theta = 0.5$ and 2°/[110]	OMPVE involving ALE	480–550	CuPt-type	[40]
$Ga_{0.52}In_{0.48}P$	~(001)GaAs	OMVPE	600–725	CuPt	[41]
$Ga_{0.5}In_{0.5}P$	~(001)GaAs	OMVPE	600 and 750	CuPt-type	[42]
$Ga_{0.5}In_{0.5}P$	~(001)GaAs	OMVPE	650–750	CuPt-type	[43]
$Ga_{0.5}In_{0.5}P$	~(001)GaAs	OMVPE	660	CuPt-type	[44]
$Al_{0.5}Ga_{0.5}P$	~(001)GaP	Evaporation of Al on GaP followed by high-energy electron irradiation	$(1-5) \times 10^{17}$ electrons/cm^2 at 7 MeV and 50°C	CuAu-I type	[45]
$(Al, Ga)_{0.5}In_{0.5}P$	~(001)GaAs	OMVPE	650 to 670	CuPt-type	[21]
$(Al_xGa_{1-x})_{0.5}In_{0.5}P$ $0 \leqslant x \leqslant 1$	(001)GaAs	OMVPE	700	CuPt-type	[25]
$(Al_xGa_{1-x})_{0.5}In_{0.5}P$ $0 \leqslant x \leqslant 1$	(001)GaAs	OMVPE	570–770	CuPt-type	[46]
$(Al_xGa_{1-x})_{0.5}In_{0.5}P$	~(001) 2°/[110]	OMVPE	550–750	CuPt-type	[27]
$(Al_xGa_{1-x})_{0.5}In_{0.5}P$	misoriented (001)GaAs substrates	OMVPE	650–675	CuPt-type	[47, 48]
$Al_{0.5}In_{0.5}P$	(001)GaAs	OMVPE	610–740	CuPt-type	[49]
$GaAs_{0.7}P_{0.3}$	~(001)GaAs	OMVPE	680	CuPt-type	[50]
$GaAs_{0.5}P_{0.5}$	~(001)GaAs $\Theta = 6°$ around ⟨110⟩ toward$\{111\}_A$ and $\{\bar{1}\bar{1}\bar{1}\}_B$	OMVPE	670	CuPt-type	[51]
$GaAs_{0.5}P_{0.5}$	Exact (001)GaAs ~(001)GaAs $\Theta = 6°$/[110] ~(001)GaAs $\Theta = 6°$/[1$\bar{1}$0]	OMVPE	670	CuPt-type	[52]

$GaAs_{1-x}P_x$ $x = 0.25$ to 0.85	Exact (001)GaAs ~(001)GaAs $\Theta = 6°/[110]$ ~(001)GaAs $\Theta = 6°/[1\bar{1}0]$	OMVPE	670	No ordering for $x \leqslant 0.35$. CuPt type for $0.4 \leqslant x \leqslant 0.85$	[52]
$GaAs_{1-x}P_x$ $x = 0.55$	~(001)GaAs	OMVPE	640	CuPt-type	[13]
AlInAs	~(001)InP	MBE	–	CuPt-type	[53]
$In_{1-x}Al_xAs$ $x = 0.48$	~(001)InP	MBE	560	CuPt-type	[54]
$InAs_{1-x}Sb_x$ $x = 0.22$ to 0.88	(001)InAs or InSb	OMVPE	375 to 480	CuPt-type intense superlattice spots observed for $x = 0.5$	[50]
$InP_{1-x}Sb_x$	–	OMVPE	–	CuPt-type	[55]
$Al_{0.5}In_{0.5}P$	~(001)GaAs	OMVPE	610–740	CuPt-type	[32]

[a] [1] Kuan et al. (1985), [2] Jen et al. (1986), [3] Murgatroyd et al. (1986), [4] Jen et al. (1987), [5] Ihm et al. (1987), [6] Otsuka et al. (1989), [7] Murgatroyd et al. (1990), [8] Nakayama and Fujita (1986), [9] Shahid et al. (1987), [10] Chu et al. (1992), [11] Kuan et al. (1987), [12] Shahid and Mahajan (1988), [13] Plano et al. (1988), [14] A. Chin et al. (1991), [15] Ueda et al. (1991), [16] Ueda et al. (1992), [17] Ueda et al. (1987), [18] Gomyo et al. (1987), [19] McKernan et al. (1988), [20] Dabkowski et al. (1988), [21] Gavrilovic et al. (1988), [22] Gomyo et al. (1988a,b), [23] Bellon et al. (1988), [24] Nishino et al. (1988), [25] Kondow et al. (1988a,b,c), [26] Morita et al. (1988), [27] Suzuki et al. (1988a,b,c), [28] Ueda et al. (1988), [29] Augarde et al. (1989), [30] Suzuki et al. (1989), [31] Bellon et al. (1989), [32] Kondow et al. (1989a,b), [33] Kurtz et al. (1989), [34] Mascarenhas et al. (1989), [35] Kurtz et al. (1990a,b), [36] Okuda et al. (1989), [37] Ueda et al. (1990), [38] Cao et al. (1991), [39] Chen and Stringfellow (1991), [40] McDermot et al. (1991), [41] DeLong et al. (1990), [42] Freedman et al. (1991), [43] Lee et al. (1991), [44] Suzuki and Gomyo (1991), [45] Wada and Maeda (1988), [46] Nozaki et al. (1988), [47] Mahajan et al. (1989), [48] Mahajan and Shahid (1989), [49] Kondow et al. (1989b), [50] Jen et al. (1989a,b), [51] Chen et al. (1990), [52] Chen et al. (1991), [53] Norman et al. (1987), [54] Ueda et al. (1989a), [55] Referred to in [50].

6.1. *Effects of growth temperature*

A number of investigators have evaluated the influence of growth temperature on the CP_B ordering (Gomyo et al. 1988a, Morita et al. 1988, Kondow et al. 1988a,b, Suzuki et al. 1988b, Nozaki et al. 1988, Kurtz et al. 1989). For a fixed V/III ratio and substrate misorientation, ordering is maximal for a growth temperature interval, whereas it is poor at lower and higher growth temperature. In certain cases, it may even be absent at high temperatures. For example, Gomyo et al. (1988a) observe that GaInP layers grown by OMVPE are maximally ordered at a growth temperature of 650°C, slightly less ordered at 600°C, and almost disordered at 700°C. Similar results have been reported in other studies. Morita et al. (1988) have examined GaInP epitaxial layers grown by OMVPE in the temperature range of 660–700°C. The observed diffraction patterns are reproduced as figs. 25a–c, whereas figs. 25d–g show dark-field images of the ordered layers. The diffuse intensity spikes are more pronounced in fig. 25a ($T_g = 660$°C) than those in fig. 25c ($T_g = 700$°C). The dark-field images indicate that the order is less perfect at 660°C, i.e., there are a large number of interfaces between the two CuPt-type variants, compare fig. 25d ($T_g =$ 660°C) with figs. 25f ($T_g = 680$°C) and 25g ($T_g = 700$°C). Morita et al. (1988) have

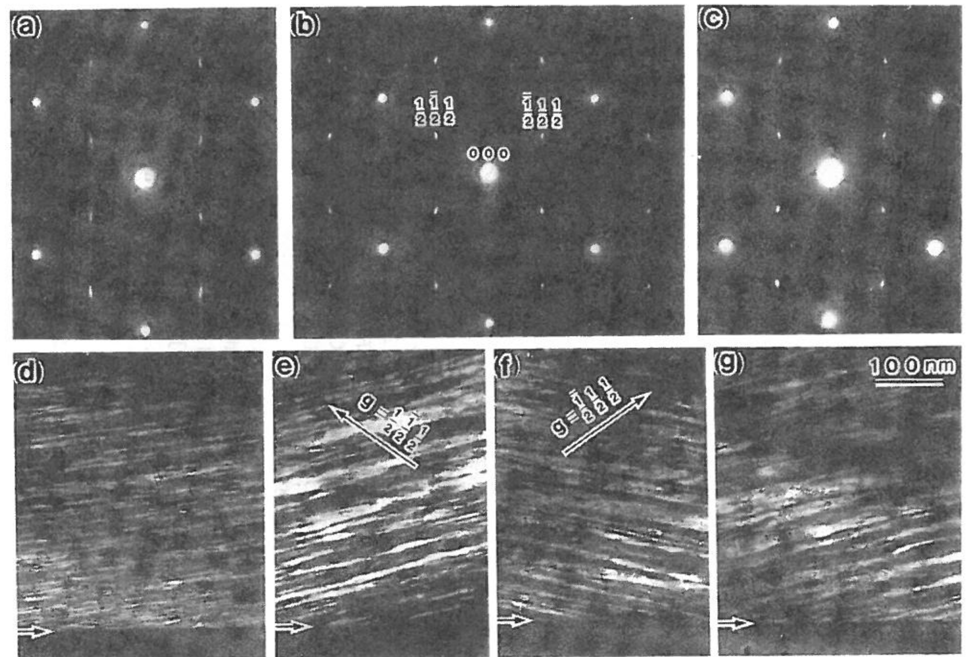

Fig. 25. (a), (b), and (c) Electron diffraction patterns and (d), (e), (f), and (g) dark-field electron micrographs of undoped GaIn/GaAs grown at 660, 680, and 700°C, respectively, taken with (d), (e), and (g) the superlattice reflections of (1, $\bar{1}$, 1) and (f) ($\bar{1}$, 1, 1). The plate-like domains in (e) and (f), which are the same area, are perpendicular to the inclined spikes of the reflections (1, $\bar{1}$, 1) and ($\bar{1}$, 1, 1), respectively. The short arrows indicate the epi/sub-interfaces. From Morita et al. (1988).

examined these layers by high-resolution electron microscopy, and an image obtained from a layer grown at 680°C is shown in fig. 26. The enhanced image of a high-resolution micrograph, fig. 26b, clearly delineates the frequency of switching between the two subvariants.

Kurtz et al. (1989) and Okuda et al. (1989) have used X-ray diffraction studies to assess the influence of growth temperature on atomic ordering in GaInP epitaxial layers grown by OMVPE. Consistent with the results discussed above, Okuda et al. find that the degree of ordering is maximum at intermediate growth temperatures of ~650°C, whereas it is low on either side of the intermediate temperature. The results of Kurtz et al. (1989) appear to be anomalous.

It is interesting to note here that the predicted (fig. 4c) bulk, IC miscibility gap temperature of GaInP is $T^{IC}_{MG} = 688$°C. As discussed in the last paragraph of § 4.2, the *coherent* MG temperature T^{C}_{MG} is expected to be lower. Hence, ordering in GaInP has been generally observed in the T^{C}_{MG} to T^{IC}_{MG} temperature interval where *bulk*

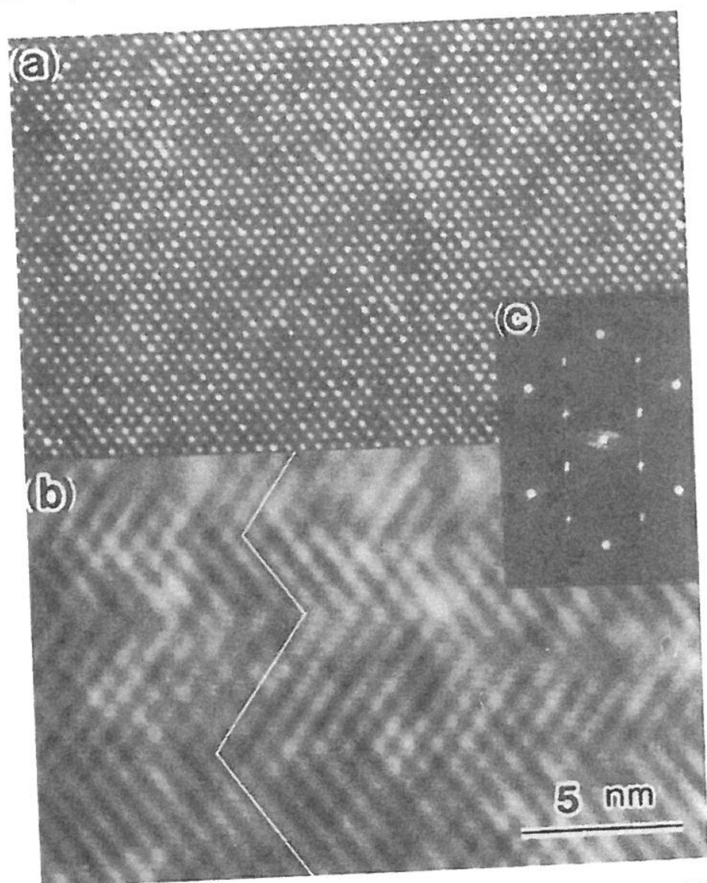

Fig. 26. (a) High-resolution electron micrograph of undoped GaInP grown at 680°C, (b) a reconstructed image of (a) with superlattice periodicities by image processing, and (c) a Fourier-transformed pattern of (b). After Morita et al. (1988).

phase-separation is suppressed by epitaxy, but *surface* phase-separation might still exist.

6.2. *Effects of growth rate*

The effects of growth rates on atomic ordering have been studied extensively by Jen et al. 1987, Cao et al. 1989, 1991, Mahajan et al. 1989, Kurtz et al. 1990a and McDermott et al. 1990. A common feature of these studies is that the increase in growth rate impairs the perfection of ordering. This effect is manifested most dramatically in electron diffraction patterns. Figure 27, reproduced from the study of Cao et al. (1991), shows the observed effects in GaInP epitaxial layers grown at various rates using OMVPE. As the growth rate is increased, diffuse intensity spikes develop through superlattice reflections: compare figs. 27a (rate of 4.1 μm/h) and 27d (12 μm/h), and they become more pronounced with increasing growth rate. In addition, these spikes are inclined slightly to the growth direction. The effect of increased growth rate on the perfection of order is analogous to that of decreased growth temperature.

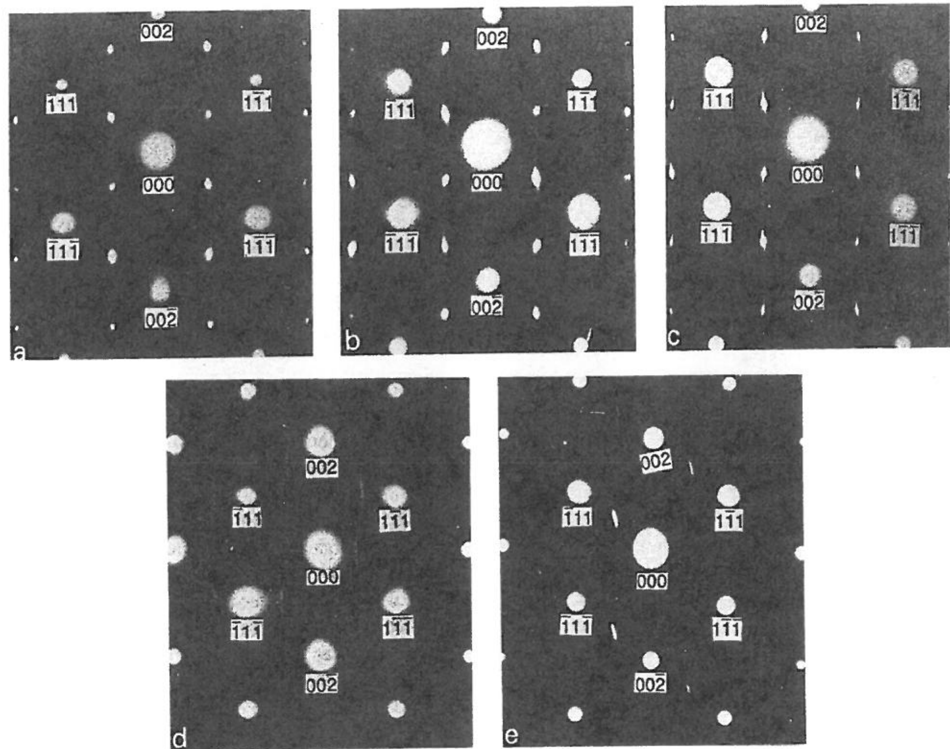

Fig. 27. TED patterns for GaInP layers grown at different growth rates (G_R). The electron beam was incident along the [110] direction. (a) $G_R = 4.1$ μm/h, (b) $G_R = 6.3$ μm/h, (c) $G_R = 8.3$ μm/h, (d) $G_R = 12$ μm/h, (e) $G_R = 12$ μm/h. From Cao et al. (1991).

The dramatic effect of growth rate on ordering is also evident from the studies of McDermott et al. (1990, 1991). These authors have used atomic layer epitaxy (characterized by a very low growth rate) to deposit GaInP layers by OMVPE. The layers are observed to have the lowest band-gap, possibly implying a high degree of ordering (see § 8.3).

The deviations of the $(1\bar{1}1)$–$(\bar{1}11)$ subvariant interfaces from the (001) plane would lead to spiking of the superlattice spots; the spike direction will be determined by the inclination of these interfaces with the (001) surface (Baxter et al. 1991, Cao et al. 1989, McDermott et al. 1990). In other words, the increased growth rate and reduced temperature must enhance the formation of the $(1\bar{1}1)$–$(\bar{1}11)$ interfaces, leading to the images observed in figs. 25 and 26.

6.3. *Effects of V/III ratio*

Gomyo et al. (1986, 1987) and Suzuki et al. (1988b) have investigated the influence of the V/III ratio on the band-gap anomaly and, later, on atomic ordering. Their results (Suzuki et al. 1988b) are reproduced as fig. 28. In discussing these results we assume that lower band-gaps imply higher ordering, as will be shown in § 8.3. These results show that (i) at high growth temperatures (e.g., 750°C), as the V/III ratio increases the band gap decreases, hence *more* ordering. (ii) At low growth temperatures (e.g., 600°C), as the V/III ratio increases the band gap increases, hence *less* ordering. A clear explanation for these effects has not yet emerged.

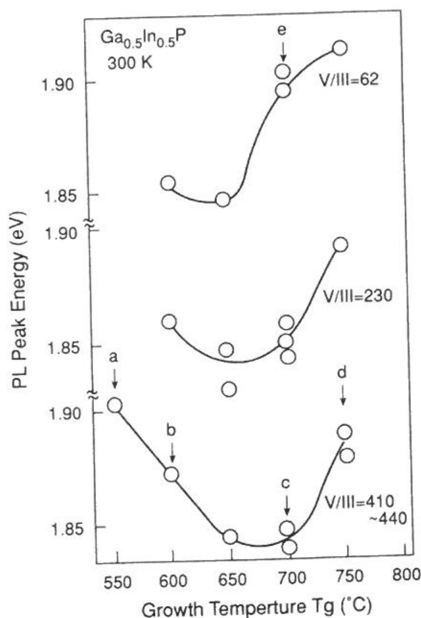

Fig. 28. The 300 K PL peak energy for $Ga_{0.5}In_{0.5}P$ as a function of growth temperature T_g and the V/III ratio. From Suzuki et al. (1988b).

6.4. *Effects of dopants*

Suzuki et al. (1988c), Gomyo et al. (1988a, 1989a), Meehan et al. (1989), and Kurtz et al. (1990b) have evaluated the effects of doping during growth on the occurrence of ordering in (001) GaInP epitaxial layers. Suzuki et al. (1988a,b,c) and Gomyo et al. (1988a, 1989a) find that in the case of Mg and Zn doping ordering is not affected until the hole concentration exceeds $\sim 10^{18}$ cm^{-3}. Similar results have been obtained for Se doping by Kurtz et al. (1990b) and Gomyo et al. (1989a).

Several reasons can contribute to the "poisoning" of order by doping. First, the presence of p-type dopant atoms above a critical concentration can destabilize thermodynamically surface reconstruction. As discussed in § 7.2, ordering is related to surface reconstruction. The removal of reconstruction can thus eliminate ordering. This argument is appropriate for Mg and Zn doping (acceptors) but not necessarily for Se doping (a donor). Second, high dopant concentration may change the Fermi level, hence speeding up the Ga and In diffusion. The increase in diffusivity of the Ga and In atoms may destroy the reconstruction and with it the ordering. Third, the occurrence of *dopant* diffusion in the layer *after* growth may destroy the already established ordering; diffusion-induced disordering has been observed in Zn-diffused GaInP epitaxial layers (Gomyo et al. 1987, Gavrilovic et al. 1988, Plano et al. 1988).

6.5. *Effects of substrate orientation and steps*

Various studies indicate that the orientation of the underlying substrate affects considerably the evolution of long-range order (Kuan et al. 1985, Jen et al. 1987, Gomyo et al. 1988a,b, 1991, T. Suzuki et al. 1988a, Ueda et al. 1989a, 1991, M. Suzuki et al. 1991, Buchan et al. 1992, Valster et al. 1991, Lin et al. 1992, Ueda and Nakata 1992, Suzuki and Gomyo 1993). Gomyo (1988b) and T. Suzuki et al. (1988a) have grown simultaneously $Ga_{0.5}In_{0.5}P$ layers on (001) and $(\bar{1}\bar{1}\bar{1})_B$ substrates and also on (001) + (110) substrates. They observe ordering on the (001) substrate, whereas it was completely absent in the $(\bar{1}\bar{1}\bar{1})_B$ and (110) growth. Likewise, Ueda et al. (1989a) do not observe ordering in $Ga_{0.5}In_{0.5}P$ layers grown by OMVPE on (110) GaAs substrates. On the other hand, Kuan et al. (1985, 1987), Ueda et al. (1991), and Ueda and Nakata (1992) observe CuAu-I-type order in AlGaAs and InGaAs layers grown on (110) GaAs and InP substrates by OMVPE and MBE. In addition, Ueda et al. (1991) found that a misorientation of 5° toward [001] accentuates the CuAu-I-type ordering. When compared with the results on (001) InGaAs layers, these findings indicate that an ordered structure in InGaAs epitaxial layers can be tailored by changing the orientation of the underlying substrate. Thus, previous studies showed that CuPt ordering does *not* occur on (111), (110), (511) and (311) substrates, but does occur on (001) and nearby orientations. In fact, CuPt ordering on (001) substrates is so common, that often attempts to grow other structures (e.g., CuAu) on the substrate by artificial shutter control (e.g., McDermott et al. 1991) result instead in the CuPt structure.

The importance of surface steps was first pointed out by Gomyo et al. (1988a).

Steps on surfaces can be produced in two different ways: (i) by tilting a surface away from a singular orientation; the separation between the steps is determined by the angle of misorientation; (ii) by patterning a surface. Following the work of Gomyo et al. (1988a), recent studies of Augarde et al. (1989), Bellon et al. (1989), and Chen and Stringfellow (1991) confirmed unequivocally that surface steps play an important role in deciding the relative subvariant population.

Augarde et al. (1989) and Bellon et al. (1989) carried out systematic studies on the influence of substrate misorientation on the evolution of the two CuPt-type ordered variants in GaInP layers grown on vicinal (001) GaAs substrates by OMVPE. They examined three types of samples: (i) in type-I samples layers were grown on exact (001) substrates; (ii) in type-II samples layers were grown on substrates that were 6° off (001) and were obtained by tilting around the $[1\bar{1}0]$ axis toward (110); (iii) in type-III samples layers were grown on substrates that were 6° off (001) and were obtained by tilting around the [110] axis toward $(1\bar{1}0)$. The layers were grown at 650°C. As expected, the $[1\bar{1}0]$ zone-axis electron diffraction patterns only exhibit the Bragg reflections of the zinc-blende structure. On the other hand, the [110] patterns show superstructure reflections. The results of Bellon et al. (1989) (similar to the results of Gomyo et al. (1988a, 1989b)) are reproduced as fig. 29. In figs. 29a (type-I samples) and 29b (type-II sample) superlattice reflections at positions $(h \mp \frac{1}{2}, k \pm \frac{1}{2}, l \pm \frac{1}{2})$ and $(h \pm \frac{1}{2}, k \mp \frac{1}{2}, l \pm \frac{1}{2})$ are observed: they correspond to the two $CuPt_B$ subvariants. In contrast, the type-III samples (fig. 29c) show only one set of superstructure reflections $(h \mp \frac{1}{2}, k \pm \frac{1}{2}, l \pm \frac{1}{2})$, which indicates that only one of the two ordered subvariants is present. The superstructure reflections in type-I samples have a lozenge shape (shown as an inset in fig. 29a) with their large diagonal tilted by ±8° off the [001] direction. The superstructures are elongated ellipses in type-II samples and become fairly circular in type-III samples. Furthermore, diffuse intensity is observed along the directions which are tilted from the [001] direction by ±8° and diffraction spots are shaped as elongated ellipses in type-II samples and become fairly circular in type-III samples. These observations point to the fact that the misorientation of the underlying substrate plays an important role in deciding the proportion of the two CP_B subvariants in the sample.

A demonstration of the role of steps in the ordering also comes from the elegant work of Chen and Stringfellow (1991). They fabricated a structure, fig. 30, where grooves are present on the surface of a (001) patterned GaAs substrate. These grooves are aligned along the [110] direction. When a GaAsP layer was grown on the patterned substrate, a different CP_B subvariant evolved from either side of the groove and an interface between the two subvariants was found close to the center of the groove, as illustrated in fig. 30.

7. Physical origins of long-range order in III–V alloys

7.1. *Early models based on bulk thermodynamics*

Initially, researchers attempted to seek an explanation for spontaneous ordering in semiconductor alloys in terms of *bulk thermodynamics*, i.e., by showing that the bulk

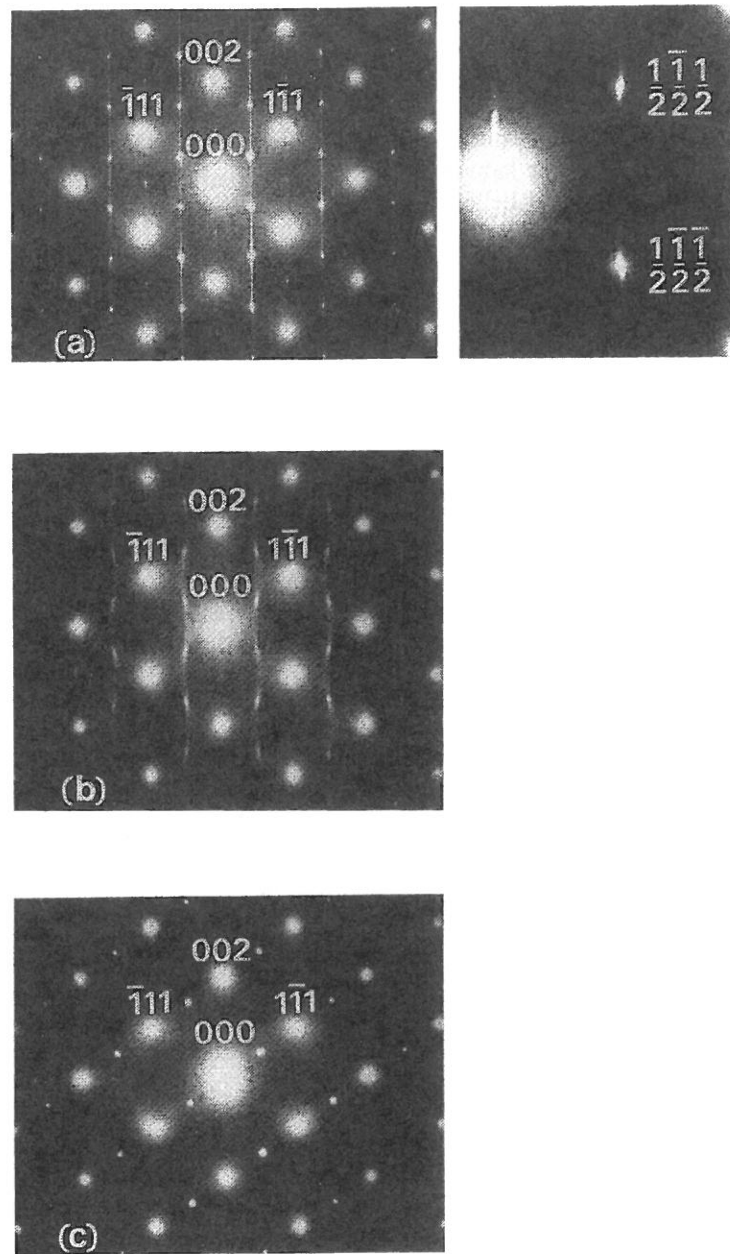

Fig. 29. The [110] diffraction patterns of the GaInP layers for an (a) exact (001) substrate (type-I samples), (b) 6° off toward (110) substrate (type-II samples), and (c) 6° off toward (1$\bar{1}$0) substrate (type-III samples). The growth temperature is the same in the three cases: 650°C. After Bellon et al. (1989).

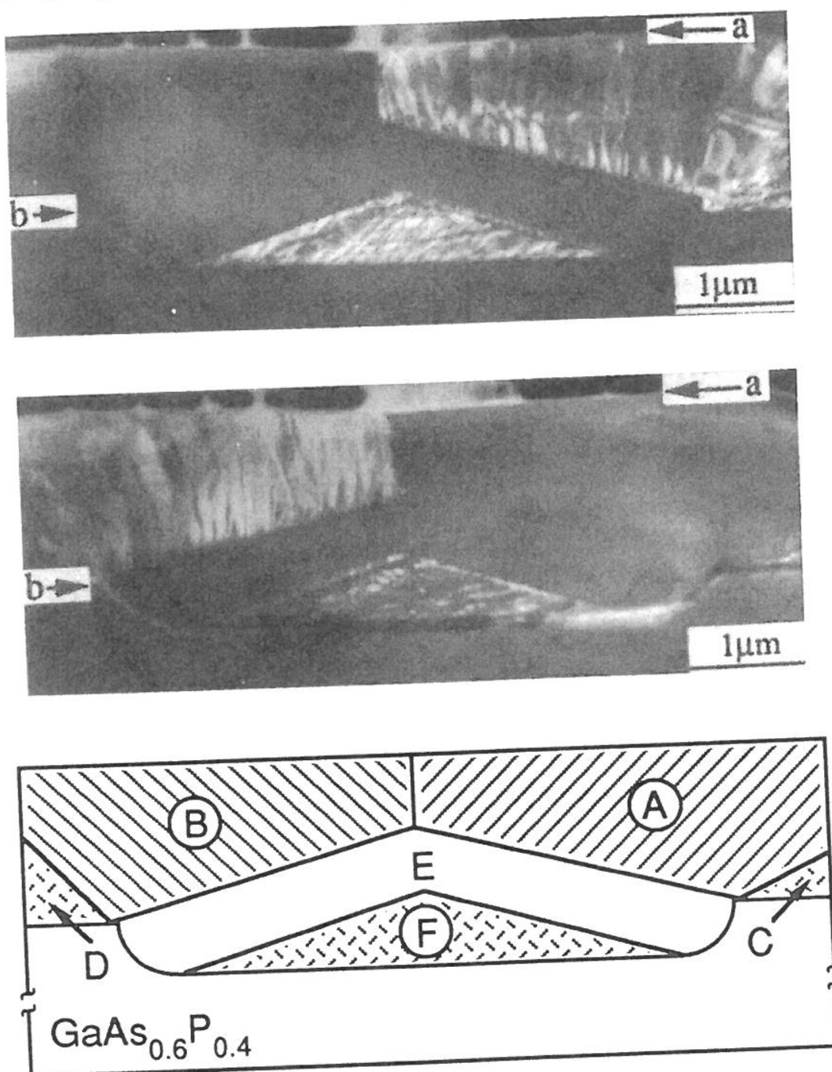

Fig. 30. Some [110] pole dark-field images of $GaAs_{0.5}P_{0.5}$ grown at 670°C on a $GaAs_{0.6}P_{0.4}$ substrate patterned with etched grooves running in the [110] direction: (a) $\frac{1}{2}(\bar{1}11)$ superspot, (b) $\frac{1}{2}(1\bar{1}1)$ superspot, and (c) schematic drawing of domains. Arrow "a" indicates the top surface of the $GaAs_{0.5}P_{0.5}$. Arrow "b" indicates the interface between the $GaAs_{0.5}P_{0.5}$ epilayer and the $GaAs_{0.6}P_{0.4}$ substrate. The symbol A (or B) denotes a very large domain of the $(\bar{1}11)$ or $(1\bar{1}1)$ variant. The symbols C, D, and F denote areas where small domains of the two variants coexist. The symbol E denotes completely disordered areas within the grooves. From Chen and Stringfellow (1991).

formation enthalpy ΔE_f of eq. (1) is negative for the observed ordered structures. (This corresponds to the "type-I" case in fig. 3.) However, as noted below, all these observations have turned out to be false.

Wang (1985) suggested that charge transfer between Al and Ga in $AlGaAs_2$ would

set up a Madelung energy that would stabilize the ordered CuAu-like structure, and hence explain the observed ordering. However, Wood et al. (1988) (see eqs. (23) and (25) there) showed that the relevant quantity in such an electrostatic model is the *excess* Madelung energy of a given structure with respect to that of the constituents (eq. (1) here). This depends both on the difference $\Delta q = q_A - q_B$ between the A charge in AC and the B charge in BC and the difference $\Delta Q = Q_A - Q_B$ between the A and B charges in the *ternary* (CuAu) structure. For the *excess* Madelung energy to be negative, one needs that $\Delta Q/\Delta q > 1.83$, a situation not supported for $AlGaAs_2$ by any first-principles calculation (Wood and Zunger 1988a, Wei and Zunger 1988a).

A second attempt at bulk thermodynamics has been made by van Schilfgaerde et al. (1986), who considered the excess Coulomb energy of various lattices, including both intersite (Madelung) and on-site Coulomb terms. They concluded that these terms may account for the observed ordering in $Al_{1-x}Ga_xAs$. However, Wei (1987) pointed out a (double-counting) error of a factor two in one of their terms; correcting this error showed that Coulomb effects do not distinguish the excess electrostatic energies of the random alloy from the phase-separated or the CuAu-ordered structure.

Next, Cohen and Schlijper (1987) calculated the formation energies of ordered $Ga_nAl_{4-n}As_4$ ($0 \leqslant n \leqslant 4$) structures using the augmented-spherical-wave method, finding $\Delta E_f(\mathrm{CA}) < 0$. An error in treating inequivalent atomic spheres as equivalent, corrected by them later (Cohen and Schlijper 1988) showed, however, that $\Delta E_f(\mathrm{CA}) > 0$ for this structure.

Later on, Shen et al. (1988) have shown on the basis of pseudopotential perturbation theory that the random $Al_{0.5}Ga_{0.5}As$ alloy has a *negative* mixing enthalpy, $\Delta E_{\mathrm{mix}} < 0$, despite the fact that the formation enthalpy of the ordered CA structure $\Delta E_f(\mathrm{CA})$ is positive. Lee et al. (1989) have later corrected an error in this calculation, confirming the earlier result (Wei and Zunger 1988a) that $\Delta E_f(\mathrm{CA}) > \Delta E_{\mathrm{mix}} > 0$, hence no bulk ordering.

More recently, Koiller et al. (1990) used a tight-binding total-energy model, finding that $AlGaAs_2$ exhibits CA ordering tendencies. However, Magri and Zunger (1991) found that the result of Koiller et al. is an artifact of using only two high-symmetry $\boldsymbol{k}$ points for sampling the Brillouin zone. A more accurate sampling gave $\Delta E_f(\mathrm{CA}) > 0$, hence no bulk ordering.

It is clear that bulk thermodynamics cannot explain the observed ordering. Indeed, accurate first-principles calculations on $GaInP_2$, $GaInAs_2$, Ga_2AsSb, and Ga_2PAs (Bernard et al. 1988, 1990, Wei et al. 1990, Dandrea et al. 1990a) showed that the CP structure always has $\Delta E_f > 0$ and even $\delta E_{\mathrm{ord}} > 0$ (fig. 3b), so bulk thermodynamics cannot explain its stability. Figure 5 shows indeed that the chemical energy ε of the CP structure is less negative than that of other ordered structures. More conclusively, Gomyo et al. (1988a) noted that if the observed CuPt ordering were of bulk origin, all the four CuPt {111} subvariants (equivalent in the bulk by symmetry) should be present. Since only two subvariants (($\bar{1}11$) and ($1\bar{1}1$)) are seen experimentally, ordering cannot reflect pure bulk effects.

The simplest surface effect is that considered by Suzuki et al. (1988a), i.e., *atomic relaxation at the surface* (not to be confused with surface *reconstruction*). They proposed that the size difference between Ga and In in GaInP could favor CP

ordering at the unreconstructed (001) surface because of size-mismatch driven relaxations. The major drawback of this model is that it implies that mixed-cation alloys (e.g., $Ga_{0.5}In_{0.5}P$) give $CuPt_B$ ordering while mixed-anion alloys (e.g., $GaAs_{0.5}Sb_{0.5}$) would give $CuPt_A$ ordering. However, Ihm et al. (1987), Murgatroyd et al. (1990), Chen et al. (1990), and Suzuki and Gomyo (1990b) have established conclusively that both types of alloys exhibit the same variant ($CuPt_B$). Hence, the atomic-relaxation model of Suzuki et al. (1988a) is incorrect, at least cannot explain the results. Furthermore, the total-energy calculations of Froyen and Zunger (1991a,b) showed that Ga–P versus In–P size differences are easily accommodated at the free *unreconstructed* surface by all ordered structures (through atomic relaxation perpendicular to the surface plane), so that size differences could not provide a *selective* driving force for ordering.

Matsumura et al. (1990, 1991) have followed the suggestion of Suzuki et al. (1988a) and have investigated the ground-state structures of a quasi-two-dimensional Ising Hamiltonian representing the *ideal* (i.e., unreconstructed) surface and its interactions with the underlying layers. They found that CuPt order can appear for a certain range of the ratio between second- and first-neighbor cation interactions. Using realistic surface-interaction values Osorio et al. (1992a,b) have shown, however, that the CuPt structure is not the ground state in the model of Matsumura et al. and that no ordered phases at all occur at growth temperatures. Along similar lines, Boguslawski (1990) calculated the surface energies of various relaxed but unreconstructed $GaInP_2$ surfaces using a purely elastic model, again finding small energy differences. We conclude that size-differences induced relaxation at the surface cannot explain the observed ordering.

7.2. *Surface-reconstruction induced long-range order*

It has been known for some time (Chadi 1987, Pashley et al. 1988, 1991) that the (001) surface of pure III–V semiconductors exhibits dimerization. The occurrence of cation and anion dimers introduces new surface symmetries. Murgatroyd et al. (1990) and Suzuki and Gomyo (1991) discussed the possibility that reconstructions at alloy surfaces could explain ordering. In *mixed-anion* alloys (e.g., $GaAs_{0.5}Sb_{0.5}$) the $CuPt_B$ variant would require dimers between *unlike atoms*, i.e., As–Sb, on anion-terminated surfaces, while the $CuPt_A$ variant requires dimers between like atoms (i.e., As–As and Sb–Sb). Murgatroyd et al. (1990) suggested that ordering in mixed-anion alloys could be related to a postulated energetic preference at the surface for mixed-anion (e.g., As–Sb) dimers. They have invoked the presence of 2×4 reconstruction on the anion-terminated (001) surface, suggesting that it facilitates the formation of As–Sb dimers along the $[1\bar{1}0]$ direction. If mixed-anion dimers are energetically favored, this would give the observed variant $CuPt_B$ provided that the mixed dimers are oriented in the same sense. If it is assumed that the two types of atoms can swap positions, then [110] rows containing both types of atoms along the $[1\bar{1}0]$ direction would result instead of the alternating [110] rows of As and Sb atoms that are required for the $CuPt_B$ ordering. However, in *mixed-cation* alloys, the $CuPt_B$ variant

in cation-terminated surfaces requires dimers between *like atoms* (e.g., Ga–Ga and In–In), while the $CuPt_A$ variant requires dimers between unlike atoms (e.g., Ga–In). Hence, the observed ordering in $Ga_{0.5}In_{0.5}P$ cannot be explained by the mechanism proposed by Murgatroyd et al. (1990).

Surface reconstruction exists both for cation-terminated and for anion-terminated (001) surfaces. It is pertinent to ask first what are the relative stabilities of these two cases for GaInP? Unfortunately, there are no experimental studies on the reconstruction of semiconductor *alloy* surfaces, so this question cannot be answered definitively at present. Experimental data is available only for surfaces of *pure* zinc-blende semiconductors, while for alloy surfaces we have only theoretical predictions based on first-principles total-energy calculations. The situation at present can be summarized as follows:

(i) For the (001) surface of GaAs, Kamiya et al. (1992) and Pashley et al. (1991) have shown that under normal MBE and MOCVD conditions a 2×4 *anion*-stabilized surface exists. However, Falta et al. (1992) have recently demonstrated, contrary to the previous results, that the first and second layers in GaAs (001) contain both Ga and As. First-principles calculations by Northrup and Froyen (1993) show that as the Ga chemical potential is increased the surface transforms from an As-rich $c(4 \times 4)$ through two distinct (2×4) structures and finally to a Ga-rich (4×2) phase which has two Ga dimers in the top layer and a third Ga dimer in the third layer.

(ii) Measurements on InP and InAs show both anion stabilization (Weiss et al. 1990, Hou et al. 1987, Reise et al. 1992) and cation stabilization (T.P. Chin et al. 1991, Wang 1988, Gruzza et al. 1985).

(iii) Calculations on GaInP/GaAs (001) surfaces (Froyen and Zunger 1993) show regions of Ga and In chemical potentials where the fully covered cation surface is stable.

It appears that while the anion-covered surface is generally preferred under normal growth conditions, at least partial cation coverage can exist too, in particular in In-containing systems. This subject awaits further experimental and theoretical studies. In what follows we will discuss calculations on reconstruction-induced ordering both for the cation surface (§ 7.2.1) and the anion surface (§ 7.2.2).

7.2.1. *Reconstruction of the mixed-cation surface*

To understand quantitatively the effect of surface reconstructions on ordering on a (001) substrate, Froyen and Zunger (1991a,b) and Bernard, Froyen, and Zunger (hereafter BFZ) (1991) have considered the following hierarchy of questions. (a) Why is atomic ordering preferred at the surface to phase separation, given that the reverse trend exists in the bulk (fig. 4)? (b) Why is there a preference for the (111) ordered CP structure rather than for differently oriented atomic layers, e.g., the (001) ordered CA or the (201) ordered CH structure? (Recall that in the bulk, CH is favored over CA and CP, see fig. 5.) (c) Given the (111) ordered structures, why is the CP_B variant preferred over CP_A? (d) Why is not there CP ordering in the lattice-matched $Al_{0.5}Ga_{0.5}As$ alloy? (Where CA, not CP, order is seen on (110) substrates but not (001), see table 2.)

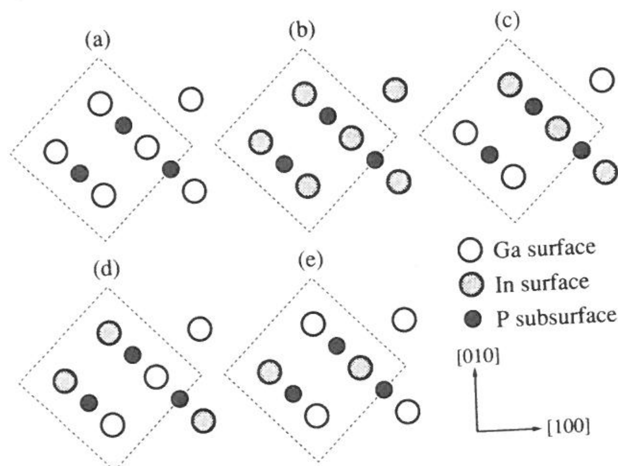

Fig. 31. Two-dimensional layer structures used in calculations of surface energies. By stacking these units one can obtain different 3D ordered structures. See table 6.

The basic methodology used by Froyen and Zunger to address these questions was to perform accurate first-principles calculations of *surface thermodynamics*, and invoke "kinetic arguments" only if the former explanation fails*. For example, as will be seen below, they find that the observed CP_B structure is *thermodynamically* stable at the near-surface atomic layers, but that (as discussed in § 2, see fig. 3, right) in deeper layers other phases are stabler. Kinetic barriers are thus needed to explain why the surface-stable structure persists after being covered by subsequent layers. The issues of thermodynamic stability at the surface can be phrased in terms of the relative stability of the five prototype two-dimensional (001) alloy layers shown in fig. 31. By stacking these prototype a, b, c, d, and e layers in different ways, many of the commonly observed three-dimensional (3D) structures e.g., phase separation or CA, CH, CP_A, and CP_B ordering can be obtained (table 5). Table 6 gives the calculated total energies of the various surface topologies, as obtained by Froyen and Zunger (1991a,b), using the first-principles pseudopotential method. These energies correspond to eq. (1), but now the energy E is calculated for a finite solid with a relaxed and reconstructed free surface rather than for an infinite three-dimensional periodic bulk system. These calculations address questions (a)–(d) above as follows:

(i) Table 6 shows that many ordered structures have lower energies than complete surface phase-separation (denoted "a + b" in table 6), hence $\Delta E_f < 0$ *at the surface*. In other words, phase separation, which is the stablest arrangement in the bulk (fig. 4) due to the overriding effect of volume deformation energies $\Delta E_{VD} \gg 0$, is

* We say that an ordered structure is "induced by surface thermodynamics" if the observed geometry corresponds to a minimum in the surface free energy. In contrast, we say that an ordered structure is induced by kinetics if it can be argued that for this geometry the free energy is *not* a minimum, but the atoms are stuck in this configuration due to inability to overcome activation barriers.

Table 5
3D structures characterized by stacking of the (001) bilayers shown in fig. 31. The structure is identified both by a superlattice notation (the direction G and the repeat period $2n$) and by the notation used in the text. Each layer is shifted laterally as indicated in parentheses (in units of the zinc-blende lattice constant). Several other structures are degenerate with those tabulated: [110] $n=1$ is identical to [001] $n=1$ CA, [201] $n=2$ CH is degenerate with [021] $n=2$ CH, and [010] CA is degenerate with [100] CA. The [102] $n=2$ and [012] $n=2$ CH structures have (001) layers that cannot be represented by the 2×2 patterns in fig. 31. Notice that the d layer of fig. 31 occurs only in the observed CP_B phase and in the Y2 superlattice. The two are distinguished only by the third- and fourth-layer stacking. From Froyen and Zunger (1991a).

Structure			Layer number			
G	n	Name	1	2	3	4
(Binary)		zinc-blende	a(0, 0)	a($\frac{1}{2}$, 0)	a(0, 0)	a($\frac{1}{2}$, 0)
(Binary)		zinc-blende	b(0, 0)	b($\frac{1}{2}$, 0)	b(0, 0)	b($\frac{1}{2}$, 0)
[021]	2	CH	e(0, 0)	e($\frac{1}{2}$, 0)	e($\frac{1}{2}$, $\frac{1}{2}$)	e(0, $\frac{1}{2}$)
[100]	1	CA	e(0, 0)	e($\frac{1}{2}$, 0)	e(0, 0)	e($\frac{1}{2}$, 0)
[001]	1	CA	a(0, 0)	b($\frac{1}{2}$, 0)	a(0, 0)	b($\frac{1}{2}$, 0)
[111]	1	CP_A	c(0, 0)	c($\frac{1}{2}$, 0)	c($\frac{1}{2}$, $\frac{1}{2}$)	c(0, $-\frac{1}{2}$)
[110]	1	Y2	c(0, 0)	c($\frac{1}{2}$, 0)	c(0, 0)	c($\frac{1}{2}$, 0)
[$\bar{1}$11]	1	CP_B	d(0, 0)	d($\frac{1}{2}$, 0)	d($\frac{1}{2}$, $-\frac{1}{2}$)	d(0, $\frac{1}{2}$)
[$\bar{1}$10]	2	–	d(0, 0)	d($\frac{1}{2}$, 0)	d(0, 0)	d($\frac{1}{2}$, 0)

Table 6
Surface energies for the various $GaInP_2/GaAs(001)$ reconstruction modes (fig. 31) discussed in the text. The energies are in meV per surface atom relative to the unreconstructed a + b (phase-separated) surface (surfaces a and b have their own separate zero of energy). We show separately the results of the dimerized + buckled + tilted (DBT) surface with Ga up and with In up. Blank entries in the "dimerized" row refer to cases where a pure dimerization without buckling or tilting cannot be defined. From Froyen and Zunger (1991a).

Surface geometry	Surface type					
	a	b	a + b	c	d	e
Unreconstructed	0	0	0	14	−9	2
Dimerized	−785	−366	−575	–	–	−620
Dimerized + buckled	−732	−448	−590	–	−692	−602
DBT-Ga up	−836	–	−701	−684	−623	−715
DBT-In up	–	−564	−701	−684	−799	−705

predicted to be partially suppressed at the surface if the latter orders*. This reflects the combined energy lowering due to coherent epitaxy and surface reconstruction. Dimerization or pure a = GaP and pure b = InP lowers the energy less than dimerization in mixed structures, e.g., e = CH. This answers question (a) above. Note, however,

* *Disordered* layers could, however, show more phase separation than ordered layers since the phase-separated and disordered phase are closer in energy than the ordered and phase-separated phase (see fig. 4 in Osorio et al. 1992a).

that *partial* phase-separation (at finite temperatures) is not ruled out by these zero-temperature calculations.

(ii) For relaxed but *unreconstructed* surfaces the energy difference between the various surface arrangements are considerably smaller than kT_g, where $T_g \sim 900$ K is the growth temperature. Hence, simple relaxations derived by atomic size mismatch (Suzuki et al. 1988a, Boguslawski 1990) cannot explain preferential ordering.

(iii) The situation changes significantly when reconstructions are permitted (figs. 32 and 33). Surface dimerization results in *heteropolar* (Ga–In) dimers on surfaces c = CP_A and e = CH (fig. 33), but in *homopolar* (Ga–Ga or In–In) dimers on surfaces a = GaP, b = InP, and d = CP_B (fig. 32). The significant topological difference between CP_A and CP_B is hence the occurrence of unlike atom versus like atom surface dimers, respectively. Relative to the undimerized surfaces, dimerization lowers the energy by an average of 600 meV per surface atom (table 6, row 2). In addition to dimerization there are two other energy-lowering reconstructions within the 2×2 surface unit cell: first, dimers relax perpendicularly to the surface creating $[\bar{1}10]$ dimer rows of

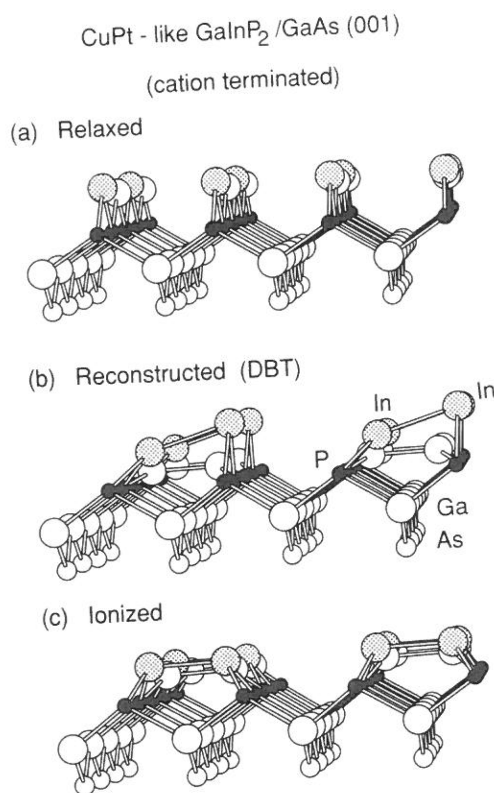

Fig. 32. Calculated equilibrium surface geometries of CuPt-like cation-terminated $GaInP_2$/GaAs (001). (a) Relaxed but unreconstructed, (b) reconstructed, and (c) the structure obtained after the highest occupied level is ionized. Observe the buckling and tilting in (b) which disappears after ionization. Ga (white), In (grey), and P (black). From Bernard et al. (1991).

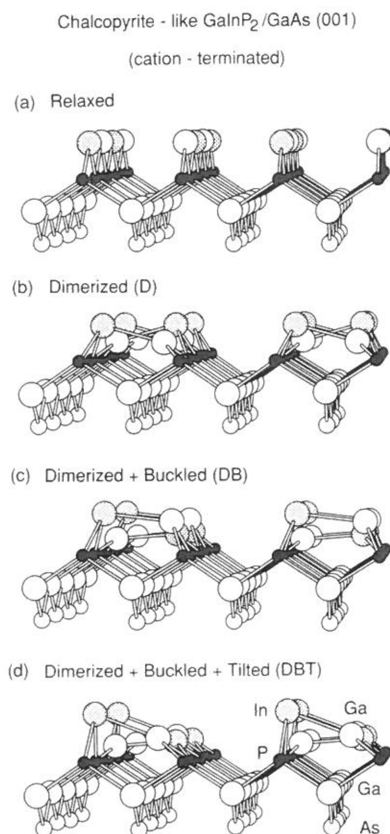

Fig. 33. Same as fig. 32 but for the chalcopyrite surface structure. (a)–(d) show the changes in structure as additional energy-lowering displacements are allowed. Note that the dimers here are heteropolar while those of fig. 32 are homopolar. Ga (white), In (grey), and P (black) are on top of GaAs (white).

alternating high and low dimers (e.g., see fig. 33c). We will refer to this as "buckling". Relative to the dimerized, unbuckled surface, buckling lowers the energy of the b surface (table 6, row 3), but raises the energy for surfaces a and e (so these surfaces will not buckle). Hence, buckling prefers the $d = CP_B$ structure over the $e = CH$ structure. This answers question (b) above, i.e., surface CP is preferred to surface CH ordering mainly due to buckling. Second, the high dimer tilts in the [110] direction, becoming nonhorizontal, whereas the low dimer remains virtually horizontal (e.g., see figs. 32b, 33d). Since the four surface sites are inequivalent in the final geometry, there are two different ways of distributing the two Ga and the two In atoms in each of the topologies, c, d, and e. We will characterize this by the type of atom (Ga or In) occupying the site on the high dimer that tilts upwards. The last two rows of table 6 show that the $d = CP_B$ surface strongly prefers having the larger In atom on the high dimer, whereas the $e = CH$ surface shows a slight preference for the smaller (but more electronegative) Ga atom to be tilted up. Tilting leads to

a uniform energy lowering of 100 meV but does not affect the relative stability of the surfaces (table 6).

As shown in table 6, the full reconstructions (dimerization, buckling, and tilting) considerably lower the energy of all the surfaces and, most significantly, make the surface corresponding to the observed CP_B ordering (d) the lowest in energy, by 84 meV per surface atom. *Thus, surface reconstruction not only favors atomic arrangements that are unstable in the bulk, but it also results in energy differences large enough to produce order at* T_g. This answers question (c) above.

(iv) Since $Al_{0.5}Ga_{0.5}As$ *does not order* when grown on (001) substrates (table 2) but $Ga_{0.5}In_{0.5}P$ does, it is interesting to examine whether the above theory will reproduce this different behavior. Froyen and Zunger (1991a) have compared the energies of the $GaInP_2$ surfaces to those of $AlGaAs_2$. They separately considered Ga and Al as the highest atom on the high dimer (table 7). They find that the energy of surface $d = CP_B$ is now only 9 meV per surface atom below that of the next lowest configuration (the e surface), so the energy difference is negligible compared to kT_g. Hence, the resulting surface topology in AlGaAs/GaAs (001) is likely to be disordered. This is consistent with the experiment of Kuan et al. (1985), where $Al_{0.5}Ga_{0.5}As/GaAs$ (001) was found to be disordered while ordering was seen only for growth on the (110) surface (table 2). This answers question (d) above. (Note that the model of Ogale and Madhukar (1991) attempts to explain ordering for $Al_{0.5}Ga_{0.5}As/GaAs$ (001), which is *not* observed. The recent simulated-annealing study of the stepped (001) surface of $Al_{0.5}Ga_{0.5}As$ (Ogale et al. 1992) predicted CuPt ordering, which is also not observed.)

There are two differences between the behavior of CP $AlGaAs_2$ and $GaInP_2$. First, in $AlGaAs_2$ the calculation shows that Ga prefers to be in the up position (table 7) while in $GaInP_2$ the In is in the up position (table 6). Second, the CP structure is ten times more stable in $GaInP_2$ than in $AlGaAs_2$.

● Regarding the first difference, we note that the choice of the atom occupying the up position is decided by a combination of (i) electronic charge transfer and (ii) steric size effects. Since Al and Ga have similar sizes, there is no steric effect for this system, so the preference is purely electronic. The atom in the up position is always found to *receive* charge from the atoms in the down positions (Froyen and Zunger 1991a). Since the atomic s-orbital binding energy of Ga (−9.2 eV) is deeper

Table 7
Surface energies for fully reconstructed cation-terminated $Al_{0.5}Ga_{0.5}As/GaAs(001)$ system. The energies are in meV per surface atom relative to the a + b phase-separated surface. The dimer type (Al up or Ga up) refers to the atom furthest from the surface. From Froyen and Zunger (1991a).

Dimer type	Surface type		
	a + b	d	e
Al up	0.0	38	7
Ga up	0.0	−35	−26

than that of Al (-7.8 eV) Al$\rightarrow$Ga charge transfer occurs. Since the atom in the up position receives charge, Ga with the deeper orbital energy takes up this position. In $GaInP_2$ the steric effect is important: the atom in the up position is the larger In atom. The Ga$\rightarrow$In charge transfer is in the direction of higher electronegativity ($\chi_{Al} = 1.5$, $\chi_{Ga} = 1.6$, and $\chi_{In} = 1.7$).

● The key to the second question is the *dimerization* energy in Ga–In versus Ga–Al: tables 6 and 7, i.e., that the energy lowering due to Ga–In dimerization is far greater than that due to Ga–Al dimerization. Consequently, the dimerization-induced stability of the CP structure is greater in $GaInP_2$ than in $AlGaAs_2$. Note that the Al–In pair has the largest electronegativity difference as well as s-orbital difference among the three combinations Al–Ga, Ga–In, and Al–In. According to the calculation of Dandrea et al. (1990a), the Al–In pair should be the stablest in superlattice form, showing a strong stabilizing Al$\rightarrow$In charge transfer (fig. 3b).

We see that the four basic questions (a)–(d) can be answered in terms of *surface* thermodynamics without invoking at this point kinetic arguments. The latter will be used below to discuss growth dynamics (§ 7.4). Given that (a) the suppression of phase separation, (b) the preference of (111) over (001) or (201) ordering, (c) the preference of B-type over A-type (111) ordering, and (d) the instability of (111) ordering in $AlGaAs_2$ all reflect surface thermodynamics, we next investigate whether this thermodynamic surface stability has "electronic" or "elastic" origins.

We find that all reconstructions are electronically driven, so simple elastic models (Boguslawski 1990) will miss them. The unreconstructed cation surfaces (figs. 32a and 33a) have two broken bonds per surface atom, each containing $\frac{3}{4}$ electron. When the surface dimerizes, two electrons per dimer occupy σ-type bonding orbitals (shown in figs. 34c,d). This leaves one unpaired electron per dimer, making the unbuckled, dimerized surface metallic. The surface breaks the "symmetry" by buckling and tilting. Of the four atoms on a dimer pair, three relax towards planar sp^2 configurations and the fourth atom moves up into a pyramidal s^2p^3 configuration with bond angles of approximately 90°. This allows the fourth atom to bind the two unpaired electrons in a dangling-bond orbital (fig. 34b). Hence, the "high atom" accepts electrons from the "low" atom. The lowest unoccupied state is a bonding p_π state on the low dimer (fig. 34a). Thus, a pair of dimers form a "negative-U" system where two neutral (horizontal) dimers are unstable with respect to disproportionation into a positively charged low dimer and a negatively charged high dimer. This analysis suggests that if the two electrons in the dangling-bond state (fig. 34b) on the high dimer could be removed, e.g., by heavy p-type doping or by excitation, both dimers would prefer planar sp^2 arrangements and the energy advantage of the $CuPt_B$ surface should vanish. The calculations of Froyen and Zunger (1991a) show that the energy difference between the d$=CP_B$ and e$=$CH surfaces is indeed reduced to 1 meV per surface atom upon the removal of two electrons per surface unit cell from the dangling bond. The resulting geometry for the d surface is shown in fig. 32c. We see that buckling and tilting disappears and along with them the energetic stabilization of the CuPt surface. We conclude that buckling and tilting of surface dimers are driven by the electronic positioning of the Fermi level within the surface band, not by elastic size differences.

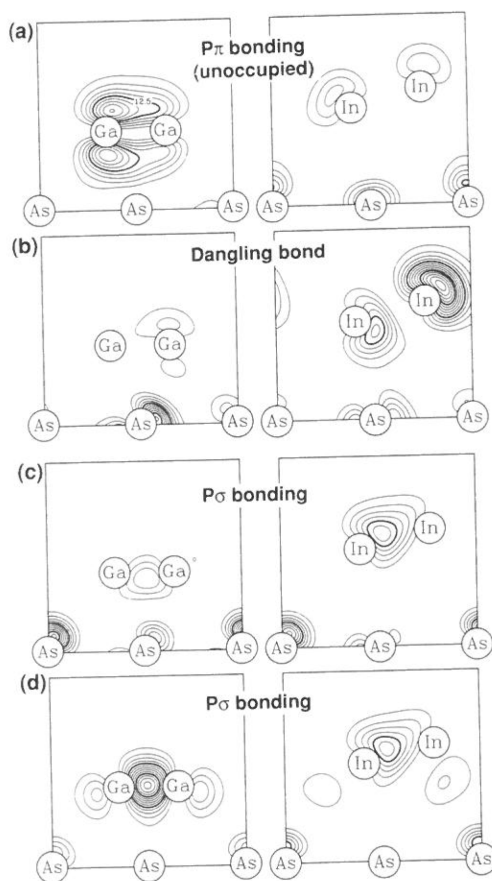

Fig. 34. Contour plots of selected surface squared wavefunctions for the CP surface at the Γ point in the Brillouin zone in two cuts: through the low Ga–Ga dimer (left) and the high In–In dimer (right). (a) A Ga–Ga p_π bonding state (lowest unoccupied state). (b) An In dangling-bond state (highest occupied state). (c), (d) The deeper Ga–Ga and In–In p_σ bonding states. From Bernard et al. (1991).

7.2.2. Reconstruction of the anion surface

We next ask how surface energies are modified when the cation layers are covered by phosphorus. We denote this first subsurface layer by $h = 1$ (in our notation, the top surface is $h = 0$ while $h = 1, 2, \ldots$ is the first, second, etc. subsurface layer). As before, Froyen and Zunger (1991a) used a 2×2 unit cell and calculated the energies of the prototype topologies a, b, d, and e (fig. 31) on a (001) GaAs substrate when all are covered by a single monolayer of P that is allowed to dimerize. The energy-minimizing geometry for the anion surface is shown in fig. 35. The P–P dimer length is found to be shorter than the Ga–In cation dimer length (fig. 32b), leading to much larger subsurface relaxations in the anion-terminated case. In addition to the dimerization they observed a buckling of the alternate dimers (fig. 35). The buckling is less than that for the cation surface, and the dimers are horizontal. The surfaces are still

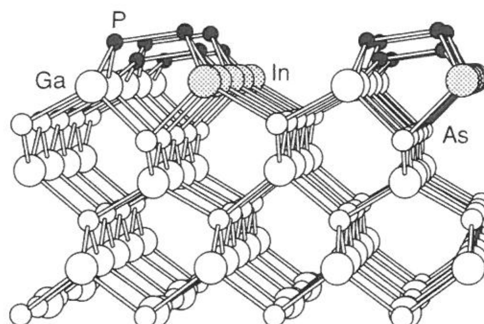

Fig. 35. Side view of the anion-terminated slab used for the surface calculations. The surface atoms are P (black), Ga (white), and In (grey) on top of a (001) substrate GaAs layer (white). From Bernard et al. (1991).

metallic and therefore likely to undergo additional reconstruction (Northrup and Froyen 1993). Within the 2×2 cell they find that the differently arranged cation layers below the phosphorus surface show suppression of phase separation, but little structural selectivity. *Hence, anion termination alone does not produce any ordering at* $h = 1$.

7.2.3. *How are the atomic arrangements in subsurface layers affected by surface geometry?*

Having discussed the relative energies of the cation-terminated ($h = 0$) and anion-terminated ($h = 1$) top surfaces, we now turn to discussion of the energies of more deeply buried ($h \geqslant 2$) cation layers. Figures 36–39 show the layer structures and results of the total-energy calculations of Bernard, Froyen, and Zunger (BFZ), (1991).

In figs. 36 ($h = 2$) and 38 ($h = 4$) the top surface layer is cationic. The cations in this top layer are permitted to take up different layer topologies, e.g., $X = CP_A$, CP_B, CH, or phase separation (PS) into binary end members. Under this top layer we find a phosphorus layer. Going one layer deeper, we again find a cationic layer. In the calculation of fig. 36 we permit this $h = 2$ cation layer to take up different topologies $Y = CP_A$, CP_B, etc. In the calculation of fig. 38 we permit also the $h = 4$ subsurface cationic layer to take up different structures. Figures 36 and 38 show the calculated energies for many possible combinations of X and Y, all for cation-terminated films. Similar results are shown in figs. 37 ($h = 3$) and 39 ($h = 5$) for anion-terminated surfaces. In all cases the geometry of the top two layers was obtained from the pseudopotential calculation (the geometry is shown in figs. 32, 33, and 35), while deeper layers were treated by an elastic valence force field (VFF) whose parameters were fitted to reproduce first-principles results. This is reasonable, since the structure of *buried* layers is primarily decided by the elastic response to the

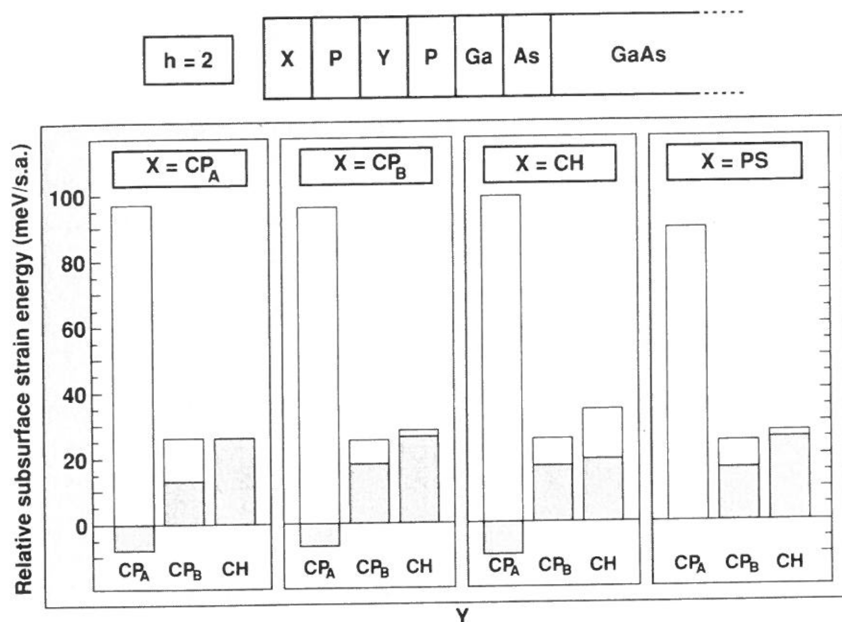

Fig. 36. Strain energies of $GaInP_2$ due to structural changes in the second subsurface layer ($h = 2$). Each panel gives the energies of the c, d, and e topologies in layer Y (relative to phase separation a + b) for specific topologies in layer X. The empty and shaded bars correspond to translations of the pattern by $a/\sqrt{2}$ in the [110] or [$\bar{1}$10] direction. We show the energies of the layers underneath a P-terminated surface with buckled dimers (a) and with the buckling removed (b). The units are meV per surface atom (SA). Note that only CP_A is stable at $h = 2$. From Bernard et al. (1991).

structure of the upper layers. The energies in figs. 36–39 are given relative to the phase-separated state in the hth layer. Negative energies hence denote structures that are stabler than layer phase-separation. Note that the subsurface elastic effects of the surface reconstruction result in a splitting of the energies of the two phase-reversed partners of a particular topology, and these are depicted separately in figs. 36–39 by the white and shaded areas. We will refer to these phase-reversed structures as "subvariants" of CP_A, CP_B, or CH (the term "variant" is reserved for the A and B partners of the CP structure).

From the results of BFZ (1991) we conclude the following:

(i) *The results for $h = 2$ in the cation-terminated surface* (fig. 36) show that the low-energy CP_A subvariant (shaded CP_A rectangles in fig. 36) is favored slightly (by about 10 meV/surface atom) over the next-lowest-energy arrangement, the phase-separated state.

(ii) *For the $h = 3$ layer in the anion-terminated surface* (fig. 37a) the energy selectivity is much greater, with the $Y = CP_B$ layer structure being preferred by about 35 meV/surface atom over the next competitor, regardless of the topology of the first surface layer (X). If we neglect buckling of dimers and use a 2×1 surface (fig. 37b) the CP_B stability increases to ~ 90 meV. One can understand these trends by inspect-

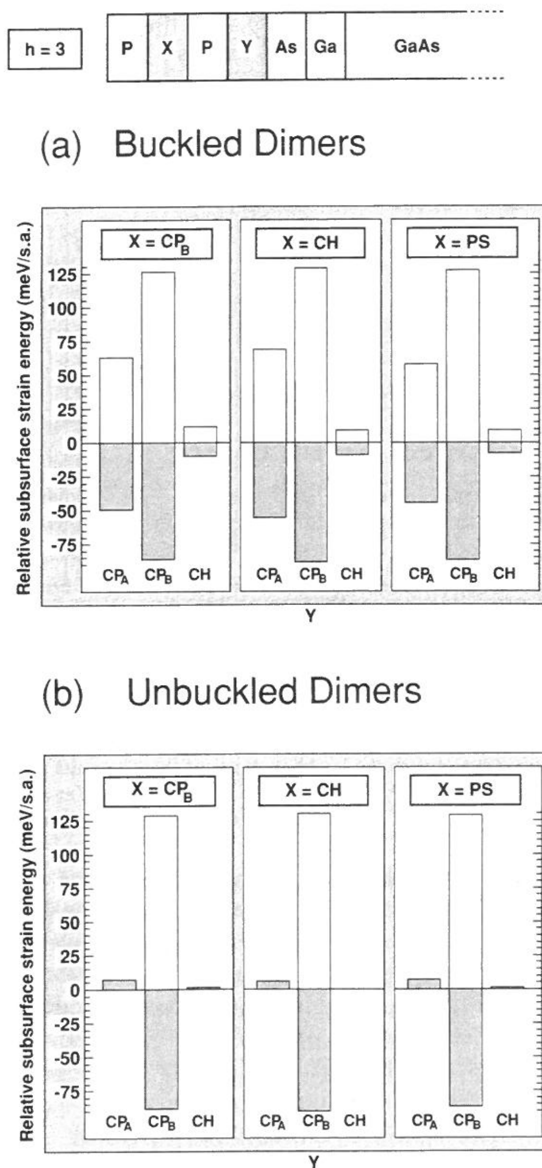

Fig. 37. Strain energies of $GaInP_2$ due to structural changes in the third subsurface layer ($h = 3$). Each panel gives the energies of the c, d, and e topologies in layer Y (relative to phase separation a + b) for specific topologies in layer X. The empty and shaded bars correspond to translations of the pattern by $a/\sqrt{2}$ in the [110] or [$\bar{1}$10] direction. We show the energies of the layers underneath a P-terminated surface with buckled dimers (a) and with the buckling removed (b). Units are meV per surface atom. Note that the CP_B structure is the stablest at $h = 3$. From Bernard et al. (1991).

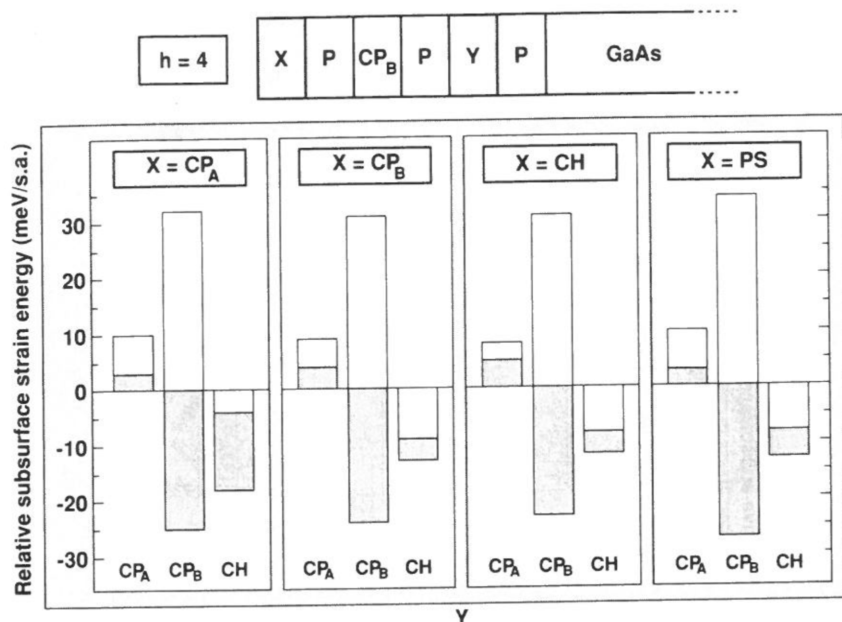

Fig. 38. Strain energies of $GaInP_2$ due to structural changes in the fourth subsurface layer ($h=4$). Each panel gives the energies of the c, d, and e topologies in layer Y (relative to phase separation a + b) for a specific topology in layer X. The empty and shaded bars correspond to translations of the topologies by $a/\sqrt{2}$ in the [110] or [$\bar{1}$10] direction. Units are meV per surface atom. Note that the CP_B structure is the stablest at $h=4$. From Bernard et al. (1991).

ing figs. 40c and 40d, which show the first-principles relaxed atomic positions for the CP_B surface on a GaAs substrate, with arrows indicating major relaxation directions of subsurface atom rows. In fig. 40c we see row relaxations induced primarily by *dimerization* of the surface P atoms. The large In atom will occupy the *dilated site* which is denoted in fig. 40c with an up-arrow, while the smaller Ga atom will occupy the *compressed site* directly below the P–P surface dimer, indicated by a down-arrow. This is the two-dimensional CP_B structure. Thus, surface ($h=0$) dimerization exerts a size-preference at $h=3$. Subsequent calculations by Osorio et al. (1992a,b) have shown that if the $h=3$ site *under* the P–P dimer is occupied by In rather than Ga, the energy is increased by 750 meV/(2 × 2 cell). Hence, there is a very strong energetic preference to avoid such local defects.

(iii) *For the $h=4$ layer in the cation-terminated surface* shown in fig. 38, again Y = CP_B is favored over the other structures. To explain this, fig. 40b shows the major row relaxations, induced primarily by *buckling* of the surface dimer rows. One can see from these that the two CP_B subvariants provide the best and worst fits at $h=4$. The most important result of the $h=4$ calculation is the identity of the lowest-energy CP_B subvariant: *we see that the low-energy subvariant corresponds to true three-dimensional CuPt ordering of the surface ($h=0$) plus the fourth subsurface layers ($h=4$).* The high-energy subvariant corresponds to having an anti-phase boundary

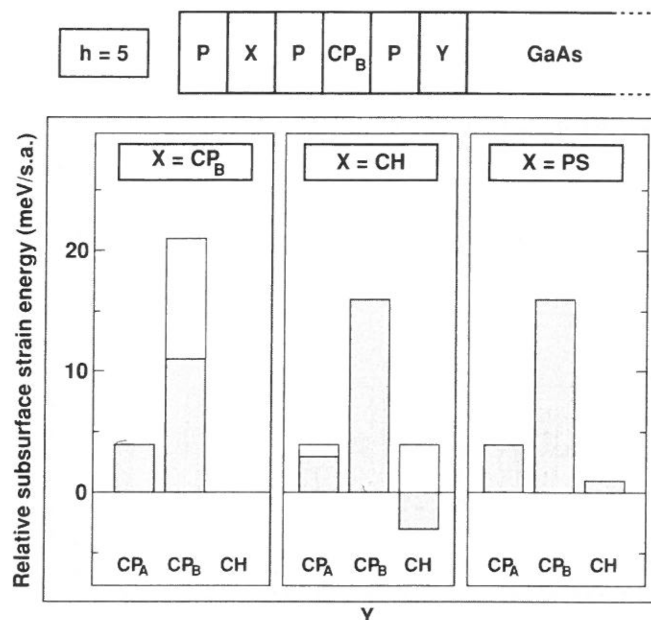

Fig. 39. Strain energies of $GaInP_2$ due to structural changes in the fifth subsurface layer ($h = 5$). Each panel gives the energies of the c, d, and e topologies in layer Y (relative to phase separation a + b) for a specific topology in layer X. The empty and shaded bars correspond to translations of the pattern by $a/\sqrt{2}$ in the [110] or [$\bar{1}$10] direction. Units are meV per surface atom. Note that structural selectivity is nearly lost at this $h = 5$ layer. From Bernard et al. (1991).

between $h = 0$ and $h = 4$. Hence, a cation-terminated surface is predicted in fig. 38 to produce the correct 3D stacking of the first four layers. Furthermore, the $h = 4$ layer takes up the CP_B structure irrespective of whether the surface is ordered, disordered, or phase separated. In contrast, the flat, anion-terminated surface, while showing a clear stability of the 2D CP_B structure at $h = 3$ (fig. 37), does not produce any intrinsic phase-locking to explain 3D CP_B.

(iv) *For the $h = 5$ layer in the anion-terminated surface* shown in fig. 39, we again present only results for which the third subsurface (cation) layer has the (lowest-energy) CP_B layer structure, since there is only weak dependence of the relative energies on the state of order of that layer. Here, at $h = 5$ the stability sequence has nearly reverted to that of the bulk (see fig. 5), with the CH phase being the most stable and CP the least stable. At this point one recovers the basic energetics of three-dimensional epitaxial layers (e.g., the ordered CH phase in the epitaxial phase diagram of fig. 9b).

In summary, we see that the surface *dimerization*, the most well-verified and the most energetically favored (table 6) of the surface reconstructions found in the first-principles calculations, induces a strong preference for CP_B layer ordering at $h = 3$ when the top surface is anion-terminated, whereas surface dimer row *buckling* induces a preference for CP_B layer ordering at $h = 0$ and $h = 4$ when the top surface is cation-

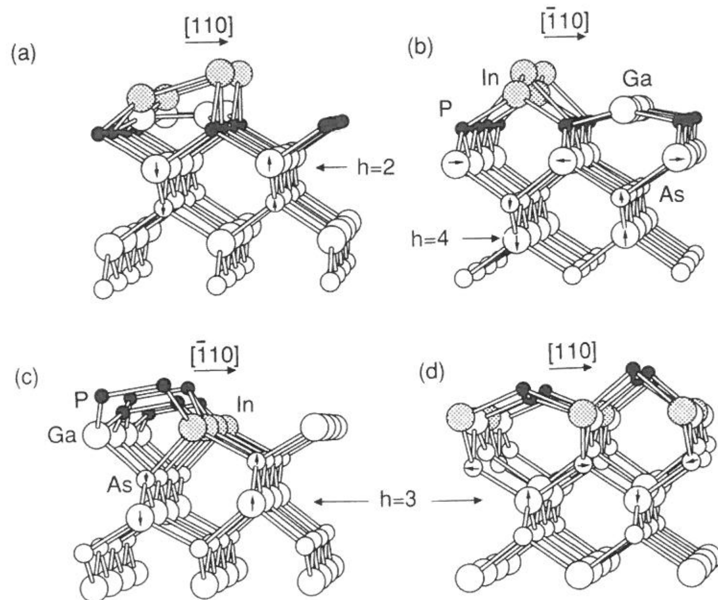

Fig. 40. Side view of atomic geometries for the cation terminated ((a) and (b)) and anion-terminated ((c) and (d)) $GaInP_2$ d-surfaces. The surface atoms are Ga (white), In (grey), and P (black) on top of a (001) substrate GaAs layer (white). The arrows illustrate the relaxation of subsurface atom rows (see text).

terminated. Tilting of surface dimers appears to have no major qualitative effect on subsurface layers, though electron-counting arguments suggest that it is closely related to the buckling of dimer rows. A nearly bulk-like stability sequence is recovered by $h = 5$.

7.3. *The surface phase diagram*

All of the energetics described above can be cast into the language of a generalized Ising model (Osorio et al. 1992a,b). One constructs a configurational "cluster-expansion (CE) Hamiltonian" $H_{CE}(\boldsymbol{\sigma})$ that describes the energy of the surface and subsurface $Ga_{1-x}In_xP$ epitaxial layers in terms of a set of pseudospin variables

$$\sigma_i = -1 \quad \text{for Ga on } i, \\ \quad = 1 \quad \text{for In on } i, \tag{23}$$

decribing the occupation of the cation sublattice sites i by Ga or In. The configuration vector $\boldsymbol{\sigma}$ describes the occupation of N cations in each of the n layers: $\boldsymbol{\sigma} = \{\sigma_1, \sigma_2, \ldots, \sigma_{Nn}\}$. The configurational Hamiltonian is expanded as a series of interaction energies $\{J_F\}$ within various "figures" $\{F\}$ (clusters of n_F sites):

$$H_{CE}(\sigma) = N \sum_F D_F J_F \bar{\Pi}_F(\boldsymbol{\sigma}), \tag{24}$$

where the degeneracy D_F is the number of symmetry-equivalent figures and $\bar{\Pi}_F(\boldsymbol{\sigma})$ is the average spin product $\langle \sigma_i \sigma_j \dots \sigma_{n_F} \rangle$. The interaction energies $\{J_F\}$ are determined by fitting a large number of total-energy calculations (e.g., figs. 36–39) to eq. (24). Such an Ising-like Hamiltonian is a convenient tool for (i) predicting the energy of configurations $\sigma' \neq \sigma$ (not used in the fit), (ii) searching for $T = 0$ ground-state structures (by direct constrained minimization), and (iii) calculating $T \neq 0$ thermodynamic functions (by standard lattice-statistics approximations, such as the cluster-variation method (Kikuchi 1974)).

Rather than design an a priori phenomenological configurational Hamiltonian, Osorio et al. (1992a,b) used the total-energy calculations described in figs. 36–39, as well as a few hundred additional configurations $\{\Sigma\}$, and then identified the significant interaction energies that should enter the Hamiltonian H_{CE}. For each configuration Σ they defined from the directly (d) calculated total energy $E_{\mathrm{d}}(\Sigma)$, i.e., the excess energy with respect to an equivalent mixture of phase-separated epitaxial GaP/GaAs and InP/GaAs free-surface slabs, as

$$\Delta E_{\mathrm{d}}(\Sigma) = E_{\mathrm{d}}(\Sigma) - (1 - x)E_{\mathrm{d}}(\mathrm{GaP}) - xE_{\mathrm{d}}(\mathrm{InP}). \tag{25}$$

The n_{CE} parameters $\{J_F\}$ of the cluster expansion (CE) are determined by projecting the set of $n_{\mathrm{d}}(\gg n_{\mathrm{CE}})$ directly calculated energies into the CE and minimizing the error

$$\sum_{\Sigma} |H_{\mathrm{CE}}(\Sigma) - \Delta E_{\mathrm{d}}(\Sigma)|^2. \tag{26}$$

In the final step, these interaction energies $\{J_F\}$ are used in eq. (24) to study the $T \neq 0$ thermodynamics by means of the cluster-variation method. This parametrization of an extensive set of direct calculations showed that the on-site energies induced by surface reconstruction dominate other interactions, and are responsible for both the $\mathrm{CP_B}$ preference at $h = 3$ and the correct stacking relationship between $h = 0$ and $h = 4$.

The previous section showed how $T = 0$ surface energetics could drive selective ordering in the subsurface layers. This does not imply that ordering will persist at finite (i.e., growth) temperatures. To find out what happens at finite temperatures, one needs to incorporate entropy effects and consider "non ideal" structures, such as the *imperfectly ordered* CuPt and *imperfectly disordered* alloy. In addition to questions (a)–(d) posed and addressed in § 7.2.1, we now add (e): would the $\mathrm{CP_B}$ ordering survive growth temperatures? (f) Would ordering exist also in nonstoichiometric compositions, e.g., in $\mathrm{Ga_{1-x}In_xP}$ with $x \neq 0.5$? (g) Would the $\mathrm{CP_B}$ arrangement be stable with respect to partial Ga–In atomic swaps? Such a study was undertaken by Osorio et al. (1992a,b). They use their Ising Hamiltonian of eq. (24) fit to many total-energy calculations to find (i) the $T=0$ ground-state structures of this Hamiltonian and (ii) its $T > 0$ free energies $E - TS$. This is done by solving the configurational Hamiltonian using the cluster-variation method of Kikuchi (1974), thus including entropy effects and site correlations. Both ideal CP as well as partially ordered structures were considered.

Figure 41 shows the $\mathrm{CuPt_B}$ long-range order parameter η for the $\mathrm{Ga_{0.5}In_{0.5}P}$

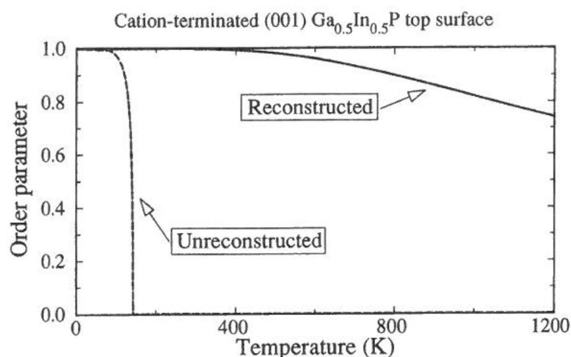

Fig. 41. Calculated temperature-dependence of the CuPt order parameter for a cation-terminated $Ga_{0.5}In_{0.5}P$ surface. From Osorio et al. (1992a).

cation-terminated surface, while fig. 42 shows the results for the $Ga_{0.7}In_{0.3}P$ surface. The main findings of this study are:

(i) As a consequence of reconstruction, the cation-terminated surface orders in the $CuPt_B$ structure and shows a gradual decrease in the degree of order with temperature, *with no phase transition* (fig. 41). We see that a thermodynamic model can account for the existence of ordering at $x = 0.5$ and that *a significant $CuPt_B$ order parameter persists up to* ~ 1500 K. This answers question (e). Note that in the *absence* of reconstruction, ordering disappears already at ~ 150 K (fig. 41). Furthermore, fig. 42 shows that CP_B ordering persists at growth temperatures even at other compositions, e.g., $Ga_{0.7}In_{0.3}P$. This is consistent with the hitherto surprising experimental findings by Kondow et al. (1989a) showing $CuPt_B$ ordering even for $x \neq \frac{1}{2}$. This answers question (f).

(ii) A study of the energies of intralayer atomic swaps shows a remarkable resilience of the two-dimensional $CuPt_B$ structures at the surface of cation-terminated alloys

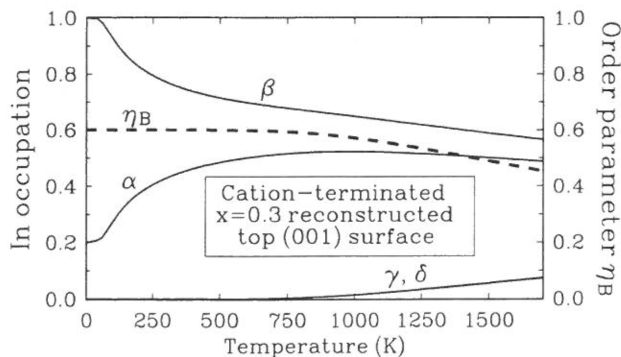

Fig. 42. Calculated temperature-dependence of the CuPt order parameter η_B (right axis) and the occupations by In atoms of the four cation sublattices α, β, γ, and δ (left axis) for off-stochiometric $Ga_{0.7}In_{0.3}P$. The value $\eta_B = 1$ corresponds to $C_\alpha = C_\beta = 1$ and $C_\gamma = C_\delta = 0$. From Osorio et al. (1992a).

and at the second cation subsurface layer of anion-terminated alloys. This answers question (g).

(iii) For the flat (i.e., no steps) surfaces studied here, the coupling between first-neighbor cation layers is very small, so that either of the two $CuPt_B$ subvariants is free to form, as observed. It is hence conceivable that the introduction of surface steps could decide the relative population of the two $CuPt_B$ subvariants ($(\bar{1}11)$ or $(1\bar{1}1)$).

7.4. *Dynamics of ordering*

We can now combine the insights gleaned from total-energy (§ 7.2) and phase-diagram (§ 7.3) calculations and describe how ordering might occur during growth. The results of these thermodynamic calculations described above can be summarized as follows:

(i) The *cation-terminated* surface shows a clear energetic preference for 2D CP_B at the free surface $h = 0$ and at $h = 4$. Furthermore, subsurface strains induced by surface reconstruction provide a natural mechanism for stacking the 2D layers of CP_B in the correct 3D arrangement ("phase locking"). The surface CP_B ordering is stable thermally even at growth temperatures. However, once covered by more than five layers, the thermodynamically stable ground state is not CP but chalcopyrite (figs. 5 and 9). The fact that the $CuPt_B$, not the chalcopyrite, structure is observed experimentally shows that atomic mobilities are too low in the interior of an epitaxial film to achieve bulk thermal equilibrium. It is at this point that we appeal to kinetic arguments, i.e., the finite rate of diffusion of atoms at the growing surface.

(ii) The *anion-terminated* surface shows no structural selectivity in the layer $h = 1$ just below the surface, however, it shows a clear preference for 2D CP_B at the third, $h = 3$ subsurface layer. Again, in deeper layers the stable structure is chalcopyrite, not CP_B. In addition, there is no energetic preference below the anion-terminated surface for correct 3D stacking of the 2D CP_B layers.

It is clear that in order to explain the occurrence of CP_B in *thick* alloy films (not just at the skin) one must assume that coverage must inhibit atomic diffusion, so that the surface-stable structure is frozen-in. We will distinguish therefore a number of possible scenarios:

(a) *Ordering models that require atomic mobilities only at the top surface.* Such models include (i) the cation-reconstruction model of BFZ (1991) and Osorio et al. (1992a,b) and (ii) the anion-reconstructed step model of Suzuki and Gomyo (1991, 1993), Suzuki et al. (1992), and Chen et al. (1991).

(b) *Ordering models that require atomic mobilities in a few subsurface layers.* This includes the anion-reconstruction models of BFZ (1991), Mahajan (1991), Mahajan and Philips (1991), and Philips et al. (1993), who independently extended the mechanism of LeGoues et al. (1990) to III–V materials.

(c) *Ordering models that involve exchange reactions between surface and subsurface layers.* This includes the anion-terminated step model of Bernard (1993).

In what follows we describe the essential features of these models, their strong points and weaknesses.

7.4.1. The top-surface cation-reconstruction model of ordering

This model of BFZ (1991) and Osorio et al. (1992a,b) supposes that the growing surface has cations exposed for a sufficiently long time so that reconstruction (and, hence, surface CP_B ordering) occurs. Suppose further that atomic diffusion is not sufficient to rearrange the state of order established at the surface after it is covered by new layers. The first cation layer is then CP_B; this is frozen-in by the next P layer. When a second layer is deposited, it will also order in the 2D CP_B structure (much like the first layer). The second layer is consistent with either the 3D $CuPt_B$ stacking or the $(GaP)_2(InP)_2$ superlattice stacking along $[1\bar{1}0]$ (denoted as "Y2" in table 5). The third cation-layer stacking (fig. 38) is the decisive factor in locking-in the 3D $CuPt_B$ structure. The $h = 4$ calculation of BFZ (1991) showed that the lowest-energy structure corresponds to the correct 3D $CuPt_B$ structure. *The* $h = 4$ *energies provide then an incentive for placing Ga at the top surface* ($h = 0$) *directly above In at the fourth subsurface layer* ($h = 4$), *as required for the correct stacking*. Note that the $h =$ 4 energies in fact can be changed by moving only surface atoms, placing In atoms and their upper dimers preferentially over the Ga rows of $h = 4$ (see fig. 40). Thus $h = 4$ energies can determine the stacking sequence. The energy difference of about 60 meV/surface atom that occurs between the two stacking possibilities of a CP_B surface structure (fig. 38) must be multiplied by the average number of atoms in a dimer chain before defects – mainly two neighboring upper dimers or two neighboring lower dimers – occur. This therefore stabilizes considerably the correct 3D $CuPt_B$ structure.

The viability of this model depends on the existence of stable cation-surface areas during growth. This question awaits experimental verification, as discussed in § 7.2. Its advantages are that no subsurface diffusion is required and that 3D phase-locking emerges naturally from the energetics. Ordering at finite temperatures (fig. 41), off-stoichiometric ordering (fig. 42), doping effects (fig. 32c), and absence of CuPt ordering in AlGaAs (table 7) are naturally explained.

7.4.2. The top-surface anion-reconstruction model of ordering

Although ordering appears on nominally flat surfaces, experiments on misoriented substrates (§ 6.5) show that a misorientation towards $[111]_B$ enhances the ordering while a misorientation towards $[111]_A$ reduces ordering. This prompted Suzuki and Gomyo (1991, 1993), Suzuki et al. (1992), and Chen et al. (1991) to introduce steps in their ordering mechanism. In what follows we discuss the way in which surface steps could decide the ratio of the two CP_B *sub*variants.

Figure 43a (Suzuki and Gomyo 1993) illustrates a particular 1 ML high step configuration with an anion dimer on the top terrace and a dangling bond at the bottom terrace. This model does not allow for "missing-dimer" configurations (Chadi 1987, Northrup and Froyen 1993). Furthermore, the model assumes *identical* surface steps. It is crucial in this model that (i) each terrace will have an even number of cations, so that long-range coherence will develop, and that (ii) the inequivalent anion sites t_1 and t_2 will have different chemical affinities toward bonding of Ga or In. The type of chemical selectivity at t_1 and t_2 is unclear, however. In 1991 Suzuki

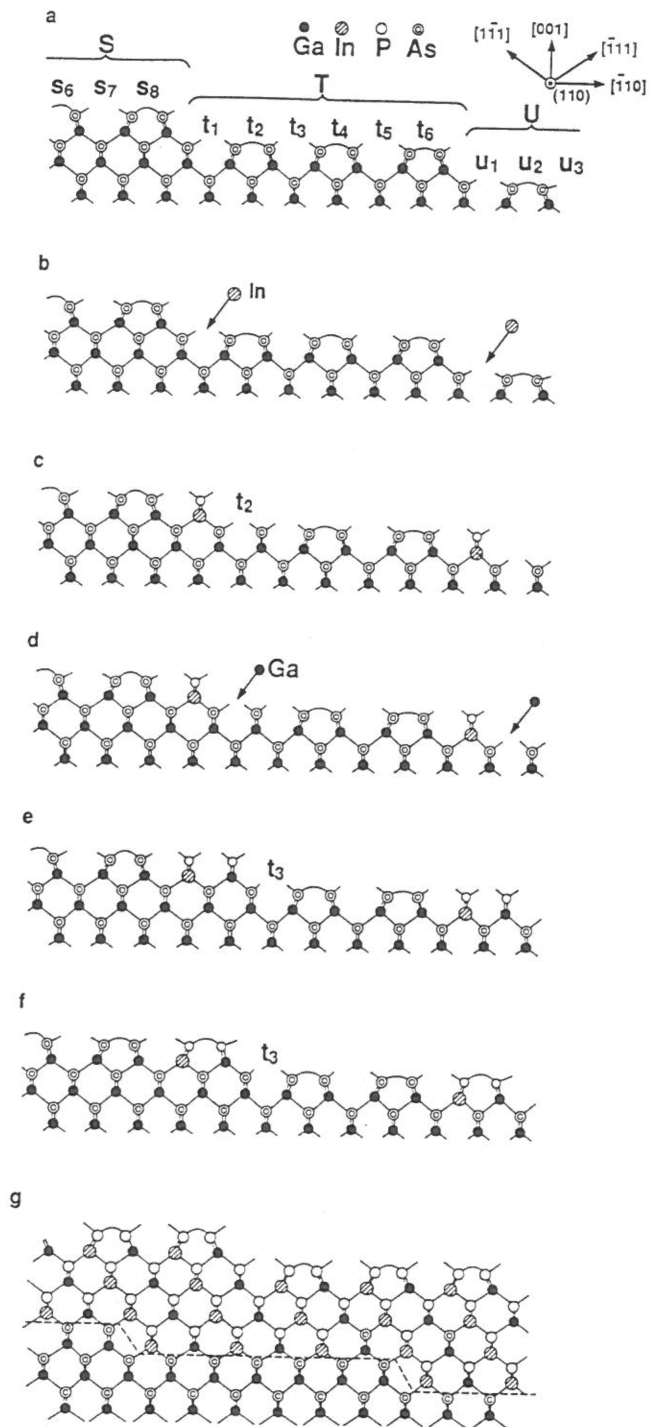

Fig. 43. Surface step ordering model of Suzuki and Gomyo (1993).

and Gomyo (1991) postulated the "step-terrace reconstruction model", in which site t_1 will selectively bind Ga (since the Ga–P or Ga–As bond is stronger in bulk than the In–P or In–As bond) while site t_2 will selectively bind In (since the In–P or In–As bond is longer than the Ga–P or Ga–As bond). Later on, Suzuki and Gomyo (1993) and Suzuki et al. (1992) criticized this "step-terrace reconstruction model" since upon its extention to growth of III–V–V alloys (e.g., GaPAs) the CP_A variants will be predicted, while the CP_B variants are actually observed. Furthermore, ordering which was observed to occur on a *disordered* $Ga_{0.5}In_{0.5}P$ substrate (Suzuki and Gomyo 1993) is not explained by this model. In 1992 they proposed (Suzuki et al. 1992, Suzuki and Gomyo 1993) that site t_1 will selectively bind In (despite the fact that this In–P or In–As bond is weaker than the Ga–P or Ga–As bond) while site t_2 will bind Ga. Figure 43 (Suzuki and Gomyo 1993) provides a detailed picture of the surface growth sequence: the In atom binds to t_1 and is then capped by P. This breaks the dimer bond next to it, making t_2 available to selectively bind Ga, which is then capped by P. The two P atoms on t_1 and t_2 will then dimerize making site t_3 (equivalent to t_1) available for In bonding, etc. This cycle is then repeated.

The advantages of this model are that it produces the correct CP_B variant and that it can be generalized to the III–V–V case, it explains why AlGaAs does not produce CP ordering (no site selectivity at t_1 versus t_2 for Al/Ga) and it requires atomic mobility only at the top surface. The model invokes, however, an unmotivated step-geometry whose stability remains, at present, unknown. Its serious problem is that it inevitably produces an In atom at $h = 3$ *under* the P–P dimer and a Ga atom *between* adjacent dimers (see part g of fig. 43). As discussed in § 7.2.3 (see item "$h = 3$" there and Bernard et al. (1991), Osorio et al. (1992a,b), and Froyen et al. (1992)) this configuration has an extremely high energy and is therefore unlikely to form even under "kinetic conditions". Indeed, the dimerization step in this model (part f or fig. 43) is unlikely to occur. This model, therefore, does not appear to be viable.

7.4.3. *The anion-reconstructed model of ordering with subsurface atomic rearrangements*

This scenario (Bernard et al. 1991) assumes anion termination and relies on the $h = 3$ selectivity predicted in the calculation of fig. 37. Here one assumes that the growing surface does not have cations exposed for a sufficient time needed to form CP_B at the surface, and that subsurface diffusion occurs at a substantial rate to the depth of $h = 3$ but becomes insignificant thereafter. Then, each mixed-cation layer, as it passes through the depth of $h = 3$ below the anion-terminated surface, would rearrange into a two-dimensional CP_B layer structure (fig. 31) as a result of the *dimerization* of the P-terminated surface, regardless of the state of order of the mixed-cation layer above it at $h = 1$ (X in fig. 37). The advantages of this model are: (i) It requires only the existence of anion dimers at the surface. This is granted by many surface-sensitive experiments. (ii) It naturally explains the absence of CP ordering in AlGaAs in terms of lack of site sensitivity at $h = 3$ due to the equal sizes of Al and Ga. (iii) It can explain the fact that ordering was observed to occur only in a "window" of temperatures. It is natural to assume in this scenario that if the

temperature is too low, then only layers $h = 0, 1$ are fluid, and ordering does not occur since $h = 1$ has but a small ordering selectivity. On the other hand, if the temperature is too high, even layers 4 and 5 are fluid, and again ordering does not occur, since these layers too have small structural selectivity (figs. 38 and 39). At intermediate temperatures, where diffusion penetrates to $h = 3$ (but no further), ordering is maximized because of the significant energetic preference for CP_B ordering there (fig. 37).

There are a few drawbacks to the model. *First,* in the absence of significant lifetimes for *cation*-terminated surfaces, Bernard et al. (1991) showed that this model fails to explain the three-dimensional CP_B layer-phasing that occurs at $h = 4$. One needs to look further for a layer-phasing mechanism that would be active with P-terminated surfaces. There are two possibilities for phase locking (both are speculative): (i) surface steps may exert influence through a choice of which pairs of rows of atoms dimerize (see § 7.4.4) or (ii) enhance the probability of formation of CP_B at $h = 1$ with fixed phase relative to the CP_B layer at $h = 3$. The latter would not require diffusion to $h = 3$, but only to $h = 1$ (or at steps). *Second,* this model requires complete diffusion of atoms at the third subsurface layer (~ 9 Å into the film) and that this diffusion stops abruptly at the fourth subsurface layer. This appears to be very artificial. Indeed, successful growth of thin quantum wells is often claimed. While their abruptness is not accurately determined, the occurrence of clear quantum confinement suggest that such wells do not exhibit any *strong* intermixing on the scale of $2 \times 9 = 18$ Å. This further argues against the assumption of complete atomic diffusion at $h = 3$.

A variation of the scenario above (Bernard et al. 1991) involves the assumption of a locally complete cation-terminated surface existing for a time too short for surface diffusion to create much CP_B ordering at $h = 0$, but long enough for the reconstruction of that surface to take place. Assume further that there is a gradual falloff of subsurface diffusion with increasing depth into the film, rather than a relatively abrupt falloff for $h > 3$. Then, when the only slightly ordered surface is buried to a depth of $h = 3$, the CP_B ordering will be enhanced by the (somewhat limited) subsurface diffusion. At this level, the initially small degree of ordering will select a surface P–P dimerization pattern that will, in turn, enhance the existing CP_B order at the expense of the other variant. When this layer passes to $h = 4$, it will dictate the pattern of cation-surface reconstruction such that the small degree of CP_B order achieved there will have the correct phase with respect to the $h = 4$ layer, so that true three-dimensional CP_B ordering results, although the imperfections due to rapid coverage of the cations at $h = 0$ and the limited subsurface diffusion at $h = 3$ would be substantial.

7.4.4. *The step-induced exchange model of ordering*

This is a modification of the anion-reconstructed model of ordering with rearrangements (§ 7.4.3). It introduces exchange reactions at steps to explain 3D phase-locking and substrate-tilting effects.

The step models of Suzuki and Gomyo (1992, 1993) and Chen et al. (1991) required

that the anion sites t_1 and t_2 exhibit different chemical affinities to Ga or In. The exchange model (Bernard 1993) assumes the same step geometry as in fig. 43 (see top part of fig. 44), or the alternative geometry in the bottom part of fig. 44. However, instead of invoking a selectivity of sites t_1 and t_2, this model grants the possibility that these sites could accept *any* atom. However, once occupied, these sites (labeled 3 and 4 in fig. 44) will exchange with the atoms labeled 5 and 6 at $h = 3$, so that the site *under* the P–P dimer (site 5) will be occupied by Ga, whereas that *between* P–P dimers (site 6) will be occupied by In. This exchange reaction takes place only while the step is flowing over these sites (i.e., at the kink where growth takes place). Once the step has moved away, further interchange takes place only rarely, if at all. Thus, the atoms in rows labeled 1 and 2, having been ordered when the step passed over them, remain ordered as the growth proceeds. It is easy to see from fig. 44 that previous growth on the lower terrace has ordered the atoms in, e.g., the rows labeled 7(In), 8(Ga), and 9(In) and that the step assures that the next layer (e.g., rows 1, 2, 5, and 6) has a fixed phase with respect to the lower layer. For the step configuration shown at the top of fig. 44 this results in stacking along a direction upward and to the right, $[1\bar{1}1]$, whereas for the step configuration of the bottom part of fig. 44 the stacking direction is along a direction upward and to the left, $[\bar{1}11]$. The model then predicts that as the substrate orientation changes so does the ratio between the

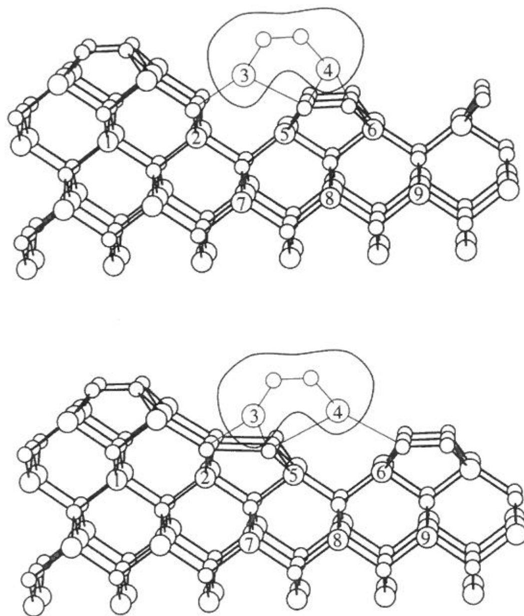

Fig. 44. Two step configurations used to discuss the surface exchange mechanism of ordering. Small circles denote P atoms and large circles denote Ga or In atoms. The subsurface strain induced by the dimers at the surface is such that the cation row below the dimer row is under compression (favoring occupation by Ga, e.g., site 5) and the adjacent row is under tension (favoring occupation by In, e.g., site 6). The labeled bubbles and atoms are discussed in the text.

different CP_B *sub*variants. Since the interval between the steps of the same kind necessarily contains an even number of cation rows, there is automatically long-range coherence between subvariants generated at nearby steps. Thus, for nominally flat surfaces, the model predicts less long-range coherence (smaller subvariant domains) than for surfaces tilted toward $[1\bar{1}0]$ or $[\bar{1}10]$, for each of which a particular subvariant will dominate and is expected to exhibit larger domain size.

To see that the mechanism works also for mixed-anion systems, simply consider the argument of Bernard et al. (1991) (see fig. 35 here) that for these systems the tight surface dimers induce subsurface strains that favor 2D ordering in the $h=2$ layer, again with the small atoms in the rows beneath the dimer rows and the large atoms in the alternate rows. Step phase-locking of ordered layers occurs in exactly the same way at $h=2$ as at $h=3$, as can easily be seen by examining fig. 44 and considering events at $h=2$.

We see that this model does not suffer from the problems of the previous step models (§ 4.2) (need to invoke selectivity at t_1 and t_2 and the occurrence of an unfavorable $h=2$ geometry); that it does not require a cation surface (unlike the model of § 7.4.1), nor does it require diffusion at $h=3$ with a cutoff at $h=4$ (unlike the model of § 7.4.3) except for an $h=1$ with $h=3$ exchange *just next to a step*. This model provides a mechanism for 3D phase-locking, makes specific predictions about the ordered subvariants generated by each possible step, has a mechanism for long-range coherence of a particular subvariant, generates the correct CP_B subvariants both for mixed-anion and mixed-cation films, and is consistent with ordering on a random alloy substrate.

There is some independent circumstantial evidence that such exchange reactions *could* occur during growth:

(i) An attempt to deliberately grow (001) $(GaP)_1/(InP)_1$ superlattices by ALE (McDermott et al. 1990) resulted instead in growth of the (111) $(GaP)_1/(InP)_1$ CuPt-structure on the (001) substrate. For this to happen in a shutter-controlled experiment (i.e., sequential exposure to GaP, then InP), some atomic exchange must occur during growth.

(ii) Suzuki and Gomyo (1993) showed that CP_B ordered $GaInP_2$ grows not only on a GaAs substrate but also on a substrate made of a random alloy, e.g., $Ga_{0.5}In_{0.5}P$. In this case a clear selectivity of the incoming atoms toward sites t_1 and t_2 (fig. 43) is difficult to envision since the sites under t_1 and t_2 are randomly occupied by different group-III substrate atoms. An exchange reaction leading to ordering is then a natural explanation. Also, a steric effect at t_1 ($\approx 15\%$ greater space than for an unreconstructed surface) seems possible (Suzuki et al. 1993).

(iii) Exchange reactions of Al with subsurface atoms on a GaAs substrate are well-documented in MBE growth (Huijser et al. 1981, Landgren and Ludeke 1981, Bachrach et al. 1981, Duke et al. 1981).

(iv) Lateral phase separation in AlAs/GaAs superlattices (Tsuchiya et al. 1989, Fukui and Saito 1987, Gaines et al. 1988) are explainable (Krishnamurthy et al. 1993) by exchange reactions.

8. Influence of phase separation and atomic ordering on electronic and optical properties

8.1. Observations of phase-separation effects on transport and optical properties

A decrease in carrier mobility has been reported for all compositions showing phase separation with no ordering (Cherng et al. 1986a, Greene et al. 1979, Kuphal and Pöcker 1982, Kuphal 1984, Quillec et al. 1983, Benchimol et al. 1983, Bhattacharya and Ku 1985, McDevitt 1990). The detailed study by Kuphal (1984) reports a dip in electron mobility of (001) InGaAsP layers grown at 630°C, whereas this is not observed in the layer deposited at 740°C. Using Hall effect measurements, Bhattacharya and Ku (1985) and Hong et al. (1987) have measured carrier mobility as a function of temperature in InGaAsP and InAlAs epitaxial layers. For the layers deposited at low temperatures, the mobility is low throughout the temperature range investigated, 50–600 K, and increases at temperatures above 400 K.

The above observations may be interpreted in terms of the model proposed by Blood and Grassie (1984). They envisage that due to the occurrence of phase separation mini-heterobarriers develop between microscopic domains differing in composition. Since interfaces between the composition-modulation domains are graded, the spatial variation of the conduction-band minimum E_C will have peaks and troughs, with the troughs separated by the saddle regions between the peaks of height ΔE_S. When $kT \gg \Delta E_S$, the electrons will be occupying energy levels close to E_C, with peaks in the E_C sheet protruding above this sea. These protrusions will contribute to alloy scattering at these temperatures. As the temperature is lowered, current transport in the saddle regions will have a significant effect on the carrier mobility. Internal emission of carriers over the saddle region will make the dominant contribution to the current. At low temperatures, thermal emission over the higher saddle regions will become less probable, leading to lower mobility. Furthermore, at higher growth temperatures, the composition difference between phase-separated regions is smaller, implying a smaller value of ΔE_S. As a result, the effect of phase separation on mobility is reduced.

Photoluminescence (PL) measurements on phase-separated layers have produced conflicting results. Most investigators have reported broadening of near-band-gap PL peaks for layers whose compositions lie within the miscibility gap (Cherng et al. 1986a,b, Chiu et al. 1985, Mukai 1983, Shirakata et al. 1986). The typical full width at half maximum is in the 15–25 meV range, but can be as much as 100 meV for immiscible systems such as InPSb (Reihlen et al. 1990). Several studies, however, show PL peaks in InGaAsP as narrow as 3–5 meV (Tsang et al. 1987, Goetz et al. 1983), a value close to the theoretical limit for a layer in which atomic constituents are distributed at random (Schubert and Tsong 1986). In both cases the width is much smaller than the offset between the conduction band edges discussed above. It is difficult to develop a coherent explanation for these conflicting results.

To our knowledge, there are no experimental studies on the effects of local clustering or phase separation on the optical band gaps. Theoretical studies of Mader and Zunger (1993) indicate that local clustering-type SRO in alloys such as

$Ga_{0.5}In_{0.5}P$ or $Ga_{0.5}Al_{0.5}As$ *reduces* the direct band gap relative to random solid solutions. In both cases the wavefunction at the conduction-band minimum is localized on the Ga sublattice, which acts therefore as a quantum well (this is at first surprising, since one might expect the smaller-gap InP to form the well. However, as shown in § 8.3.1 and fig. 51 below, actually Ga, not In, constitutes the CBM wavefunction). The clustering-induced band-gap reduction can be substantial, and unlike the ordering-induced band-gap reduction (see § 8.3) is *not* accompanied by a crystal-field splitting of the valence-band maximum. Clearly, more experimental and theoretical research is needed on the effects of SRO on band gaps.

8.2. *Observations of long-range atomic-ordering effects on transport*

The available results on the influence of ordering on carrier mobility can be divided into two groups: (i) observations where the occurrence of atomic ordering has reduced mobility (Friedman et al. 1991a,b, Lee et al. 1991, Horng and Lee 1992) and (ii) observations where ordering has produced higher mobility (A. Chin et al. 1991, Ueda and Nakata 1992). Both Friedman et al. and Lee et al. have done mobility measurements on (001) GaInP layers grown by OMVPE. These layers are *partially* ordered showing different CP subvariants. Indeed, growth on (001) substrates produces domains with various degrees of order. Shahid and Mahajan (1988) and Mahajan et al. (1989) have also examined similar films and shown that atomic ordering coexists in them with phase separation. Consequently, mobility can be lowered both by recombination and scattering at the domain boundary between regions with different degrees of LRO and by the presence of phase separation. Comparing the observed mobilities of samples deposited at 600, 670, and 750°C (Friedman et al. 1991a,b), it is inferred that scattering from ordering domain boundaries affects the mobility strongly.

The InGaAs samples which show *enhanced* mobility were grown on (110) InP substrates (A. Chin et al. 1991, Ueda and Nakata 1992) by MBE and OMVPE. As shown by Chin et al. and Ueda and Nakata, these layers have undergone CuAu-I-type ordering. Since only one variant of the ordered structure can form in this case, intervariant domain boundaries are absent in these layers. On the other hand, Ueda et al. (1989a) and McDevitt et al. (1992) have shown that OMVPE GaInP and LPE InGaAsP, grown on (110) substrates, contain some phase-separated regions. Assuming that similar results hold for (110) InGaAs layers, CuAu-I-type ordering may coexist with some phase separation. The fact that the mobility is *increased* in (110)-grown samples suggests therefore that scattering from phase-separated regions is unimportant, whereas atomic ordering leads to a reduced scattering relative to the random alloy, hence, enhanced mobility. We expect that growth of single subvariant samples (e.g., by substrate tilting or grooving) with large domains will result in high carrier mobilities.

8.3. *Observations of long-range atomic-ordering effects on optical properties*

Ordering leads to a number of distinct effects on the optical spectra:

(i) *Ordering-induced band-gap reduction:* many investigators (Gomyo et al. 1986, 1987, Kondow et al. 1988a,b, 1989a,b, Kondow and Minagawa 1989, Kurtz et al.

1989, 1990a, Nishino et al. 1988) observed a reduction in the band gap (the "band-gap anomaly") in ordered (001) GaInP and GaAlInP layers grown by OMVPE. This effect is illustrated in fig. 28 for $GaInP_2$ and in fig. 45 for $GaInAs_2$ (Arent et al. 1993). The band gap of the (disordered) layers grown by LPE remains invariant as a function of the growth temperature, whereas in the $GaInP_2$ layers grown by OMVPE it decreases first up to a growth temperature of 650°C and then increases again. This reflects the fact that the layer is strongly ordered at 650°C and the order parameter decreases on either side of this temperature. Also, the decrease in band gap may be enhanced further using atomic layer epitaxy (McDermott et al. 1991). Spatially resolved cathodoluminescense has recently been used to correlate the degree of order with the band-gap changes.

The effect of ordering-induced band-gap reduction is seen also in reflectivity (Alonso et al. 1993): fig. 46a shows the spectra of nearly disordered GaInP while fig. 46b shows the spectra of a highly ordered sample. Note how the peaks labeled E_{1c} and E_{2c} move to lower energy upon ordering. The same effect is seen in PLE (Horner et al. 1993): the disordered sample (fig. 47b) shows PLE at higher energies than the more ordered sample (fig. 47a).

(ii) *Ordering-induced valence-band splitting:* piezomodulated reflectivity (Alonso et al. 1993) shows that while a disordered sample has a single transition at threshold (fig. 46a), upon ordering this splits into two components (labeled E_{1c} and E_{2c} in fig. 46b). The same effect is seen in PLE and PL (Horner et al. 1993; see fig. 47). Similar results were obtained in photoreflectance by Glembocki et al. (1992) and in PL by Kanata et al. (1992, 1993) and Mowbray et al. (1992). The E_1–E_2 splitting

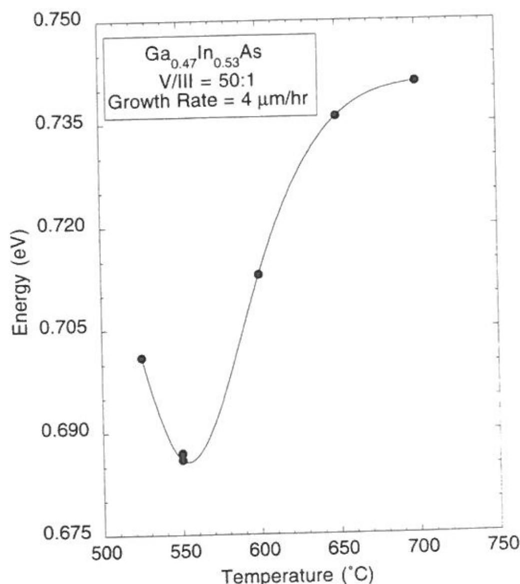

Fig. 45. Growth-temperature dependence of the band gap of $GaInAs_2$. From Arent et al. (1993).

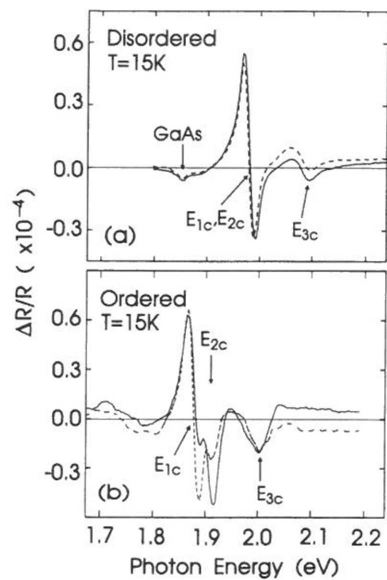

Fig. 46. Piezomodulated reflectivity spectra of (a) disordered and (b) ordered $GaInP_2$. The solid and dashed lines refer to the two polarization directions, see text. From Alonso et al. (1993a).

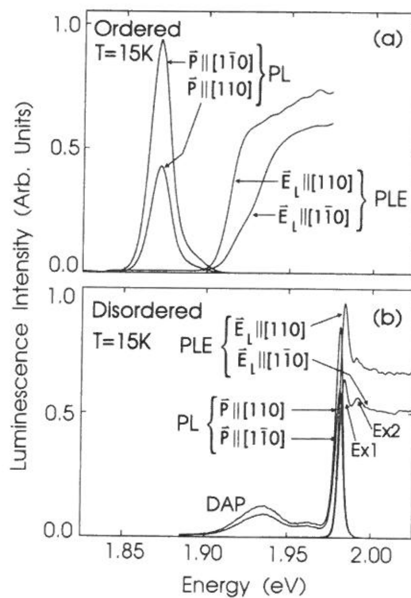

Fig. 47. PL and PLE of (a) ordered and (b) disordered $GaInP_2$. From Horner et al. (1993).

seen in reflectivity does not depend on temperature (Alonso et al. 1993) while the E_1–E_2 splitting observed in PL (Horner et al. 1994) increases with temperature, reflecting a Boltzmann population factor. That the E_1–E_2 splitting is correlated with ordering can be seen from fig. 48, which shows the [110] and [$1\bar{1}0$] PLE at 15 K for samples grown at different temperatures. We see that the samples with the largest band-gap reduction ($T_g \sim 670°C$) also show the largest splittings.

(iii) *Ordering-induced Stokes shift:* fig. 47a shows a significant red shift of the low-temperature PL relative to the PLE in the more ordered sample while in the disordered sample (fig. 47b) this shift is largely absent. Furthermore, in the ordered sample, the rising edge of the PLE is less steep than in the disordered sample.

(iv) *Disappearance of excitonic lines upon ordering:* the PLE spectra of the disordered sample in fig. 47b show distinct $n = 1$ and $n = 2$ excitonic features, labeled E_{X1} and E_{X2}, in the two polarizations. Their energies are 1.9833 and 1.9918 eV, respectively. The exciton binding energy is 11.3 meV. In the more ordered samples (fig. 47a) these features are smeared, thus unobserved. Indeed, Jones et al. (1992) and Schneider et al. (1992) observed *narrow* exciton lines (FWHM PL width of 4.3 meV) in disordered GaInP, while the ordered samples had a width of about 20 meV. The width *increases* with magnetic field for the disordered sample while it *decreases* for the ordered sample.

(v) *Intensity-dependent PL emission:* while disordered samples show a weak dependence of the PL peak on the laser intensity, partially ordered samples exhibit an emission that moves with increasing laser intensity (DeLong 1990, 1991).

The above observation can be interpreted *phenomenologically* by assuming that (a) ordering splits the valence-band maximum (VBM) into two components denoted E_1 and E_2, (b) ordering reduces the band gap in proportion to the *degree* of ordering, and (c) currently available ordered samples exhibit domains with different degrees of LRO. The more ordered domains have a lower gap than the less ordered domains, and (d) disordered samples exhibit a single domain, with a larger band gap.

The next section will discuss the physical basis for these, as yet phenomenological, assumptions. Here we first note that they are consistent with experiment as follows:

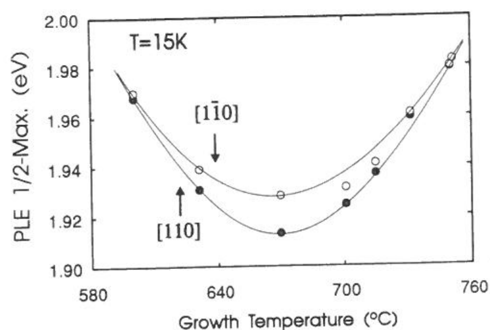

Fig. 48. Dependence of the PLE gap at two polarizations on the $GaInP_2$ growth temperature. Observe that at ~670°C the band-gap lowering and valence-band splitting are maximal. From Horner et al. (1994).

Low-temperature PL occurs predominantly from the domains with lower gaps (i.e., higher order parameter η_{high}). In contrast, PLE and reflectivity measurements produce *absorption* events, so the dominant contributions will come from the *most abundant domains*, i.e., those with the "average" degree or order η_{av}. Since $E_g(\eta_{\text{high}}) < E_g(\eta_{\text{av}})$, there is a large PL versus PLE Stokes shift in the ordered sample (fig. 47a) relative to the disordered sample (fig. 47b). Furthermore, the existence of a *distribution* of domains with different band gaps leads to a smeared absorption edge in the ordered sample (fig. 47a) relative to the disordered sample (fig. 47b) which shows a sharper PLE edge. If a perfectly ordered sample could be grown, we expect a strongly red-shifted PL and PLE, a narrowing of their signatures, and a reduced Stokes shift.

We note that it is unlikely that conventional growth of partially ordered samples will produce ordered domains embedded in a disordered matrix as suggested by DeLong et al. (1990). In such a case, one would expect spectroscopic signatures from *both* ordered and disordered domains. This is absent in regular MOCVD samples and exists only in samples *designed* to have two domains (Su et al. 1993). The results discussed above are consistent with a *distribution of partially ordered domains* each having its own η. The nonlinear dependence of the PL peak position on the laser intensity (DeLong 1990) is also consistent with the existence of differently absorbing domains. This anomaly disappears in single-domain samples and in the disordered alloy. Furthermore, this distribution could cover or smear the exciton lines, which are therefore too broad to be resolved in most ordered samples (fig. 47). Single-domain ordered samples should exhibit narrow excitonic lines.

We conclude that nominally ordered samples grown to date appear to exhibit a distribution of ordered domains. One of the challenges in this field is to control the growth parameters so that large, single domains will be achieved.

A general theory of ordering-induced changes in optical properties was developed by Wei and Zunger (1988b, 1989, 1990, 1993), Bernard et al. (1987), Wei et al. (1993), and Laks et al. (1992). We will first explain (§ 8.3.1) why *ideal* CuPt long-range order *reduces* the band gap and leads to a splitting of the valence band. We will then (§ 8.3.2) explain how optical properties are affected by *partial* ordering, correlating quantitatively the measured data with theory. This will enable us to deduce the degree of order from optical measurements.

8.3.1. Theory of optical effects in ideal CuPt structures

General arguments of quantum confinement suggest that the formation of an ordered superstructure is associated with an increase in the band gap due to the increased kinetic energy of the confined particles. We first explain how the existence of inter-valley coupling (or more generally, the dominance of potential-energy over kinetic-energy effects) reverses this trend in short-period superlattices such as the CuPt or CuAu structures.

To illustrate the generic relationships between the electronic structure of an ordered $(AC)_p(BC)_q$ compound and its isovalent binary constituents AC and BC, consider first the Γ and X conduction states Γ_{1c} and X_{1c} of the zinc-blende compounds AC

and BC (fig. 49, where C is assumed to be here the common cation). The average $(1-x)\varepsilon_{AC} + x\varepsilon_{BC}$ of the corresponding energies in the binaries is denoted in fig. 49 as $\langle\Gamma_{1c}\rangle$ and $\langle X_{1c}\rangle$. In a superlattice, these states exhibit "folding". It is instructive, therefore, to classify the electronic states of the superlattice (denoted by an overbar) according to the band index (m) and the wavevector $\boldsymbol{k}$ states of the binary constituents folded into the smaller Brillouin zone of the ordered system. Table 8 gives these folding relationships for the CA, CH, and CP structures depicted in fig. 1. Note from table 8 that the representations of the folded states are generally different for common-anion and common-cation superlattices. Note further that in the CuAu-I structure, which is an (001) superlattice, X folds to $\bar{\Gamma}$, while in the CuPt structure which is a (111) superlattice L folds to $\bar{\Gamma}$.

Conventional (i.e., purely kinetic-energy) theories proceed at this point by describing how the superlattice states in table 8 are displaced by quantum confinement effects. Note, however, that table 8 shows that states of *different symmetries* in the binary zinc-blende constituents can fold into states of the *same symmetry* in the ordered structure. In the particular example of common-cation CuAu-I-like ordering illustrated in the center column in fig. 49, we see two $\bar{\Gamma}_1$-folded states: $\bar{\Gamma}_{1c}(\Gamma_{1c})$ and $\bar{\Gamma}_{1c}(X_{1c})$. In the CuPt case, table 8 and fig. 50 show that the zinc-blende states Γ_{1c}

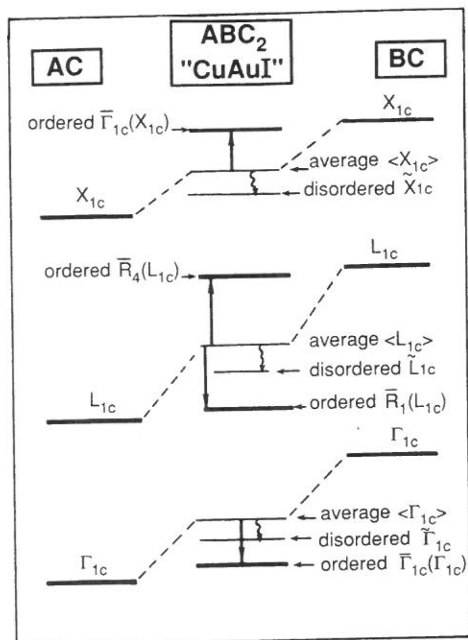

Fig. 49. Energy-level diagram showing how the energy levels of the (001) CuAu superlattice at $\bar{\Gamma}$ evolve from the energy levels of the binary constituents AC and BC. Here, Γ_{1c}, L_{1c}, and X_{1c} denote states in the constituents, $\langle\Gamma_{1c}\rangle$, $\langle L_{1c}\rangle$, and $\langle X_{1c}\rangle$ denote the average energy of the corresponding states of the deformed constituents, and $\tilde{\Gamma}_{1c}$, $\tilde{L}_{1c}$, and $\tilde{X}_{1c}$ denote the states of the *random* alloy. Arrows show how the "average" states repel once they are folded. Note that this repulsion lowers the CBM at Γ_{1c} thus contributing to band-gap reduction.

Table 8
Folding relations for CuAu, chalcopyrite, and CuPt structures. (From Wei and Zunger 1989.)

ZB	ABC_2, CuAu		ZB	Chalcopyrite ABC_2		ZB	CuPt ABC_2	
	Common anion	Common cation		Common anion	Common cation		Common anion	Common cation
Γ_1	$\bar{\Gamma}_1$	$\bar{\Gamma}_1$	Γ_1	$\bar{\Gamma}_1$	$\bar{\Gamma}_1$	Γ_1	$\bar{\Gamma}_1$	$\bar{\Gamma}_1$
Γ_{15}	$\bar{\Gamma}_5+\bar{\Gamma}_4$	$\bar{\Gamma}_5+\bar{\Gamma}_4$	Γ_{15}	$\bar{\Gamma}_4+\bar{\Gamma}_5$	$\bar{\Gamma}_4+\bar{\Gamma}_5$	Γ_{15}	$\bar{\Gamma}_1+\bar{\Gamma}_3$	$\bar{\Gamma}_1+\bar{\Gamma}_3$
X_1	$\bar{\Gamma}_4$	$\bar{\Gamma}_1$	X_1	$\bar{\Gamma}_2$	$\bar{\Gamma}_3$	L_1	$\bar{\Gamma}_1$	$\bar{\Gamma}_1$
X_3	$\bar{\Gamma}_1$	$\bar{\Gamma}_4$	X_3	$\bar{\Gamma}_3$	$\bar{\Gamma}_2$	L_3	$\bar{\Gamma}_3$	$\bar{\Gamma}_3$
X_5	$\bar{\Gamma}_5$	$\bar{\Gamma}_5$	X_5	$\bar{\Gamma}_5$	$\bar{\Gamma}_5$			
			W_1	$\bar{\Gamma}_5$	$\bar{\Gamma}_1+\bar{\Gamma}_3$			
			W_2	$\bar{\Gamma}_5$	$\bar{\Gamma}_2+\bar{\Gamma}_4$			
			W_3	$\bar{\Gamma}_1+\bar{\Gamma}_3$	$\bar{\Gamma}_5$			
			W_4	$\bar{\Gamma}_2+\bar{\Gamma}_4$	$\bar{\Gamma}_5$			

and L_{1c} give rise in the superlattice to the two equal-symmetry states $\bar{\Gamma}_1(\Gamma_{1c})$ and $\bar{\Gamma}_1(L_{1c})$. These are illustrated in fig. 50. We know from perturbation theory that states of the same symmetry repel one another in the presence of a perturbing potential: in the ordered structure, there exists an "ordering potential perturbation" $\Delta V(r)$ distinguishing energy levels of the ternary system from the average energy levels of the binaries. This potential does not have the zinc-blende symmetry, but belongs instead to the totally symmetric representation of the space group of the *ternary* structure. In general, $\Delta V(r)$ has an electronic piece, contributed by the electronegativity difference between the alloyed atoms A and B, and a structural piece, due to

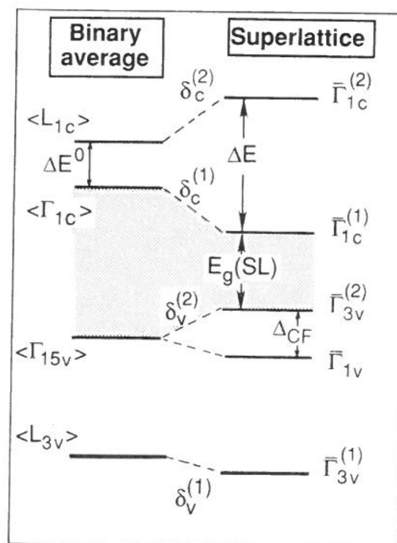

Fig. 50. Analogous to fig. 49, but for the (111)-oriented CuPt structure. Here $\delta_v^{(2)}$ is the up-shift of the VMB and $\delta_c^{(1)}$ is the down-shift of the CBM. The total band-gap reduction is $\delta_v^{(2)}+\delta_c^{(1)}$.

possible atomic displacements in the ternary phase relative to ideal zinc-blende positions. This "ordering potential" $\Delta V(r)$ can couple the zinc-blende states $|\gamma_i, m, \boldsymbol{k}\rangle$ and $|\gamma_j, m', \boldsymbol{k}'\rangle$ if they fold in the superlattice into states belonging to the same representation $\bar{\gamma}$. Using perturbation theory, the energy shift due to the coupling of the zinc-blende states $|\gamma_2, \boldsymbol{k}\rangle$ and $|\gamma_j, \boldsymbol{k}'\rangle$ folded into states of the same symmetry $\bar{\gamma}$ in the ternary phase (at wavevector $\boldsymbol{K}$) is

$$\delta E(\bar{\gamma}, \boldsymbol{K}) = \pm \frac{|\langle \gamma_i, m, \boldsymbol{k}|\Delta V(r)|\gamma_j, m', \boldsymbol{k}'\rangle|^2}{\varepsilon_m(\boldsymbol{k}) - \varepsilon_{m'}(\boldsymbol{k}')}. \tag{27}$$

This repulsion is indicated schematically in fig. 49 for the $\{\bar{\Gamma}_{1c}(\Gamma_{1c}); \bar{\Gamma}_{1c}(X_{1c})\}$ pair by the solid vertical arrows. We see that $\bar{\Gamma}_{1c}(\Gamma_{1c})$ is repelled downwards, while $\bar{\Gamma}_{1c}(X_{1c})$ is repelled upwards. If $\bar{\Gamma}_{1c}(\Gamma_{1c})$ is the conduction-band minimum, this effect will lead to a *reduction* in the band gap.

Figure 50 shows the situation in the CuPt structure. Here the average energy states $\langle L_{1c}\rangle$ and $\langle \Gamma_{1c}\rangle$ of the binary constituents fold in CuPt into $\bar{\Gamma}^{(1)}_{1c} = \bar{\Gamma}_{1c}(\Gamma_{1c})$ and $\bar{\Gamma}^{(2)}_{1c} = \Gamma_{1c}(L_{1c})$. According to eq. (27), the lowest state is repelled downwards by a quantity denoted in fig. 50 by $\delta^{(1)}_{c}$. This contributes again to the band-gap *reduction.*

This simple analysis points to a number of important features:

(i) Significant level repulsion can be expected between those states for which the energy denominator of eq. (27) is small. In GaSb–GaAs the energy denominator is smaller for the CuPt-folded states $\{\bar{\Gamma}_{1c}(\Gamma_{1c}); \bar{\Gamma}_{1c}(L_{1c})\}$ than for the CuAu-I-folded states $\{\bar{\Gamma}_{1c}(\Gamma_{1c}); \bar{\Gamma}_{1c}(X_{1c})\}$; therefore we will expect a larger band-gap reduction in the CuPt structure than in the CuAu structure. For the chalcopyrite structure one expects but a small level repulsion between the equal-symmetry folded states $\bar{\Gamma}_1(\Gamma)$ and $\bar{\Gamma}_1(W)$ (see table 8) since the Γ–W energy denominator near the band edge is rather large in the binary constituents.

(ii) Since the Γ_{1c} wavefunction is comprised of cation s + anion s orbitals, only folded states which have large s-character in the mixed sublattice can be expected to significantly couple to it. For a mixed-cation system, this is the case for X_{3c} (cation s and anion p state) and L_{1c} (mostly s-like state); for mixed-anion systems, this is the case for X_{1c} (cation p + anion s state) and L_{1c} states.

(iii) Level repulsion between $|\boldsymbol{k}\rangle$ and $|\boldsymbol{k}'\rangle$ can localize the wavefunction on different sublattices in the superlattice. The degree of this localization is strongly correlated with the energy shift δE of eq. (27). This repulsion-induced localization will have important effects on the spin–orbit splitting which depends primarily on the degree of wavefunction localization near a given atomic site. Repulsion-induced localization effects are depicted in fig. 51, showing the calculated squared wavefunction for the CuPt structure of $GaInP_2$ (Mader and Zunger 1993). We see that the $\bar{\Gamma}_{1c}(\Gamma_{1c})$ conduction-band minimum (upper figure) is localized on the Ga–P bond, while the next conduction band (lower figure) is localized on the In–P bond. Hence, contrary to naive expectations, the CBM in ordered $GaInP_2$ is localized on the large-gap component (GaP), not on the small-gap component (InP). This illustrates the effect of ordering on wavefunction localization.

The reduced symmetry in the ternary system relative to the binary zinc-blende

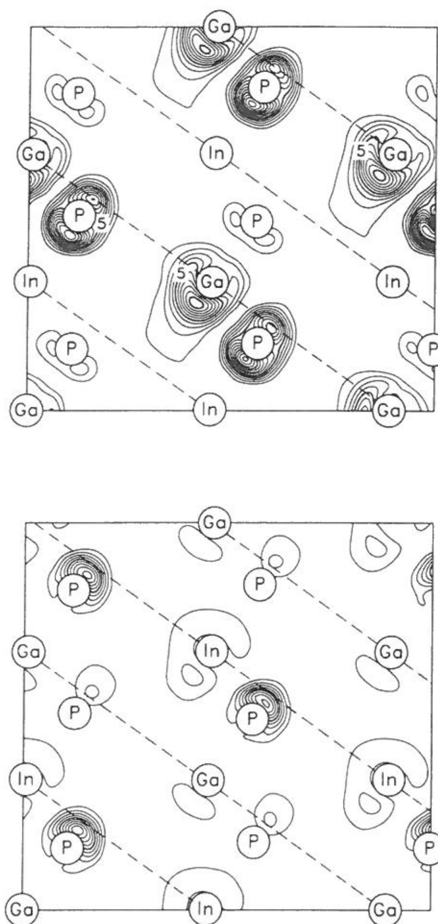

Fig. 51. Calculated squared wavefunction for the two lowest conduction bands in CuPt-like $GaInP_2$. Observe that the $\bar{\Gamma}_{1c}$ CBM (top figure) is localized on the Ga–P plane while the second conduction band (bottom figure) is localized on the In–P plane. Thus, contrary to simple intuition, the GaP region acts here as a quantum *well* (not barrier). From Mader and Zunger (1993).

constituents also splits the valence-band maximum: "heavy-hole" and "light-hole" states are now separated by the crystal-field splitting Δ_{CF} (fig. 50). Since the upper valence-band component moves to higher energies (by $\delta_v^{(2)}$ in fig. 50), this effect also contributes to the band-gap reduction. Hence, the total band-gap reduction upon ordering reflects a combination of conduction-band downward repulsion (due to intervalley coupling) with valence-band upward repulsion (due to crystal-field effects).

To calculate reliably the ordering-induced changes in the band gap, we avoid perturbation theory or effective-mass theory, and calculate instead the band structure of the ordered structures as if they were new compounds in their own right. We use the local-density formalism as implemented by the linear augmented plane wave

(LAPW) method (Wei and Zunger 1988b, 1990, Bernard et al. 1987). The energy of the random alloy is calculated by the method of Zunger et al. (1990).

Figure 52 summarizes the results of Wei and Zunger (1990) for the *direct* gaps of a range of alloys each calculated in a few ordered structures. The following conclusions are apparent:

(i) The calculated direct $\Gamma_{\mathrm{VBM}} \rightarrow \Gamma_{1c}$ band gaps generally increase in the sequence

$$E_{\mathrm{CP}} < E_{\mathrm{CA}} < E_{\mathrm{R}} < E_{\mathrm{CH}} < \bar{E}, \tag{28}$$

where $\bar{E}$ denotes the 50%–50% average of the direct gaps of the binary constituents (the only exceptions are $E_{\mathrm{CH}} \gtrsim \bar{E}$ for lattice matched $AlGaAs_2$ and $CdHgTe_2$).

(ii) The band-gap narrowing δ relative to the constituents

$$\delta = E_g(ABC_2) - \tfrac{1}{2}[E_g(AC) + E_g(BC)] \tag{29}$$

is generally small in the chalcopyrite structure but can be very large in the CuPt phase.

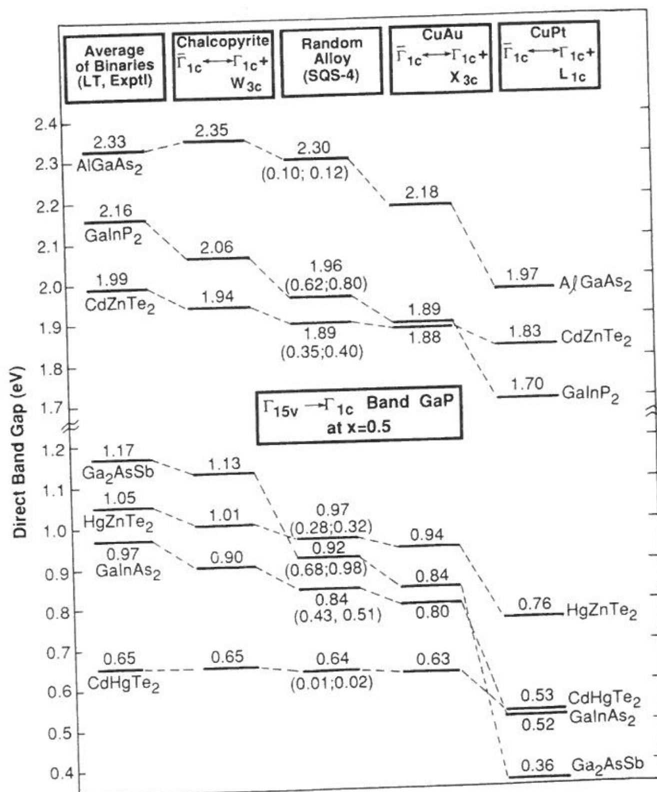

Fig. 52. Calculated direct band gaps of various 50%–50% ordered alloys of III–V and II–VI systems. The band gaps of the random alloy are cited here with respect to the crystal-field averaged VBM. To obtain the value with respect to the VBM (using $GaInP_2$ as an illustration) we calculate $1.96 + (0.80 - 0.62)/4 = 2.01$ eV. Hence, the band-gap reduction in the CuPt structure relative to the VBM of the random alloy is $1.70 - 2.01 = -0.31$ eV. From Wei and Zunger (1990).

(iii) In some cases δ_{CP} is so large that $AlGaAs_2$ (Wei and Zunger 1988b) and Ga_2PAs (Dandrea and Zunger 1990c, 1991) are predicted to become *direct-gap materials in this structure, despite the fact that the corresponding* 50%–50% *random alloys have indirect band gaps.* For Ga_2PAs, Dandrea and Zunger (1990c, 1991) predicted that both the CP and the CA structure will become direct-gap materials if grown coherently on a GaAs substrate. While the prediction for the CuPt structure awaits experimental verification, recent (artificial growth) of the CA structure of Ga_2PAs/GaAs (Takarohashi and Ozeki 1991) demonstrated a direct band gap, in agreement with this prediction.

(iv) The large variation of the band gaps ($\sim$0.81 eV for Ga_2AsSb) with the type of ordering highlights the possibility of tuning alloy band gaps at a *fixed* composition by selecting growth conditions that stabilize a particular structure. This could open interesting technological applications, e.g., making far-IR gaps from ordered In_2AsSb or $GaInSb_2$ (Wei and Zunger 1991). The variation is generally smaller for II–VI's than for III–V's.

(v) It is interesting to see in fig. 52 some cases of "band-gap crossings" for different systems in different structures, e.g., $GaInP_2$ has a larger gap than $CdZnTe_2$ both in the chalcopyrite structure and in the random alloy, yet the opposite is predicted to be true in the CuPt structure. Similarly, $CdHgTe_2$ has a smaller gap than Ga_2AsSb in the CH, CA, and in the random structure, yet in the CuPt structure Ga_2AsSb has a smaller gap than $CdHgTe_2$.

We can explain qualitatively the trends of fig. 52 in terms of the properties of the binary constituents using the discussion at the top of this section:

(i) The larger band-gap narrowing δ_{CP} in the CuPt-like structure relative to δ_{CA} in the CuAu-like structure reflects the smaller Γ_{1c}–L_{1c} energy denominator (appropriate to CP) relative to the Γ_{1c}–X_c energy denominator (appropriate to CA). The effect is considerably smaller in CH where the $\bar{\Gamma}$-folded W_c states are energetically far removed from Γ_{1c}, hence the coupling is weaker.

(ii) The "band crossings" noted above reflect the same effect: the calculated binary-averaged energy-denominator Γ_{1c}–L_{1c} in GaP–InP ($\sim$0.1 eV) is smaller than that in CdTe–ZnTe ($\sim$0.9 eV), hence, $\delta_{CP} = 0.45$ eV is larger in the former relative to the latter ($\delta_{CP} = 0.17$ eV) case.

(iii) Among size-matched alloys, $CdHgTe_2$ has a very small $\delta_{CP} = 0.12$ eV while $AlGaAs_2$ has a larger $\delta_{CP} = 0.36$ eV, reflecting again a larger energy denominator in the former case (1.3 eV) relative to the latter (0.4 eV).

(iv) $AlGaAs_2$ is predicted to have a larger band-gap narrowing upon ordering in the CuAu-like structure than $CdHgTe_2$, since the pertinent Γ_{1c}–X_{3c} denominator is larger in the latter case (2.4 eV) than in the former (0.8 eV).

(v) The larger crystal-field splitting at the VBM for CA and CP relative to CH is also explainable by noticing the larger energy difference Γ_{15v}–W_v in CH relative to Γ_{15v}–X_{5v} and Γ_{15v}–L_{3v} in CA and CP, respectively. (The coupling between Γ and X states in CH is very small due to the incompatible phase factor.)

(vi) Finally, the strong $\bar{\Gamma}_4(\Gamma_{15v})$–$\bar{\Gamma}_4(W_v)$ coupling relative to the $\bar{\Gamma}_5(\Gamma_{15v})$–$\bar{\Gamma}_5(X_{5v})$ coupling in the chalcopyrite structure can lead there to an *inverted* valence band

($\Delta_{CF} < 0$), whereby the $\bar{\Gamma}_{4v}$ is *above* the $\bar{\Gamma}_{5v}$. This is the case in Ga_2AsSb, $AlGaAs_2$, and $CdHgTe_2$ and in most real chalcopyrites.

To our knowledge, only in a few cases has nearly *perfect* monolayer ordering been achieved experimentally. In all cases, nearly perfect ordering occurs only when the structure is grown intentionally rather than spontaneously. We next review the experimental data on optical-induced band-gap changes in nearly perfectly ordered structures.

8.3.2. *Observations of band-gap changes in nearly perfectly ordered structures*

8.3.2.1. CA structure of $GaAlAs_2$. Ellipsometry measurements of the *direct* gap in $GaAlAs_2$ in the CA structure gave 2.08 eV at room temperature (Garriga et al. 1987), or ~2.18 eV when extrapolated to low temperatures. Low-temperature Raman scattering (Cardona et al. 1987) gave 2.15 eV. These values agree well with the prediction (fig. 52) of 2.18 eV. However, in the case of the *indirect* gap of the CA structure of $AlGaAs_2$, considerable controversy exists. Ge et al. (1991) determined conclusively from PL and PLE experiments that the lowest conduction band is the AlAs-derived X_{xy} state, while first-principles band calculations (Zhang et al. 1989, Bylander and Kleinman 1986) all agree that the CBM is the GaAs-derived L-folded state. This controversy was recently resolved (Laks and Zunger 1992) by performing calculations on the *imperfectly ordered* CA structure of $AlGaAs_2$. In the perfect CA structure successive bilayers along the (001) direction are either pure AlAs or pure GaAs. In the imperfectly ordered structure, some admixture of the opposite atomic type can occur. By calculating the band structure of CA $AlGaAs_2$ as a function of this interfacial roughness, Laks and Zunger (1992) showed that for *perfect ordering* the CBM is indeed the GaAs-derived L-like state (as noted by previous calculations, all assuming perfect ordering), but that for $\gtrsim 20\%$ *intermixing*, the CBM reverts to the AlAs-derived X_{xy} state (as seen experimentally). It hence appears that even the artificially grown CA structure is not sufficiently perfect to show the full spectroscopic fingerprints of ideal ordering. For example, Wei and Zunger (1988b) predicted that perfectly ordered $AlGaAs_2$ in the (111) CuPt structure will have a direct gap, yet the PL results of Cinagolani et al. (1990) shows that currently grown (111) AlAs/GaAs superlattices have an indirect gap. We suspect again interfacial roughness.

8.3.2.2. CA structure of $Ga_2PAs/GaAs$. The second example of relatively high-quality growth is the CA structure of $Ga_2PAs/GaAs$ (001) grown by Takarohashi and Ozeki (1991). Their measured band gap of 1.77 eV agrees remarkably well with the theoretical prediction (Dandrea and Zunger 1990c, 1991) of 1.77 eV. This experiment also confirmed that the CA structure has a direct band gap despite the fact that the 50%–50% alloy is indirect.

Our foregoing discussion clarifies the physical factors responsible for ordering-induced band-gap reduction, but also highlights the fact that currently produced samples do not exhibit perfect ordering. We next explain how the optical properties of *imperfectly ordered* samples depend on the degree of LRO. This will establish a spectroscopic method of assessing the degree of LRO in given samples.

8.3.3. Theory of the relation between optical properties and the degree of ordering

The spontaneous monolayer A/B alternation along the [111] direction observed in vapor-phase growth of virtually all III–V alloys is an example of the imperfect ordering: successive atomic layers along [111] are not pure A or pure B. We have seen (§ 6) that the degree of ordering depends on growth temperature, growth rates, III/V ratio, and doping. Electron diffraction does not provide a quantitative measure of LRO, and current theories do not relate the optical properties to the degree of LRO.

Laks et al. (1992) have recently introduced a general theoretical method for describing alloy properties as a function of the degree of LRO. They derived from this general theory a simplified formula that describes the properties of alloys with partial LRO in terms of the properties of (i) the perfectly random alloy (LRO parameter $\eta = 0$) and (ii) the ordered superlattice ($\eta = 1$). The result is simply

$$E_i(x, \eta) = E_i(x, 0) + \eta^2[E_i(X, 1) - E_i(X, 0)], \quad (30)$$

where X is the composition of the ordered phase and x is the alloy composition. Equation (30) involves two approximations: (i) while retaining all pair interactions contributing to E_i, it neglects three-body and higher contributions, and (ii) it represents any distribution of partially ordered domains and short-range order that may exist in actual samples by a single, sample-average LRO parameter. Approximation (i) was previously tested (Laks et al. 1992) by contrasting the predictions of eq. (30) with directly calculated energies, obtained in a simulation of large (~ 2000 atoms) supercells whose sites are occupied by A and B atoms in accordance with a given η value. Equation (30) produces excellent agreement with the direct simulation when both η and x are varied for E_i = elastic strain energies in GaP/InP, and E_i = superlattice band energies for AlAs/GaAs. Approximation (ii) will be tested, in part, by contrasting the predictions of eq. (30) with experiment. This can be done by comparing with eq. (30) the various measured optical transition energies in a given sample, as well as for different samples representing different degrees of order.

CuPt-like ordering splits the valence-band maximum (VBM) of cubic semiconductors into heavy-hole, light-hole, and split-off bands, denoted here $i = 1$, 2, and 3, respectively. Their energies can be described by the quasicubic model (Hopfield 1960, Wei and Zunger 1990, 1993)

$$E_1 = \tfrac{1}{3}(\Delta_0 + \Delta_{CF}),$$
$$E_{2,3} = -\tfrac{1}{6}(\Delta_0 + \Delta_{CF}) \pm \tfrac{1}{2}[(\Delta_0 + \Delta_{CF})^2 - \tfrac{8}{3}\Delta_0\Delta_{CF}]^{1/2}, \quad (31)$$

where Δ_0 is the spin–orbit splitting in a cubic field and Δ_{CF} is the crystal-field splitting in the absence of spin–orbit coupling. Applying eq. (30) to Δ_0 and Δ_{CF} for $x = X = \tfrac{1}{2}$ gives

$$\Delta_0(\eta) = \Delta_0(0) + \eta^2[\Delta_0(1) - \Delta_0(0)],$$
$$\Delta_{CF}(\eta) = \Delta_{CF}(0) + \eta^2[\Delta_{CF}(1) - \Delta_{CF}(0)]. \quad (32)$$

Note that since the random alloy is cubic, $\Delta_{CF}(0) = 0$, so $E_1 - E_2 = 0$ and $E_1 - E_3 = \Delta_0(0)$ for $\eta = 0$. For $\eta > 0$, spin–orbit and crystal-field effects are intermixed. The

band-gap reduction $\Delta E_g(\eta)$ relative to the *random* alloy can be further written according to eq. (30) as

$$\Delta E_g(\eta) = \Delta E_g(0) + \eta^2[\Delta E_g(1) - \Delta E_g(0)] = \eta^2 \Delta E_g(1), \tag{33}$$

where $\Delta E_g(0) \equiv 0$ by definition. Inserting eq. (32) into eq. (31) gives two valence-band splittings $E_1(\eta) - E_2(\eta)$ and $E_1(\eta) - E_3(\eta)$ expressed in terms of $\Delta_0(0)$, $\Delta_0(1)$, and $\Delta_{CF}(1)$, while eq. (33) gives the third quantity – $\Delta E_g(\eta)$, in terms of $\Delta E_g(1)$. All four quantities can be calculated from band theory.

Wei and Zunger (1990) have fitted their LAPW calculated relativistic VBM energy levels of perfectly CuPt-ordered alloys to eq. (31) and extracted thereby $\Delta_{CF}(1)$ and $\Delta_0(1)$ for the seven systems given in table 9. For comparison, we also show the values obtained by averaging over the binary constituents. The table shows that: (i) the difference between $\Delta_0(1)$ for the ordered structures and the value averaged over the binary constituents is small in common-anion systems: $\lesssim 0.01$ eV for III–V's and $\lesssim 0.04$ eV for II–VI's (the larger difference in II–VI's is probably due to the large mixing of d character into the VBM). (ii) The bowing of the spin–orbit splitting can be large and *negative* in common-cation systems. (iii) The crystal-field splitting is small and often negative for CH but generally large and positive in the CA and CP structures (for $GaInP_2$ it is even larger than Δ_0).

In general, the value of $\Delta_{CF}(1)$ depends on the assumed mode of lattice relaxation. Two extreme cases are possible: (a) assume that all atoms in the CP structure relax to their minimum-energy positions, as if the film was "free standing". In this "relaxed" case there is a *trigonal* distortion and $\Delta_{CF}(1)$ is large. (b) Assume that coherence with

Table 9

Calculated unrelaxed crystal-field splitting $\Delta_{CF}(1)$ and spin–orbit splitting $\Delta_0(1)$ (all in eV) at the VBM for seven 50%–50% semiconductor alloys. For comparison, we also give the calculated binary-averaged values. The small LDA correction (<0.03 eV for III–V and <0.10 eV for II–VI) for Δ_0 is not included in the binary-averaged value. The values $\Delta_0(1) = 1.05$ and $\Delta_{CF}(1) = 0.20$ of table 10 for CP $GaInP_2$ differ slightly from the values given here due to stricter LAPW convergence in table 10. From Wei and Zunger (1990).

System	Property	Binary average	CA	CH	CP
$GaInP_2$	Δ_{CF}	0	0.191	0.032	0.212
	Δ_0	0.107	0.114	0.108	0.118
Ga_2AsSb	Δ_{CF}	0	0.085	−0.013	0.230
	Δ_0	0.523	0.554	0.522	0.595
AlGaAs	Δ_{CF}	0	0.049	−0.007	0.028
	Δ_0	0.319	0.317	0.319	0.320
$ZnCdTe_2$	Δ_{CF}	0	0.127	0.020	0.099
	Δ_0	0.873	0.864	0.868	0.854
$ZnHgTe_2$	Δ_{CF}	0	0.231	0.002	0.257
	Δ_0	0.831	0.831	0.828	0.793
$CdHgTe_2$	Δ_{CF}	0	0.008	−0.004	0.020
	Δ_0	0.817	0.813	0.812	0.811
$GaInAs_2$	Δ_{CF}	0	0.134	0.020	0.121
	Δ_0	0.351	0.355	0.352	0.347

the (110) substrate inhibits trigonal deformation, so the system remains cubic. Table 10 (Wei et al. 1993) shows the results for $GaInP_2$ and $GaInAs_2$ corresponding to both cases. Unfortunately, at this time there are no X-ray diffraction experiments that can discern trigonal distortions.

The lines shown in fig. 53 depict the predictions of the theory of Wei et al. (1993) for $GaInP_2$ (fig. 53a) and $GaInAs_2$ (fig. 53b) assuming the two separate scenarios for relaxation. This theory can now be compared with experiments, e.g., by fitting the measured gap reduction in a given sample s to fig. 53, hence deducing the long-range order parameter η_s in this sample. Consistency can then be examined by using this η_s-value to predict the two valence-band splittings $E_1 - E_3$ and $E_1 - E_2$ from fig. 53 and comparing these with the measured splittings for this sample. If consistency is established, we have an LRO parameter η_s. This procedure can be repeated for many samples, grown at different temperatures, thus establishing the degree of LRO versus growth conditions.

Figure 53a shows the optical data of Glembocki et al. (1992) (photoreflectance), Kanata et al. (1992) (polarized PL), and Alonso et al. (1993b) (piezomodulated reflectivity) on many $GaInP_2$ samples. The agreement with theory is rather good. This establishes a spectroscopic method of inferring the degree of LRO in different samples.

The theory of eqs. (30)–(33) applies to cases where the only source of valence-band splitting and band-gap reduction is long-range ordering. We have seen, however, in § 8.1 (see Mader and Zunger 1993) that local clustering can reduce the band gap (without any valence-band splitting). Furthermore, if a film is coherent with a lattice-*mismatched* substrate (e.g., when the composition x in $Ga_xIn_{1-x}P$ deviates from the value that gives a match to GaAs), one can find a strain-induced valence-band splitting which is not caused by ordering. It is then natural to ask how one could distinguish (i) clustering-induced band-gap reduction from ordering-induced band-gap reduction, or (ii) strain-induced valence-band splitting from ordering-induced valence-band splitting. Of course, simultaneous measurements of clustering (e.g., via

Table 10

Calculated spin–orbit splitting (Δ_0) and crystal-field splitting (Δ_{CF}) for the perfectly ordered ($\eta = 1$) and perfectly random ($\eta = 0$) phase, and band-gap reduction (ΔE_g) of the ordered phase relative to the random alloy. Results (in eV) are given for two alloys. For $\Delta_{CF}(1)$ we give results calculated with and without rhombohedral relaxation. The Δ_0 and ΔE_g values are rather insensitive to the rhombohedral distortion. From Wei et al. (1993).

	$Ga_{0.5}In_{0.5}P$	$Ga_{0.5}In_{0.5}As$
$\Delta_0(0)$	0.100	0.35
$\Delta_0(1)$	0.105	0.35
$\Delta_{CF}(0)$	0.0	0.0
$\Delta_{CF}(1)_{unrel.}$	0.20	0.10
$\Delta_{CF}(1)_{rel.}$	0.31	0.18
ΔE_g	−0.32	−0.30

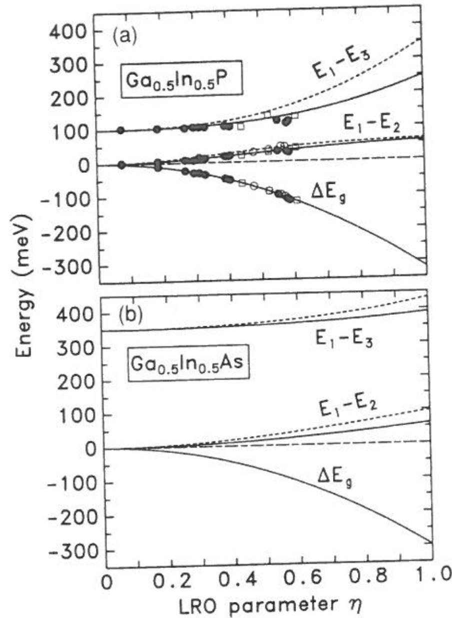

Fig. 53. (a) Theoretical predictions for the valence-band splittings $E_1 - E_2$ and $E_1 - E_3$ (see eqs. (31), (32)) and band-gap reduction relative to the random alloy ΔE_g (eq. (33)) are shown as lines. Solid lines: using the cubic value $\Delta_{CF}(1) = 0.20$ eV, dashed lines: using the equilibrium, trigonally deformed value $\Delta_{CF}(1) = 0.31$ eV. Points refer to measured values. Solid circles: data of Alonso et al. (1993b) taken at $T = 15$ K, open circles: Kanata et al. (1992) at $T = 13$ K, open squares: Glembocki et al. (1992) at $T = 298$ K. (b) Theoretical prediction for $Ga_{0.5}In_{0.5}As$. From Wei et al. (1993).

diffuse X-ray scattering) and LRO (via TED) will be very helpful. Another approach is suggested by eqs. (31)–(33) (Wei and Zunger 1993). By substituting eq. (32) in eq. (31) one obtains $E_1 - E_2$ in terms of η. Similarly, one can extract η from eq. (33) and substitute it in the expression for $E_1 - E_2$. This then gives a direct relationship between $E_1 - E_2$ and ΔE_g, *independent of* η. This is shown in fig. 54 for $GaInP_2$ using the data of Alonso et al. (1993b). The calculated lines for different compositions are from Wei and Zunger (1993). If the experimental points lie on this line, one could conclude that the valence-band splitting and the band-gap reduction share a common physical source: LRO. If the experimental points fall *below* the line, this means that there is a mechanism leading to band-gap reduction without a proportional increase in valence-band splitting. Phase separation is a plausible source of such a behavior. The data points of fig. 54 (Alonso et al. 1993b) point to this possibility for the two samples with the largest $|\Delta E_g|$. Finally, if points lie *above* the line, this means that there is a mechanism leading to valence-band splitting without a concomitant reduction in band gap. Substrate strain-induced splitting is a likely candidate for such a behavior, as seen in fig. 54 for $x \neq x_0$.

In a recent work, Wei and Zunger (1994) considered the effects of strain (produced by a lattice-mismatched film composition) on the optical properties of ordered

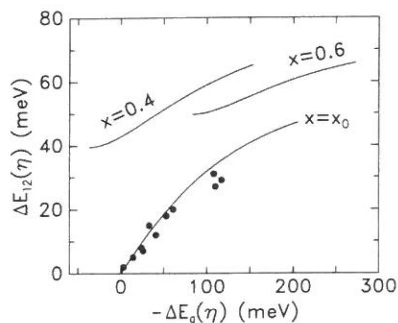

Fig. 54. The solid line depicts the theoretically predicted dependence of the $E_1 - E_2$ valence-band splitting in $GaInP_2$ on the band-gap reduction (Wei and Zunger 1993). Solid circles are the data of Alonso et al. (1993b). The deviation of the two experimental points at high ΔE_g from the theoretical line is suggestive of possible phase separation in these samples. Note that if the composition deviates from the lattice-matched value (x_0) all curves move up.

$GaInP_2$. For (001) strain and (111) ordering they find that (i) chemical ordering removes the "cusp" in the band gap versus strain curve of random alloys. (ii) Epitaxial strain always leads to an *increase* in the ordering-induced valence-band splitting ΔE_{12}. (iii) Chemical ordering *reduces* the slope of ΔE_{12} versus strain. (iv) In the case of strain the *intensities* of the transitions between the split components of the valence-band and the conduction-band minimum are the same for [110] and [1$\bar{1}$0] polarization, while if the splitting is caused by ordering the intensities depend on polarization. (v) Ordering can significantly enhance the *spin*-polarization: a 100% polarization is predicted for single-subvariant $GaInP_2$ if photoelectrons are collected from the highest valence band.

The optical data surveyed above correspond to the fundamental absorption edge around 1.7–2.1 eV. However, Nishino et al. (1988) and Inoue et al. (1988) observed in electroreflectance of partially ordered $GaInP_2$ also the E_1 (3.25 eV) and $E_1 + \Delta_1$ (3.40 eV) transitions, which are slightly downshifted relative to the values 3.28 and 3.47 eV, respectively, found in disordered LPE material. In addition they find in the partially ordered materials two additional very weak transitions at ~2.2 (transition A) and ~2.4 eV (transition B). The origin of these transitions is not clear. The predicted (Wei and Zunger 1993) transitions in perfectly ordered CuPt between the light-hole and heavy-hole to the folded L_{1c} state occur at 2.30 and 2.40 eV. On the other hand, the random alloy also has (indirect) transitions in this energy range. At present, it seems difficult to unambiguously identify the origins of transitions A and B.

9. Implications of phase separation and atomic ordering on semiconductor technology

The occurrence of phase separation and atomic ordering in mixed III–V epitaxial layers has a number of implications on semiconductor technology.

(1) *Effect of phase separation on laser degradation:* the studies of Petroff and Hartman (1973), Hutchinson and Dobson (1975), and Ishida et al. (1977) have shown convincingly that dark-line defects (DLDs) observed in degraded GaAs/GaAlAs lasers consist of highly jagged dislocations in the form of long dipoles. A consensus has emerged that these dislocation networks originate from dislocations existing in the heterostructure and that their evolution involves nonradiative recombination enhanced climb and glide (Petroff and Hartman 1973, Hutchinson and Dobson 1975, Ishida et al. 1977).

Mahajan et al. (1979) and Temkin et al. (1982) have used optical pumping to simulate the degradation behavior of light-emitting devices based on the InP/InGaAsP system. At low power levels, dense dislocation networks develop from existing dislocations and inclusion generated dislocations (Mahajan et al. 1979). At higher power levels, thermomigration of liquid droplets occurs under the temperature gradient produced by optical pumping and nonradiative regions develop by dissolution and deposition processes that accompany the migration of droplets (Mahajan et al. 1984b). A significant result of these studies is that the InGaAsP epitaxial layers are considerably more degradation-resistant than the GaAlAs layers. A plausible explanation is that in the presence of phase separation or phase separation and ordering, the multiplication of dislocations by glide and climb will be impeded (Mahajan 1983). As a result, the active layers that are phase separated and atomically ordered will be more degradation-resistant. Therefore, the light-emitting devices containing such active layers will be more reliable.

(2) *Effects of ordering on laser emission and threshold:* ordering has both beneficial and deleterious effects on laser operation. The beneficial effect is the reduction in threshold current densities. Ueno et al. (1990) at NEC reported use of ordering for making high-power visible lasers with window structures at the mirror facets. Fujii et al. (1992) at NEC showed that the threshold currents in AlGaInP lasers depend on the directions of stripes for current injection. This reflects the E_1 versus E_2 valence-band splitting (§ 8.3). They find that the threshold currents in the $[\bar{1}10]$ and [110] direction were 1.35 and 2.10 kA/cm^2, respectively. This indicates that one should select the correct stripe direction for lasers made of an active layer containing ordered alloys; this could reduce significantly the threshold current. A similar result was obtained by the Sony group of Nakano et al. (1992).

The deleterious effect of ordering on red-emitting $Ga_{0.5}In_{0.5}P$/GaAs lasers is due to the shift of the emission wavelength by ~20 nm. This is undesirable. Valster et al. (1991) have used the effect of substrate orientation on ordering to address this technological problem. They have shown that when the structures are grown on the $(113)_B$ substrates, ordering is not observed under "normal" growth conditions in the active layers, leading to a reproducible control of the emission wavelength of the devices. A similar misorientation effect was reported by Hamada et al. (1991), Minagawa and Kondow (1989), Valster et al. (1991), M. Suzuki et al. (1991), and by Suzuki and Gomyo (1993).

(3) *Use of ordering-induced band-gap reduction for III–V based far-IR detectors:* Wei and Zunger (1991) predicted that CP_B ordering in InAsSb or GaInSb will reduce their band gaps significantly, so as to produce a potentially useful far-infrared III–V

material. Recently, the Sandia group (Kurtz et al. 1992) have reported successful MBE growth of spontaneously ordered InAsSb layers exhibiting emission near 9 μm, confirming the above expectations. Superlattices and quantum-well structures consisting of ordered and disordered layers were fabricated. The interfaces in these structures should be extremely sharp because the ordered and disordered layers have the same composition.

(4) *Effects of ordering on GaInP tandem solar cells:* Kurtz et al. (1990b) have calculated the efficiencies of two-junction, series-connected solar cells as a function of the band gap and thickness of the top cell. They found that if the GaAs bottom cell has a band gap of 1.424 eV, the optimal thickness of the top cell depends on its band gap, hence, degree of ordering. If the top-cell material is disordered (E_g = 1.92 eV) a top-cell thickness of ~1.5 μm gives a theoretical efficiency of ~34%, while if the top-cell material is ordered (Eg = 1.85 eV) an optimal thickness of ~0.8 μm is needed for a 33–34% efficiency. However, a band gap as low as 1.70 eV is undesirable since in this case the cell efficiency depends too sensitively on the top-cell thickness and a 10% variation in thickness could result in a variation of a few efficiency points. They predicted an optimal top-cell thickness of 0.75 μm for a $GaAs/Ga_{0.5}In_{0.5}P$ cell with a top-cell band gap of 1.85–1.86 eV. They were able to fabricate such a cell, finding 27% efficiency, in good agreement with this prediction. Friedman et al. (1991a,b) have further noted that the best passivation layer for ordered $GaInP_2$ is disordered $Ga_{0.5}In_{0.5}P$. This leads to an improvement in the open-circuit voltage.

(5) *Potential applications of ordering to high-speed devices:* the fact that single-domain ordering alloys show an *enhancement* in mobility (A. Chin et al. 1991, Ueda and Nakata 1992) opens the possibility of using such materials (after their microstructure will be further perfected) for future high-speed devices.

(6) *Applications in light-emitting diodes*: Lee et al. (1992) demonstrated an LED made of a disordered/ordered/disordered sandwich structure of MOCVD-grown GaInP. The emission is red-shifted and has stronger output intensity relative to a conventional homojunction LED.

10. Summary

The status of our current understanding regarding the occurrence of atomic ordering and phase separation in ternary and quaternary III–V epitaxial layers is reviewed in this chapter. It is shown that the atoms within the layers are not distributed at random within the respective sublattices. Two classes of macroscopic deviations from randomness are observed: (i) phase separation and (ii) atomic ordering.

Phase separation is driven by atomic size mismatch and therefore occurs frequently in bulk-grown alloys whose constituents differ in atomic sizes. Phase separation is reduced by coherent epitaxy (LPE, VLE, VPE, OMVPE, and MBE) due to substrate strain. In such epitaxial layers, phase separation occurs along the elastically soft direction in the substrate plane rather than along the growth direction. It is observed by X-ray microanalysis, as well as by bright- and dark-field images and electron

diffraction patterns, where the wavelength of composition modulation $\leqslant 100$ Å. The tendency of like atoms to cluster is also manifested by microscopic short-range order on the scale of a few bond lengths (~ 5 Å). This is observed in impurity-bound PL, NMR chemical shifts, X-ray diffuse scattering, resonance Raman, and IR vibrational spectra.

Long-range atomic ordering can occur due to epitaxial constraints (chalcopyrite ordering) as well as surface reconstruction (CuPt ordering). The degree of ordering is not perfect, depending on substrate misorientation, V/III ratio, growth temperature, and dopants. It is manifested by new superlattice diffraction spots, a reduction in band gap, a splitting in the valence band, and altered NMR chemical shifts. Currently grown ordered samples exhibit a "mosaic structure" consisting of domains with different degrees of ordering (hence, different band gaps). This leads to broadening of the exciton lines, a Stokes shift between PL and PLE, a slow rise in the PLE spectra, an intensity-dependent PL structure, and coexistence of ordering with phase separation. These features are expected to diminish (or disappear) when large, single domain structures will be grown. Such structures are expected to exhibit large valence-band splittings and band-gap reductions, sharp exciton lines, small Stokes shifts, higher mobilities, and further suppression of phase separation.

11. Open issues and research opportunities

This review on the experimental and theoretical aspects of nonrandomness in III–V alloys clearly points to areas where further developments are urgently needed:

(i) The discussion of § 3 clearly indicates that experimental measures of clustering versus anticlustering in III–V alloys are currently both insufficient and inconclusive. Further NMR, EXAFS, impurity-PL, Raman, IR, and X-ray diffuse scattering experiments and better analytical interpretations are clearly needed to establish the atomic structure on a scale < 10 Å. In particular: (a) all current analyses of the vibrational properties suggest clustering ($\beta > 0$), whereas all theoretical models favor anticlustering ($\beta < 0$). (b) We do not know how clustering or anticlustering affects bond lengths. (c) We do not know how bond relaxation due to clustering interacts with chemical SRO to alter the diffuse scattering.

(ii) The discussion of § 4 indicates that the various types of epitaxial phase separation (e.g., lateral versus vertical) as well as the growth conditions leading to the various forms of phase separation (e.g., homogeneous growth versus mobility enhanced growth versus superlattice growth) are poorly understood. We do not understand in any detail the effects on phase separation of surface steps, exchange reaction, preferential attachment to step-edge versus terrace sites, and how surface reconstruction affects the above. Furthermore, for a given alloy, we do not know how growth temperature and the presence of steps selects a particular form and wavelength of phase separation over others. In addition, the origins of step-induced segregation and step-induced lateral phase separation are unknown.

(iii) Section 8 reveals that the optical fingerprints of microscopic SRO are yet unknown, e.g., does local clustering increase or decrease the band gap? Theoretical

tools capable of addressing this question seem to be lacking, as are experimental studies.

(iv) Section 5 highlights the fact that while ordering in III–V alloys was seen in many cases, with the exception of a single example, ordering in II–VI systems was not observed. Is ordering restricted to III–V physics or is it that II–VI systems were not studied sufficiently in this respect?

(v) Theoretical predictions suggest (§§ 2.1 and 4.2) that chalcopyrite-type and/or famatinite-type ordering will exist in low-temperature epitaxial growth of size-mismatched alloys (fig. 9), yet this has been seen only in one or two cases (Nakayama and Fujita 1986, Jen et al. 1986).

(vi) The CA ordering in $Al_{0.5}Ga_{0.5}As/GaAs$ (110) is currently without explanation.

(vii) Section 7.2 describes predictions of CuPt ordering *at the free surface* of cation-stabilized III–V alloys, but this was not examined experimentally (e.g., by STM).

(viii) Section 6 demonstrated how various growth parameters can affect the size of the ordered domains, e.g., substrate steps, misorientation, low growth rates, etc. There is a clear need to optimize these variables, so large ordered domains can be made and studied. Furthermore, attempts at growing the CA, CH, and CP structure by *artificial* shutter-controlled (as opposed to spontaneous) growth methods could both provide control samples and shed further light on the ordering mechanism. To date, the only artificially grown CA samples are $AlGaAs_2$ and Ga_2PAs, and no artificially grown CH or CP structures have been reported.

(ix) While there are numerous experimental and some theoretical studies on the effects of LRO on optical properties (§ 8.3), almost all experimental studies were confined to $GaInP_2$ and to some extent to $GaInAs_2$. Theory predicts profound effects of ordering on virtually *all* III–V and II–VI alloys (e.g., fig. 52) and that the *type* of ordering (CA, CH, CP) can change the magnitude and nature of the band gap. For example, CP ordering of $AlGaAs_2$ is predicted to lead to a direct band gap while CA ordering of the same material leads to an indirect gap. Also, CP ordering of $Ga_2PAs/GaAs$ is predicted to lead to a direct gap, while growth on a lattice-matched substrate would lead to an indirect gap. These and other predictions (§ 8.3.1) await further experimental testing.

(x) Growth of ordered/disordered superlattices, quantum wells, and quantum boxes/wires made of ordered materials appears to be an interesting area of research.

Acknowledgements

The authors benefitted considerably from discussions with their colleagues at the National Renewable Energy Laboratory (NREL), Bellcore, AT&T Bell Laboratories, and Carnegie Mellon University. A. Zunger would like to thank his collaborators J.E. Bernard, L.G. Ferreira, S. Froyen, D. Laks, R. Osorio, and S.H. Wei. A. Zunger's work at NREL was supported by the Department of Energy, Office of Energy Research and Office of Conservation and Renewables, whereas S. Mahajan's work at CMU was supported by ONR and DOE. We would also like to thank R. Alonso, J. Bernard, M. Bode, S. Froyen, F. Glas, Sarah Kurtz, A. Mascarenhas,

G. Stringfellow, and T. Suzuki for reviewing this manuscript and making helpful comments and suggestions.

References

Alonso, R.G., A. Mascarenhas, S. Froyen, G.S. Horner, K. Bertness and J.M. Olson, 1993a, Solid State Commun. **85**, 1021.
Alonso, R.G., A. Mascarenhas, G.S. Horner, K.A. Bertness, Sarah R. Kurtz and J.M. Olson, 1993b, Phys. Rev. B, in press.
Arent, D.J., M. Bode, K.A. Bertness, Sarah R. Kurtz and J.M. Olson, 1993, Appl. Phys. Lett. **62**, 1086.
Augarde, E., M. Mpaskoutas, P. Bellon, J.P. Chevalier and G.P. Martin, 1989, Inst. Phys. Conf. Ser. **100**, 155.
Bachrach, R.Z., R.S. Bauer, P. Chiaradia and G.V. Hansson, 1981, J. Vac. Sci. & Technol. **56**, 335.
Balzarotti, A., P. Letardi and N. Motta, 1985a, Solid State Commun. **56**, 471.
Balzarotti, A., N. Motta, A. Kisiel, M. Zimnal-Starnawska, M.T. Czyżyk and M. Podgórny, 1985b, Phys. Rev. B **31**, 7526.
Baxter, C.S., R.F. Broom and W.M. Stobbs, 1990, Surf. Sci. **228**, 102.
Baxter, C.S., W.M. Stobbs and J.H. Wilkie, 1991, in: Microscopy of Semiconducting Materials, Inst. Phys. Conf. Ser. **117**, 469.
Bellon, P., J.P. Chevalier, G.P. Martin, E. Dupont-Nivet, C. Thiebaut and J.P. André, 1988, Appl. Phys. Lett. **52**, 567.
Bellon, P., J.P. Chevalier, E. Augarde, J.P. André and G.P. Martin, 1989, J. Appl. Phys. **66**, 2388.
Benchimol, J.L., M. Quillec and S. Slempkes, 1983, J. Cryst. Growth **64**, 96.
Berak, J., and Z. Pruchnik, 1971, Roczn. Chem. Ann. Soc. Chim. Polon. **45**, 1425.
Bernard, J.E., 1993, unpublished.
Bernard, J.E., and A. Zunger, 1986, Phys. Rev. B **34**, 5992.
Bernard, J.E., and A. Zunger, 1987, Phys. Rev. B **36**, 3196.
Bernard, J.E., S.-H. Wei, D.M. Wood and A. Zunger, 1987, Appl. Phys. Lett. **52**, 311.
Bernard, J.E., L.G. Ferreira, S.-H. Wei and A. Zunger, 1988, Phys. Rev. B **38**, 6338.
Bernard, J.E., R.G. Dandrea, L.G. Ferreira, S. Froyen, S.-H. Wei and A. Zunger, 1990, Appl. Phys. Lett. **56**, 731.
Bernard, J.E., S. Froyen and A. Zunger, 1991, Phys. Rev. B **44**, 11178.
Beshah, K., D. Zamir, P. Becla, P.A. Wolf and R.G. Griffin, 1987, Phys. Rev. B **36**, 6420.
Bhattacharya, P.K., and J.W. Ku, 1985, J. Appl. Phys. **58**, 1410.
Blood, P., and A.D.C. Grassie, 1984, J. Appl. Phys. **56**, 1866.
Bocchi, C., P. Franzosi and C. Ghezzi, 1985, J. Appl. Phys. **57**, 4533.
Bode, M., 1993, J. Appl. Phys., in press.
Boguslawski, P., 1990, Phys. Rev. B **42**, 3737.
Boguslawski, P., and A. Baldereschi, 1988, Solid State Commun. **66**, 674.
Bruhl, H.G., L. Hildisch, H. Morwinski, W. Schmidt and E. Schubert, 1977, Phys. Status Solidi (a) **39**, 133.
Buchan, N., A. Jakubowicz, R.F. Broom, W. Heuberger and P. Roentgen, 1992, Appl. Phys. Lett. **61**, 2996.
Burkhalova, G.A., and D.V. Sementsova, 1965, Russ. J. Inorg. Chem. **10**, 1024.
Burns, J.H., and W.R. Busing, 1965, Inorg. Chem. **4**, 1510.
Bylander, D.M., and L. Kleinman, 1986, Phys. Rev. B **34**, 5280.
Cahn, J.W., 1961, Acta Metall. **2**, 795.
Cao, D.S., A.W. Kimball and G.B. Stringfellow, 1989, J. Appl. Phys. **66**, 5384.
Cao, D.S., E.H. Reihlen, G.S. Chen, A.W. Kimball and G.B. Stringfellow, 1991, J. Cryst. Growth **109**, 279.
Capobianco, C., B.P. Burton, P.M. Davidson and A. Navrotsky, 1987, J. Solid State Chem. **71**, 214.
Cardona, M., T. Suemoto, N.E. Christensen, T. Isu and K. Ploog, 1987, Phys. Rev. B **36**, 5906.

Chadi, D.J., 1987, J. Vac. Sci. & Technol. A **5**, 834.
Chang, K.T., and E. Goo, 1992, J. Vac. Sci. & Technol. B **10**, 1549.
Chen, G.S., and G.B. Stringfellow, 1991, Appl. Phys. Lett. **59**, 3258.
Chen, G.S., D.H. Jaw and G.B. Stringfellow, 1990, Appl. Phys. Lett. **56**, 2475.
Chen, G.S., D.H. Jaw and G.B. Stringfellow, 1991, J. Appl. Phys. **69**, 4263.
Cheng, K.Y., K.-C. Hsieh and J.N. Baillargeon, 1992, Appl. Phys. Lett. **60**, 2892.
Cherng, M., Y.T. Cherng, H.R. Chen, P. Harper, R.M. Cohen and G.B. Stringfellow, 1986b, J. Electron. Mater. **15**, 79.
Cherng, Y.T., G.B. Stringfellow and R.M. Cohen, 1986a, Appl. Phys. Lett. **44**, 550.
Chernov, R.V., and V.V. Bugaerko, 1976, Russ. J. Inorg. Chem. **21**, 1518.
Chernov, R.V., V.V. Bugaerko and A.N. Antishko, 1976, Russ. J. Inorg. Chem. **21**, 115.
Cherns, D., P.D. Greene, A. Hainsworth and A.R. Preston, 1987, in: Microscopy of Semiconductor Materials, eds A.G. Cullis and P.D. Augustus, Inst. Phys. Conf. Ser. **87**, 83.
Chiang, C.S., and W.C. Johnson, 1989, J. Mater. Res. **4**, 678.
Chin, A., T.Y. Chang, A. Ourmazd and E.M. Monberg, 1991, Appl. Phys. Lett. **58**, 968.
Chin, T.P., B.W. Liang, H.Q. Hou and C.W. Tu, 1991, Mater. Res. Soc. **216**, 517.
Chiu, T.H., W.T. Tsang, S.N.G. Chu, J. Shah and J.A. Ditzenberger, 1985, Appl. Phys. Lett. **46**, 408.
Chu, S.N.G., S. Nakahara, K.E. Strege and W.D. Johnston Jr, 1985, J. Appl. Phys. **57**, 4610.
Chu, S.N.G., R.A. Logan and T. Tanbun-Ek, 1992, J. Appl. Phys. **72**, 4118.
Cinagolani, R., L. Tepfer and K. Ploog, 1990, Appl. Phys. Lett. **56**, 1233.
Cohen, J.S., and ?. Schlijper, 1987, Phys. Rev. B **36**, 1526.
Cohen, J.S., and ?. Schlijper, 1988, Phys. Rev. B **36**, 12694.
Compaan, A., and R.C. Bowman, 1990, Mater. Res. Soc. Symp. Proc. **161**, 251.
Compaan, A., R.C. Bowman and D.E. Cooper, 1990a, Semicond. Sci. & Technol. **5**, S73.
Compaan, A., R.C. Bowman and D.E. Cooper, 1990b, Appl. Phys. Lett. **56**, 1055.
Cuthbert, J.D., and D.G. Thomas, 1968, J. Appl. Phys. **39**, 1573.
Dabkowski, F.P., P. Gavrilovic, K. Meehan, W. Statius, J.E. Williams, M.A. Shahid and S. Mahajan, 1988, Appl. Phys. Lett. **52**, 2142.
Dandrea, R.G., and A. Zunger, 1990, Appl. Phys. Lett. **57**, 1031.
Dandrea, R.G., and A. Zunger, 1991, Phys. Rev. B **43**, 8962.
Dandrea, R.G., J.E. Bernard, S.-H. Wei and A. Zunger, 1990a, Phys. Rev. Lett. **64**, 36.
Dandrea, R.G., S. Froyen and A. Zunger, 1990b, Phys. Rev. B **64**, 3213.
de Cremoux, B., 1982, J. Phys. (Paris) Colloq. **43**, Suppl. No. 12, C5.
de Cremoux, B., P. Hirtz and J. Ricciardi, 1981, Inst. Phys. Conf. Ser. **56**, 115.
DeLong, M.C., P.C. Taylor and J.M. Olson, 1990, Appl. Phys. Lett. **57**, 620.
DeLong, M.C., W.D. Ohlson, I. Viohl, P.C. Taylor and J.M. Olson, 1991, J. Appl. Phys. **70**, 2780.
Dimoulas, A., Z. Hatzopoulos, I. Stoemenos and A. Christou, 1990, Superlattices & Microstructures **8**, 117.
Duke, C.B., A. Paton, R.J. Meyer, L.J. Brillson, A. Kahn, D. Kanani, J. Carelli, J.L. Yeh, G. Margaritondo and A.D. Katnani, 1981, Phys. Rev. Lett. **46**, 440.
Falta, J., R.M. Tromp, M. Copel, G.D. Pettit and P.D. Kirchner, 1992, Phys. Rev. Lett. **69**, 3068.
Ferguson, I.T., A.G. Norman, B.A. Joyce, T.Y. Seong, G.R. Booker, R.H. Thomas, C.C. Phillips and R.A. Stradling, 1991, Appl. Phys. Lett. **59**, 3324.
Ferguson, I.T., A.G. Norman, T.Y. Seong, R.H. Thomas, C.C. Phillips, X.M. Zhang, R.A. Stradling, B.A. Joyce and G.R. Booker, 1992, in: Int. Symp. on GaAs and Related Compounds, 1991, Inst. Phys. Conf. Ser. **120**, 395.
Ferreira, L.G., A. Mbaye and A. Zunger, 1988, Phys. Rev. B **37**, 10547.
Ferreira, L.G., S.-H. Wei and A. Zunger, 1989, Phys. Rev. B **40**, 3197.
Foster, L.M., 1976, J. Electrochem. Soc. **121**, 1662.
Friedman, D.J., A.E. Kibbler and J.M. Olson, 1991a, Appl. Phys. Lett. **59**, 2998.
Friedman, D.J., Sarah R. Kurtz and J.M. Olson, 1991b, in: 22nd IEEE Photovoltaic Specialists Conference, 1991, p. 358.
Froyen, S., and A. Zunger, 1991a, Phys. Rev. Lett. **66**, 2132.
Froyen, S., and A. Zunger, 1991b, J. Vac. Sci. & Technol. B **9**, 2176.

Froyen, S., and A. Zunger, 1993, unpublished results.
Froyen, S., R. Osorio and A. Zunger, 1992, Phys. Scripta T **45**, 272.
Fu, Z.W., and J.D. Dow, 1987, Phys. Rev. B **36**, 7625.
Fujii, H., Y. Ueno, A. Gomyo, K. Endo and T. Suzuki, 1992, Appl. Phys. Lett. **61**, 737.
Fukui, T., and H. Saito, 1987, Appl. Phys. Lett. **50**, 824.
Furdyna, J.K., 1988, J. Appl. Phys. **64**, R29.
Gaines, J.M., P.M. Petroff, H. Kroemer, R.J. Simes, R.S. Geels and J.H. English, 1988, J. Vac. Sci. & Technol. B **6**, 1378.
Gallardo, P.G., 1992, Phys. Status Solidi (a) **134**, 119.
Gallardo, P.G., and Y.N. Lin, 1992, Phys. Status Solidi (a) **134**, K1.
Garriga, M., M. Cardona, N.E. Christensen, P. Lautenschlager, T. Isu and K. Ploog, 1987, Phys. Rev. B **36**, 3254.
Gavrilovic, P., F.P. Dabkowski, K. Meehan, J.E. Williams, W. Statius, K.C. Hsieh, N. Holonyak Jr, M.A. Shahid and S. Mahajan, 1988, J. Cryst. Growth **93**, 426.
Ge, W., W.D. Schmidt, M.D. Sturge, L.N. Pfeiffer and K.W. West, 1991, Phys. Rev. B **44**, 3432.
Glas, F., 1987, J. Appl. Phys. **62**, 3201.
Glas, F., 1989a, Inst. Phys. Conf. Ser. **100**, 167.
Glas, F., 1989b, in: Evaluation of Advanced Semiconductor Materials by Electron Microscopy, NATO ASI Series B, Vol. 203, ed. D. Cherns (Plenum Press, New York) p. 217.
Glas, F., and P. Henoc, 1987, Philos. Mag. A **56**, 311.
Glas, F., M.M.J. Treacy, M. Quillec and H. Launois, 1982, J. Phys. (Paris) Colloq. 5 **43**, 11.
Glas, F., P. Henoc and H. Launois, 1985, Inst. Phys. Conf. Ser. **76**, 251.
Glas, F., C. Gors and P. Henoc, 1990, Philos. Mag. B **62**, 373.
Glembocki, O.J., E.S. Snow, Sarah R. Kurtz and J.M. Olson, 1992, unpublished results.
Goetz, K.H., D. Bimberg, H. Jürgensen, J. Selders, A.V. Solomonov, G.F. Glonskii and M. Razeghi, 1983, J. Appl. Phys. **54**, 4543.
Gomyo, A., K. Kobayashi, S. Kawata, I. Hino and T. Suzuki, 1986, J. Crys. Growth **77**, 367.
Gomyo, A., T. Suzuki, K. Kobayashi, S. Kawata, I. Hino and T. Yuasa, 1987, Appl. Phys. Lett. **50**, 673.
Gomyo, A., T. Suzuki and S. Iijima, 1988a, Phys. Rev. Lett. **60**, 2645.
Gomyo, A., T. Suzuki, S. Iijima, H. Hotta, H. Fujii, S. Kawata, K. Kobayashi, Y. Ueno and I. Hino, 1988b, Jpn. J. Appl. Phys. **27**, L2370.
Gomyo, A., H. Hotta, I. Hino, S. Kawata, K. Kobayashi and T. Suzuki, 1989a, Jpn. J. Appl. Phys. **28**, L1330.
Gomyo, A., S. Kawata, T. Suzuki, S. Iijima and I. Hino, 1989b, Jpn. J. Appl. Phys. **28**, L1728.
Gomyo, A., T. Suzuki, K. Kobayashi, S. Hawata, H. Hotta and I. Hino, 1991, preprint. Many of these results are cited by Suzuki and Gomyo (1993).
Goryunova, N.A., and N.N. Fedorova, 1955, Zh. Tekh. Fiz. **25**, 1339.
Gowers, J.P., 1983, Appl. Phys. A **31**, 23.
Greene, P.D., S.A. Wheeler, A.R. Adams, A.N. El-Sabbahy and C.N. Ahmad, 1979, Appl. Phys. Lett. **35**, 78.
Gruzza, B., B. Achard and C. Pariset, 1985, Surf. Sci. **162**, 202.
Hamada, H., M. Shono, S. Honda, R. Hiroyama, K. Yodoshi and T. Yamaguchi, 1991, IEEE J. Quantum Electron. **27**, 1483.
Henoc, P., A. Izrael, M. Quillec and H. Launois, 1982, Appl. Phys. Lett. **40**, 963.
Hong, W.P., P.K. Bhattacharya and J. Singh, 1987, Appl. Phys. Lett. **50**, 618.
Hopfield, J.J., 1960, J. Phys. & Chem. Solids **15**, 97.
Horner, G.S., A. Mascarenhas, S. Froyen, R.G. Alonso, K. Bertness and J.M. Olson, 1993, Phys. Rev. B **47**, 4041.
Horner, G.S., A. Mascarenhas, R.G. Alonso, S. Froyen, K.A. Bertness and J.M. Olson, 1994, Phys. Rev. B, in press.
Horng, R.H., and M.K. Lee, 1992, Appl. Phys. Lett. **72**, 1513.
Hou, X., G. Dong, X. Ding and X. Wang, 1987, J. Phys. C **20**, L121.
Hsieh, K.C., J.N. Baillargeon and K.Y. Cheng, 1990, Appl. Phys. Lett. **57**, 2244.
Huijser, A., J. van Laar and T.T. van Rooy, 1981, Surf. Sci. **102**, 264.

Hutchinson, P.W., and P.S. Dobson, 1975, Philos. Mag. **32**, 745.
Ichimura, M., and A. Sasaki, 1986, J. Appl. Phys. **60**, 3850.
Ihm, Y.-E., N. Otsuka, J. Klem and H. Morkoç, 1987, Appl. Phys. Lett. **51**, 2013.
Inoue, Y., T. Nishino, Y. Hamakawa, M. Kondow and S. Minagawa, 1988, Optoelectron. Dev. & Technol. **3**, 61.
Ishida, K., T. Kamejima and J. Matsui, 1977, Appl. Phys. Lett. **31**, 397.
Ishida, K., T. Shumiya, T. Nomura, H. Ohtani and T. Nishizawa, 1988, J. Less-Common Met. **142**, 135.
Jen, H.R., M.J. Cherng and G.B. Stringfellow, 1986, Appl. Phys. Lett. **48**, 1603.
Jen, H.R., M.J. Jou, Y.T. Cherng and G.B. Stringfellow, 1987, J. Cryst. Growth **85**, 175.
Jen, H.R., D.S. Cao and G.B. Stringfellow, 1989a, Appl. Phys. Lett. **54**, 1890.
Jen, H.R., K.Y. Ma and G.B. Stringfellow, 1989b, Appl. Phys. Lett. **54**, 1154.
Johnson, W.C., and C.S. Chiang, 1988, J. Appl. Phys. **64**, 1155.
Jones, E.D., R.P. Schneider Jr, S.M. Lee and K.K. Bajaj, 1992, Phys. Rev. B **46**, 7225.
Jou, M.J., Y.T. Cherng, H.R. Jen and G.B. Stringfellow, 1988, Appl. Phys. Lett. **52**, 549.
Kakimoto, K., and T. Katoda, 1985, Jpn. J. Appl. Phys. **24**, 1022.
Kamiya, I., H. Tanaka, D.E. Aspnes, L.T. Florez, E. Colas, J.P. Harbison and R. Bhat, 1992, Appl. Phys. Lett. **60**, 1238.
Kanata, T., M. Nishimoto, H. Nakayama and T. Nishino, 1992, Phys. Rev. B **45**, 6637.
Kanata, T., M. Nishimoto, H. Nakayama and T. Nishino, 1993, Appl. Phys. Lett. **63**, 512.
Kashihara, Y., N. Kashiwaguna, M. Sakata, J. Harada and T. Arii, 1989, Jpn. J. Appl. Phys. **23**, L901.
Kikuchi, R., 1974, J. Chem. Phys. **60**, 1071.
Koiller, B., M.A. Davidovich and L.M. Falicov, 1990, Phys. Rev. B **41**, 3670.
Kondow, M., and S. Minagawa, 1989, Appl. Phys. Lett. **54**, 1760.
Kondow, M., H. Kakibayashi and S. Minagawa, 1988a, J. Cryst. Growth **88**, 291.
Kondow, M., H. Kakibayashi, S. Minagawa, Y. Inoue, T. Nishino and Y. Hamakawa, 1988b, J. Cryst. Growth **93**, 412.
Kondow, M., H. Kakibayashi, S. Minagawa, Y. Inoue, T. Nishino and Y. Hamakawa, 1988c, Appl. Phys. Lett. **53**, 2053.
Kondow, M., H. Kakibayashi, T. Tanaka and S. Minagawa, 1989a, Phys. Rev. Lett. **63**, 884.
Kondow, M., H. Kakibayashi and S. Minagawa, 1989b, Phys. Rev. B **40**, 1159.
Koster, W., and B. Thoma, 1955, Z. Metallk. **46**, 291.
Kozyrev, S.P., L.K. Vodopyanov and R. Triboulet, 1983, Solid State Commun. **45**, 383.
Krishnamurthy, A., A. Lorke, M. Wassermeier, D.R.M. Williams and P.M. Petroff, 1993, J. Vac. Sci. & Technol. B **11**, 1384.
Kuan, T.S., T.F. Kuech, W.I. Wang and E.L. Wilkie, 1985, Phys. Rev. Lett. **54**, 201.
Kuan, T.S., W.I. Wang and E.L. Wilkie, 1987, Appl. Phys. Lett. **51**, 51.
Kuphal, E., 1984, J. Cryst. Growth **67**, 441.
Kuphal, E., and A. Pöcker, 1982, J. Cryst. Growth **58**, 133.
Kurtz, Sarah R., J.M. Olson and A. Kibbler, 1988, Solar Cells **24**, 307.
Kurtz, Sarah R., J.M. Olson and A. Kibbler, 1989, Appl. Phys. Lett. **54**, 718.
Kurtz, Sarah R., J.M. Olson and A. Kibbler, 1990a, Appl. Phys. Lett. **54**, 718.
Kurtz, Sarah R., J.M. Olson, J.P. Goral, A. Kibbler and E. Beck, 1990b, J. Elect. Mater. **19**, 825.
Kurtz, Steve R., L.R. Dawson, R.M. Biefeld, D.M. Follstaedt and B.L. Doyle, 1992, Phys. Rev. B **46**, 1909.
Laks, D.B., and A. Zunger, 1992, Phys. Rev. B **45**, 11411.
Laks, D.B., S.-H. Wei and A. Zunger, 1992, Phys. Rev. Lett. **69**, 3766.
Landgren, G., and R. Ludeke, 1981, Solid State Commun. **37**, 127.
Larche, F.C., W.C. Johnson, C.S. Chiang and G.P. Martin, 1988, J. Appl. Phys. **64**, 5251.
Launois, H., M. Quillec, F. Glas and M.M.J. Treacy, 1982, Inst. Phys. Conf. Ser. **65**, 537.
Lee, M.K., R.H. Horng and L.C. Haung, 1991, Appl. Phys. Lett. **59**, 3261.
Lee, M.K., R.H. Horng and L.C. Haung, 1992, J. Appl. Phys. **72**, 3420.
Lee, S., D.M. Bylander and L. Kleinman, 1989, Phys. Rev. B **40**, 8399.
LeGoues, F.K., V.P. Kesan and S.S. Iyer, 1990, Phys. Rev. Lett. **66**, 40.
Lin, J.F., M.J. Jou, C.Y. Chen and B.J. Lee, 1992, J. Cryst. Growth **124**, 415.

Lu, Y.-T., P. Petroff and H. Metiu, 1990, Appl. Phys. Lett. **57**, 2683.
Lu, Z.W., S.-H. Wei and A. Zunger, 1993, Europhys. Lett. **21**, 221.
Mackenzie, R.A.D., J.A. Liddle and C.R.M. Grovenor, 1991, J. Appl. Phys. **69**, 250.
Mader, K., and A. Zunger, 1993, unpublished.
Magri, R., and A. Zunger, 1991, Phys. Rev. B **43**, 1584.
Mahajan, S., 1983, Inst. Phys. Conf. Ser. **67**, 259.
Mahajan, S., 1991, in: Proc. Fifth Brazilian School on Semiconductor Physics, ed. J.R. Leite (World Scientific, Singapore) pp. 79–98.
Mahajan, S., and B.A. Philips, 1992, in: Ordered Intermetallics – Physical Metallurgy and Mechanical Behavior, eds C.T. Liu, R.W. Cahn and G. Sauthoff (Kluwer, Dordrecht) pp. 93–106.
Mahajan, S., and M.A. Shahid, 1989, in: Advances in Materials, Processing, and Devices on III–V Compound Semiconductors, eds D.K. Sadana, L.E. Eastman and R. Dupuis, Mater. Res. Soc. Symp. Proc. **144**, 169.
Mahajan, S., W.D. Johnston Jr, M.A. Pollack and R.E. Nahory, 1979, Appl. Phys. Lett. **34**, 717.
Mahajan, S., B.V. Dutt, H. Temkin, R.J. Cava and W.A. Bonner, 1984a, J. Cryst. Growth **68**, 589.
Mahajan, S., H. Temkin and R.A. Logan, 1984b, Appl. Phys. Lett. **34**, 119.
Mahajan, S., M.A. Shahid and D.E. Laughlin, 1989, Inst. Phys. Conf. Ser. **100**, 143.
Martins, J.L., and A. Zunger, 1984, Phys. Rev. B **30**, 6217.
Martins, J.L., and A. Zunger, 1985, Phys. Rev. B **32**, 2689.
Martins, J.L., and A. Zunger, 1986a, J. Mater. Res. **1**, 523.
Martins, J.L., and A. Zunger, 1986b, Phys. Rev. Lett. **56**, 1400.
Mascarenhas, A., and J.M. Olson, 1990, Phys. Rev. B **41**, 9947.
Mascarenhas, A., Sarah R. Kurtz, A. Kibbler and J.M. Olson, 1989, Phys. Rev. Lett. **63**, 2108.
Mascarenhas, A., R.G. Alonso, G.S. Horner, S. Froyen, K.C. Hsieh and K.Y. Cheng, 1992, Superlattices & Microstructures **12**, 57.
Masumoto, K., S. Isomura and K. Saski, 1971, Phys. Status Solidi (a) **6**, 515.
Matsumura, S., N. Kuwano and K. Oki, 1990, Jpn. J. Appl. Phys. **26**, 688.
Matsumura, S., K. Takano, N. Kuwano and K. Oki, 1991, J. Cryst. Growth **115**, 194.
Mbaye, A., A. Zunger and D.M. Wood, 1986, Appl. Phys. Lett. **49**, 782.
Mbaye, A., L.G. Ferreira and A. Zunger, 1987, Phys. Rev. Lett. **58**, 49.
Mbaye, A., D.M. Wood and A. Zunger, 1988, Phys. Rev. B **37**, 3008.
McDermott, B.T., K.G. Reid, N.A. El-Masry, S.M. Bedair, W.M. Duncan, X. Yin and F.H. Pollak, 1990, Appl. Phys. Lett. **56**, 1172.
McDermott, B.T., N.A. El-Masry, B.L. Jiang, F. Hyuga and S.M. Bedair, 1991, J. Cryst. Growth **107**, 96.
McDevitt, T.L., 1990, Ph.D. Dissertation (Carnegie Mellon University, Pittsburgh, PA) unpublished.
McDevitt, T.L., S. Mahajan, D.E. Laughlin, W.A. Bonner and V.G. Keramidas, 1990, in: Epitaxial Heterostructures, eds D.W. Shaw, J.C. Bean, V.G. Keramidas and P.S. Peercy, Mater. Res. Soc. Symp. Proc. **198**, 609.
McDevitt, T.L., S. Mahajan, D.E. Laughlin, W.A. Bonner and V.G. Keramidas, 1991, Inst. Phys. Conf. Ser. **117**, 477.
McDevitt, T.L., S. Mahajan, D.E. Laughlin, W.A. Bonner and V.G. Keramidas, 1992, Phys. Rev. B **45**, 6614.
McKernan, S., B.C. DeCooman and C.B. Carter, 1988, J. Mater. Res. **3**, 406.
Meehan, K., F.P. Dabkowski, P. Gavrilovic, J.E. Williams, W. Stutius, K.S. Shieh and N. Holonyak Jr, 1989, Appl. Phys. Lett. **54**, 2136.
Mena, R.A., G.D. Sanders, K.K. Bajaj and S.C. Dudley, 1991, J. Appl. Phys. **70**, 1866.
Mikkelson Jr, J.C., and J.B. Boyce, 1982, Phys. Rev. Lett. **49**, 1412.
Minagawa, S., and M. Kondow, 1989, Electron. Lett. **25**, 758.
Morita, E., M. Ikeda, O. Kumagai and K. Kaneko, 1988, Appl. Phys. Lett. **53**, 2164.
Mowbray, D.J., R.A. Hogg, M.S. Skolnick, M.C. DeLong, Sarah R. Kurtz and J.M. Olson, 1992, Phys. Rev. B **46**, 7232.
Mukai, S., 1983, J. Appl. Phys. **54**, 2635.
Murgatroyd, I.J., A.G. Norman, G.R. Booker and T.M. Kerr, 1986, in: Proc. 11th Int. Conf. on Electron Microscopy, eds T. Imura, S. Maruse and T. Suzuki (Japanese Society of Electron Microscopy, Tokyo) p. 1497.

Murgatroyd, I.J., A.G. Norman and G.R. Booker, 1990, J. Appl. Phys. **67**, 2310.
Nakano, K., A. Toda, T. Yamamoto and A. Ishibashi, 1992, Appl. Phys. Lett. **61**, 1959.
Nakayama, H., and H. Fujita, 1986, Inst. Phys. Conf. Ser. **79**, 289.
Navrotsky, A., and C. Capobianco, 1987, Am. Mineral. **72**, 782.
Neave, J.H., P.J. Dobson, B.A. Joyce and J. Zhang, 1985, Appl. Phys. Lett. **47**, 100.
Newman, K.E., and X. Xiang, 1991, Phys. Rev. B **44**, 4677.
Nishino, T., Y. Inoue, Y. Hamakawa, M. Kondow and S. Minagawa, 1988, Appl. Phys. Lett. **53**, 583.
Nohory, R.E., 1993, Bellcore.
Norman, A.G., 1985, Ph.D. Dissertation (University of Oxford) unpublished.
Norman, A.G., and G.R. Booker, 1985, J. Appl. Phys. **57**, 4715; Inst. Phys. Conf. Ser. **76**, 257.
Norman, A.G., R.E. Mallard, I.J. Murgatroyd, G.R. Booker, A.H. Moore and M.D. Scott, 1987, Inst. Phys. Conf. Ser. **87**, 77.
Norman, A.G., T.Y. Seong, I.T. Ferguson, G.R. Booker and B.A. Joyce, 1993, Semicond. Sci. & Technol. **8**, S9.
Northrup, J.E., and S. Froyen, 1993, Phys. Rev. Lett. **71**, 2276.
Nozaki, C., Y. Ohba, H. Sugawara, S. Yasuami and T. Nakanisi, 1988, J. Cryst. Growth **93**, 406.
Ogale, S.B., and A. Madhukar, 1991, Appl. Phys. Lett. **69**, 1356.
Ogale, S.B., A. Madhukar, S.Y. Joshi and R. Viswanathan, 1992, J. Vac. Sci. & Technol. B **10**, 1689.
Okuda, H., C. Anayama, T. Tanahashi and K. Nakajima, 1989, Appl. Phys. Lett. **55**, 2190.
Okuda, H., M. Kondo, K. Kato and K. Nakajima, 1990, Appl. Phys. Lett. **56**, 337.
Osamura, K., M. Sugahara and K. Nakajima, 1987, Jpn. J. Appl. Phys. **26**, L1746.
Osorio, R., S. Froyen and A. Zunger, 1991a, Phys. Rev. B **43**, 14055.
Osorio, R., S. Froyen and A. Zunger, 1991b, Solid State Commun. **78**, 249.
Osorio, R., J.E. Bernard, S. Froyen and A. Zunger, 1992a, Phys. Rev. B. **45**, 1173.
Osorio, R., J.E. Bernard, S. Froyen and A. Zunger, 1992b, J. Vac. Sci. & Technol. B **10**, 1683.
Osorio, R., Z.W. Lu, S.-H. Wei and A. Zunger, 1993, Phys. Rev. B **47**, 9985.
Otsuka, N., Y.E. Ihm, Y. Hurotsu, J. Klein and H. Morkoç, 1989, J. Cryst. Growth **95**, 43.
Panish, M.B., and M. Ilegems, 1972, in: Progress in Solid State Chemistry, eds M. Reiss and J.O. McCaldin (Pergamon Press, New York) p. 39.
Park, K., L. Salamanca-Riba and B.T. Jonker, 1992, Appl. Phys. Lett. **61**, 2302.
Pashley, M.D., K.W. Haberern, W. Friday, J.M. Woodall and P.D. Kirchner, 1988, Phys. Rev. Lett. **60**, 2176.
Pashley, M.D., K.W. Haberern and J.M. Gaines, 1991, J. Vac. Sci. & Technol. B **9**, 938.
Patrick, R., A.-B. Chen and A. Sher, 1987, Phys. Rev. B **36**, 6585.
Peiro, F., A. Villa, A. Comet, A. Herms, J.R. Morante, S. Clark and R.H. Williams, 1991, in: Microscopy of Semiconducting Materials, Inst. Phys. Conf. Ser. **117**, 519.
Perkowitz, S., L.S. Kim and P. Becla, 1991, Phys. Rev. B **43**, 6598.
Petroff, P.M., and R.L. Hartman, 1973, Appl. Phys. Lett. **23**, 469.
Petroff, P.M., A.Y. Cho, F.K. Reinhart, A.C. Gossard and W. Wiegmann, 1982, Phys. Rev. Lett. **48**, 170.
Philips, B.A., A.G. Norman, T.Y. Tseong, S. Mahajan, G.R. Booker, M. Skowronski, J.P. Harbison and V.G. Keramidas, 1993, J. Cryst. Growth, submitted.
Plano, W.E., D.W. Nam, J.S. Major Jr, K.C. Hsieh and N. Holonyak Jr, 1988, Appl. Phys. Lett. **53**, 2537.
Quillec, M., J.L. Benchimol, S. Slempkes and H. Launois, 1983, Appl. Phys. Lett. **42**, 886.
Quintero, M., E. Guerrero, R. Tovar and G.S. Perez, 1990, J. Solid State Chem. **87**, 456.
Ramos, A., C. Levelut, J. Petiau and F. Villain, 1993, J. Phys.: Condens. Matter **5**, 3507.
Reihlen, E.H., M.J. Jou, Z.M. Fang and G.B. Stringfellow, 1990, J. Appl. Phys. **68**, 4604.
Reise, S., E. Milas and H. Merz, 1992, Surf. Sci. **269/270**, 833.
Roberts, J.S., G.B. Scott and J.P. Gowers, 1981, J. Appl. Phys. **52**, 4018.
Salamanca-Riba, L., K. Park and B.T. Jonker, 1992, Mater. Res. Soc. Symp. Proc. **231**, 347.
Samuelson, L., S. Nilsson, Z.G. Wang and H.G. Grimmeiss, 1984, Phys. Rev. Lett. **53**, 1501.
Schneider Jr, R.P., E.D. Jones, J.A. Lott and R.P. Bryan, 1992, J. Appl. Phys. **72**, 5397.
Schubert, E.F., and W.T. Tsang, 1986, Phys. Rev. B **34**, 2991.
Sela, I., V.V. Gridin, R. Beserman and H. Morkoç, 1988a, Phys. Rev. B **37**, 6393.
Sela, I., V.V. Gridin, R. Beserman, R. Sarfaty, D. Fekete and H. Morkoç, 1988b, J. Appl. Phys. **63**, 966.

Seong, T.Y., A.G. Norman, G.R. Booker, R. Droopad, R.L. Williams, S.D. Parker, P.D. Wang and R.A. Stradling, 1990, Mater. Res. Soc. Symp. Proc. **163**, 907.
Shahid, M.A., and S. Mahajan, 1988, Phys. Rev. B **38**, 1344.
Shahid, M.A., S. Mahajan, D.E. Laughlin and H.M. Cox, 1987, Phys. Rev. Lett. **58**, 2567.
Shen, Y.T., D.M. Bylander and L. Kleinman, 1988, Phys. Rev. B **38**, 13257.
Sher, A., A.-B. Chen and M. van Schilfgaarde, 1986, J. Vac. Sci. & Technol. A **4**, 1965.
Shih, C., and E.A. Peretti, 1953, J. Am. Chem. Soc. **75**, 608.
Shirakata, S., M. Kondow, T. Nishino and Y. Hamakawa, 1986, Jpn. J. Appl. Phys. **25**, 435.
Sood, A.K., K. Wu and J.N. Zemel, 1978, Thin Solid Films **48**, 73; J. Appl. Phys. **49**, 5292.
Srivastava, G.P., J.L. Martins and A. Zunger, 1985, Phys. Rev. B **31**, 2561.
Stringfellow, G.B., 1974, J. Cryst. Growth **27**, 21.
Stringfellow, G.B., 1982a, J. Cryst. Growth **58**, 194.
Stringfellow, G.B., 1982b, J. Electron. Mater. **11**, 903.
Stringfellow, G.B., 1989, J. Cryst. Growth **98**, 108.
Stringfellow, G.B., 1993, private communication.
Stringfellow, G.B., and M. Cherng, 1988, J. Cryst. Growth **64**, 413.
Su, L.C., S.T. Pu, G.B. Stringfellow, J. Christen, H. Selber and D. Bimberg, 1993, Appl. Phys. Lett. **62**, 3496.
Sullivan, P.W., R.F.C. Farrow and G.R. Jones, 1982, J. Cryst. Growth **60**, 403.
Suzuki, M., Y. Nishizawa, M. Ishikawa and Y. Kokubun, 1991, J. Cryst. Growth **113**, 127.
Suzuki, T., and A. Gomyo, 1990a, J. Cryst. Growth **99**, 60.
Suzuki, T., and A. Gomyo, 1990b, 6th International Conference on MBE, San Diego, CA, Abstract XII-3, unpublished.
Suzuki, T., and A. Gomyo, 1991, J. Cryst. Growth **111**, 353.
Suzuki, T., and A. Gomyo, 1993, in: NATO ASI Series, Physical Properties of Semiconductor Interfaces at Sub-Nanometer Scale, ed. H.W. Salemink (Kluwer, Dordrecht) in press.
Suzuki, T., A. Gomyo and S. Iijima, 1988a, J. Cryst. Growth **93**, 396.
Suzuki, T., A. Gomyo, S. Iijima, K. Kobayashi, S. Kawata, I. Hino and T. Yuasa, 1988b, Jpn. J. Appl. Phys. **27**, 2098.
Suzuki, T., A. Gomyo, I. Hino, K. Kobayashi, S. Kawata and S. Iijima, 1988c, Jpn. J. Appl. Phys. **27**, L1549.
Suzuki, T., A. Gomyo and S. Iijima, 1992, in: Ordering at Surfaces and Interfaces, Proc. 3rd NEC Symp., Hakone, Japan, eds H. Yoshimori, T. Shinjo and W. Watanabe (Springer, Berlin) p. 363.
Takarohashi, T., and M. Ozeki, 1991, J. Appl. Phys. **30**, L956; J. Cryst. Growth **115**, 538.
Tchakpele, K.P., and J.P. Albert, 1988, Phys. Status Solidi (b) **149**, 641.
Temkin, H., S. Mahajan, M.A. DiGuiseppe and A.G. Dentai, 1982, Appl. Phys. Lett. **40**, 562.
Thurmond, C.D., 1953, J. Electrochem. Soc. **57**, 827.
Treacy, M.M.J., J.M. Gibson and A. Howie, 1985, Philos. Mag. A **51**, 380.
Trzebiatowski, W., F. Krolicki and W. Zdanowicz, 1963, Bull. Acad. Polon. Sci. **16**, 343.
Tsang, W.T., E.F. Schubert, T.H. Chiu, J.E. Cunningham, E.G. Burkhardt, J.A. Ditzenberger and E. Agyekum, 1987, Appl. Phys. Lett. **51**, 761.
Tsuchiya, M., P.M. Petroff and L.A. Coldren, 1989, Appl. Phys. Lett. **57**, 1690; Phys. Rev. Lett. **62**, 466, 1989.
Tycko, R., G. Dabbagh, Sarah R. Kurtz and J.P. Goral, 1992, Phys. Rev. B **45**, 13452.
Ueda, O., and Y. Nakata, 1992, Mater. Sci. Forum **83-87**, 1297.
Ueda, O., S. Isozumi and S. Komiya, 1984, Jpn. J. Appl. Phys. **23**, L241.
Ueda, O., M. Takikawa, J. Komeno and I. Umebu, 1987, Jpn. J. Appl. Phys. **26**, L1824.
Ueda, O., M. Takikawa, M. Takechi, J. Komono and I. Umebu, 1988, J. Cryst. Growth **93**, 418.
Ueda, O., T. Fujii, Y. Nakada, H. Yamada and I. Umebu, 1989a, J. Cryst. Growth **95**, 38.
Ueda, O., M. Takachi and J. Komeno, 1989b, Appl. Phys. Lett. **54**, 2312.
Ueda, O., M. Hoshino, K. Kodama, H. Yamada and M. Ozeki, 1990, J. Cryst. Growth **99**, 560.
Ueda, O., Y. Nakata and T. Fujii, 1991, Appl. Phys. Lett. **58**, 705.
Ueno, Y., H. Fujii, K. Kobayashi, K. Endo, A. Gomyo, K. Hara, S. Kawata, T. Yuasa and T. Suzuki, 1990, Jpn. J. Appl. Phys. **29**, L1666.

Valster, A., C.T.H.F. Lidenbaum, M.N. Funke, A.L.G. Severens, M.J.B. Boermans, D.E.W. Vandenhoudt and C.W.T. Bulle-Lieuwma, 1991, J. Cryst. Growth **107**, 403.
van Schilfgaarde, M., A.-B. Chen and A. Sher, 1986, Phys. Rev. Lett. **57**, 1149.
Verleur, H.W., and A.S. Barker, 1966, Phys. Rev. **149**, 715.
Wada, T., and Y. Maeda, 1988, Appl. Phys. Lett. **53**, 1597.
Wang, W.I., 1985, J. Appl. Phys. **58**, 3244.
Wang, X., 1988, Appl. Surf. Sci. **33–34**, 88.
Warren, B.E., 1969, X-ray Diffraction (Addison-Wesley, Reading, MA).
Wei, S.-H., 1987, Phys. Rev. Lett. **59**, 2613.
Wei, S.-H., and A. Zunger, 1988a, Phys. Rev. Lett. **61**, 1505.
Wei, S.-H., and A. Zunger, 1988b, Appl. Phys. Lett. **53**, 2077.
Wei, S.-H., and A. Zunger, 1988c, J. Vac. Sci. & Technol. A **6**, 2597.
Wei, S.-H., and A. Zunger, 1989, Phys. Rev. B **39**, 3279.
Wei, S.-H., and A. Zunger, 1990, Appl. Phys. Lett. **56**, 662.
Wei, S.-H., and A. Zunger, 1991, Appl. Phys. Lett. **58**, 2684.
Wei, S.-H., and A. Zunger, 1992, Phys. Rev. B **45**, 2533.
Wei, S.-H., and A. Zunger, 1993, Appl. Phys. Lett., in press.
Wei, S.-H., L.G. Ferreira and A. Zunger, 1990, Phys. Rev. B **41**, 8240.
Wei, S.-H., D.B. Laks and A. Zunger, 1993, Appl. Phys. Lett. **62**, 1937.
Weiss, W., R. Hornstein, D. Schmeisser and W. Gople, 1990, J. Vac. Sci. & Technol. B **8**, 715.
Wood, D.M., 1992, J. Vac. Sci. & Technol. B **10**, 1675.
Wood, D.M., and A. Zunger, 1988a, Phys. Rev. Lett. **61**, 1501.
Wood, D.M., and A. Zunger, 1988b, Phys. Rev. B **38**, 12756.
Wood, D.M., and A. Zunger, 1989, Phys. Rev. B **40**, 4062.
Wood, D.M., S.-H. Wei and A. Zunger, 1988, Phys. Rev. B **37**, 1342.
Woolley, J.C., 1962, in: Compound Semiconductors, eds R.K. Willardson and H.L. Goering (Reinhold, New York) p. 3.
Yamazaki, S., A. Ushirokawa and T. Katoda, 1980, J. Appl. Phys. **51**, 3722.
Yasuami, S., K. Koga, K. Ohshima, S. Sasaki and M. Ando, 1992, J. Appl. Crystallogr. **25**, 514.
Zax, D.B., S. Vega, N. Yellin and D. Zamir, 1987, Chem. Phys. Lett. B **8**, 105.
Zax, D.B., D. Zamir and S. Vega, 1993, Phys. Rev. B **47**, 6304.
Zhang, S.B., M.S. Hybertsen, M.L. Cohen, S.G. Louie and D. Tomanek, 1989, Phys. Rev. Lett. **63**, 1795.
Zunger, A., 1986, Int. J. Quantum Chem. S **19**, 629.
Zunger, A., 1987, Appl. Phys. Lett. **50**, 164.
Zunger, A., and A. Mbaye, 1986, unpublished.
Zunger, A., and D.M. Wood, 1989, J. Cryst. Growth **98**, 1.
Zunger, A., S.-H. Wei, L.G. Ferreira and J.E. Bernard, 1990, Phys. Rev. Lett. **65**, 353.